
Doctoral Dissertations

Student Theses and Dissertations

Spring 2019

Plasmonic metamaterial for structural color printing and spontaneous emission control

Wei Wang

Follow this and additional works at: https://scholarsmine.mst.edu/doctoral_dissertations



Part of the [Mechanical Engineering Commons](#)

Department: Mechanical and Aerospace Engineering

Recommended Citation

Wang, Wei, "Plasmonic metamaterial for structural color printing and spontaneous emission control" (2019). *Doctoral Dissertations*. 3116.

https://scholarsmine.mst.edu/doctoral_dissertations/3116

This thesis is brought to you by Scholars' Mine, a service of the Missouri S&T Library and Learning Resources. This work is protected by U. S. Copyright Law. Unauthorized use including reproduction for redistribution requires the permission of the copyright holder. For more information, please contact scholarsmine@mst.edu.

PLASMONIC METAMATERIAL FOR STRUCTURAL COLOR PRINTING AND
SPONTANEOUS EMISSION CONTROL

by

WEI WANG

A DISSERTATION

Presented to the Faculty of the Graduate School of the
MISSOURI UNIVERSITY OF SCIENCE AND TECHNOLOGY

In Partial Fulfillment of the Requirements for the Degree

DOCTOR OF PHILOSOPHY

in

MECHANICAL ENGINEERING

2019

Approved by:
Dr. Jie Gao, Advisor
Dr. Cheng Wang
Dr. Jeffrey Winiarz
Dr. Alexey Yamilov
Dr. Xiaodong Yang

© 2019

Wei Wang

All Rights Reserved

PUBLICATION DISSERTATION OPTION

This dissertation consists of the following three articles that have been published or submitted for publication as follows:

Paper I, pages 7-26 have been published in Optics Express.

Paper II, pages 27-42 have been published in Optics Express.

Paper III, pages 43-63 have been published in ACS Photonics

Paper IV, pages 64-76 have been published in Optics Letters

Paper V, pages 77-91 have been published in Applied Physics Letters

Paper VI, pages 92-107 are intended for submission to Optics Express

ABSTRACT

Plasmon polaritons or plasmons are a collective oscillation movement of free electrons in metal at optical frequencies. The frequency-dependent complex dielectric function makes the metal property at optical frequencies behave totally different with that at other spectral ranges with lower frequency such as infrared and microwaves. This novel property makes the so called plasmonics or nanoplasmonics a rapid growing research field over the past few years. Many innovative concepts and applications have been developed such as perfect absorber, structural color printing, and quantum emitter spontaneous emission enhancement.

In this dissertation two of the most important applications will be addressed. The first application is structure color printing and the other is to control the spontaneous emission rate of quantum emitters such as quantum dot. To achieve structural color printing, two different nanostructures: V-groove arrays and square shaped arrays were designed as a fundamental perfect absorber structure unit for structural color printing. To control dipole emitter spontaneous emission, hyperbolic multilayers, plasmonic perfect absorbers and chiral metasurfaces were used to enhance the spontaneous emission through Purcell effect.

ACKNOWLEDGMENTS

I would like to thank my advisor and all committee members for ongoing support of my work and many helpful discussions. Furthermore, I would like to acknowledge all the colleagues and friends who helped me in various ways in these years. Last but not least, I wish to thank all my family members and all the friends for their support. The constant support from them is deeply appreciated.

TABLE OF CONTENTS

	Page
PUBLICATION DISSERTATION OPTION	iii
ABSTRACT	iv
ACKNOWLEDGMENTS	v
LIST OF ILLUSTRATIONS	ix
 SECTION	
1. INTRODUCTION.....	1
1.1. BACKGROUND	1
1.2. ORGANIZATION OF DISSERTATION	3
 PAPER	
I. REALIZING STRUCTURAL COLOR GENERATION WITH ALUMINUM PLASMONIC V-GROOVE METASURFACES	7
ABSTRACT	7
1. INTRODUCTION	8
2. METASURFACE FABRICATION AND CHARACTERIZATION	10
3. PLASMONIC PAINTING OF COLOR IMAGES	20
4. CONCLUSIONS	21
ACKNOWLEDGMENTS	22
REFERENCES	22
II. ALL-METAL STRUCTURAL COLOR PRINTING BASED ON ALUMINUM PLASMONIC METASURFACES	27
ABSTRACT	27
1. INTRODUCTION	27

2. DEVICE DESIGN AND FABRICATION.....	29
3. RESULTS OF EXPERIMENTAL CHARACTERIZATION AND NUMERICAL SIMULATION.....	30
4. INCIDENT ANGLE DEPENDENCE OF OPTICAL RESPONSE.....	37
5. CONCLUSIONS	38
ACKNOWLEDGMENTS	38
REFERENCES	38
III. ENHANCED QUANTUM DOT SPONTANEOUS EMISSION WITH MULTILAYER METAMATERIAL NANOSTRUCTURES.....	43
ABSTRACT.....	43
1. INTRODUCTION	44
2. RESULTS AND DISCUSSION.....	47
3. CONCLUSIONS	56
4. METHODS	56
ACKNOWLEDGMENTS	60
REFERENCES	61
IV. SCALING LAW OF PURCELL FACTOR IN HYPERBOLIC METAMATERIAL CAVITIES WITH DIPOLE EXCITATION.....	64
ABSTRACT.....	64
1. INTRODUCTION	65
2. HYPERBOLIC MULTILAYER NANO-CAVITY DESIGN.....	65
3. SCALING LAW OF PURCELL FACTOR	68
4. CONCLUSIONS	74
ACKNOWLEDGMENTS	74
REFERENCES	74

V. ENHANCED QUANTUM DOTS SPONTANEOUS EMISSION WITH METAMATERIAL PERFECT ABSORBERS	77
ABSTRACT.....	77
1. INTRODUCTION	78
2. MATERIALS AND METHODS.....	80
3. CONCLUSIONS	87
ACKNOWLEDGMENTS	88
REFERENCES	88
VI. SELECTIVE CHIRAL SPONTANEOUS EMISSION OF QUANTUM DOTS ON CHIRAL METASURFACE	92
ABSTRACT.....	92
1. INTRODUCTION	93
2. CHIRAL METASURFACE DESIGN AND CHARACTERIZATION	95
3. SELECTIVE QUANTUM DOTS RCP AND LCP SPONTANEOUS EMISSION CONTROL.....	99
4. CONCLUSIONS	103
5. METHOD	104
ACKNOWLEDGMENTS	106
REFERENCES	106
SECTION	
2. CONCLUSION	108
BIBLIOGRAPHY.....	112
VITA	113

LIST OF ILLUSTRATIONS

	Page
PAPER I	
Figure 1. (a) Schematic of the V-groove array on an aluminum layer with silicon substrate. (b) Schematic of the optical reflection mode for the bright field and dark field illumination. Angle 1 represents the collection angle of the objective lens while angle 2 is the incident angle of the dark field condenser lens. (c-j) Cross-section SEM images of the fabricated V-groove arrays with the same groove period of 250 nm and eight different groove depths from 76 nm to 231 nm.	11
Figure 2. (a) Measured (black solid line) and simulated (red solid line) optical reflectance spectra under bright field illumination for the eight V-groove arrays with different groove depths from 76 nm to 231 nm. The simulation depth are also shown in the Fig. (b) Measured (black solid line) and simulated (red solid line) scattering intensity spectra under dark field illumination for the eight V-groove arrays. Insets show the corresponding bright field or dark field optical microscope images of $20 \times 20 \mu\text{m}^2$ V-groove arrays. (c) Dependence of red-shift of the plasmonic resonance dip (red) and the plasmonic resonance peak (blue) on the groove depth.	12
Figure 3. Measured and simulated results in the CIE 1931 xy chromaticity coordinates for the eight V-groove arrays with the increased groove depth from 76 nm to 231 nm.	13
Figure 4. Cross sections of the time-averaged magnetic field (color map) and electric displacement (white arrows) distributions for the V-groove metasurface with depth of 150 nm at the resonance wavelength, under (a) the bright field illumination with vertical incident angle and (b) the dark field illumination with oblique incident angle of 70 degrees.	13
Figure 5. Simulated incident angle dependent (a) optical reflection spectra under the bright field illumination and (b) optical scattering intensity spectra under the dark field illumination for the V-groove metasurface with depth of 100 nm.	15

- Figure 6. (a) Schematic of two-dimensional V-groove array on an aluminum layer with silicon substrate. The grooves in different directions have different depth, thus sample can appear different color when incident by different polarization light. (b) Simulation results of reflectance spectrum of sample illuminated by light with different polarization. 16
- Figure 7. (a) Original landscape art painting with various colors. (b) The measured bright field microscope image of the plasmonic painting under the horizontal linear polarization (white arrow) with size of $40 \times 50 \mu\text{m}^2$. (c) The measured dark field microscope image. (d)-(f) SEM images of the fabricated plasmonic painting sample with V-groove arrays of different depths. 18
- Figure 8. (a) Color response of one-dimensional groove sample illuminated by light with different polarization changes from vertical to the groove to parallel to the groove. The polarizer was placed in the incident beam path. (b) Different polarization color images of one-dimensional groove in the dark field setting with polarizer in the reflected beam path. 19

PAPER II

- Figure 1. (a) Schematic of square-shaped disk array on aluminum surface. (b-d) SEM images of square-shaped disk arrays fabricated on $h = 250 \text{ nm}$ thick aluminum film with different geometric parameters of (b) $P = 400 \text{ nm}$, $d = 135 \text{ nm}$, $w = 245 \text{ nm}$, (c) $P = 400 \text{ nm}$, $d = 227 \text{ nm}$, $w = 200 \text{ nm}$, and (d) $P = 400 \text{ nm}$, $d = 82 \text{ nm}$, $w = 245 \text{ nm}$ 31
- Figure 2. Measured (black solid line) and simulated (red dashed line) optical reflection spectra of three groups of disk array samples (a) by varying disk etching depth d from 82 nm to 135 nm with constant $P = 400 \text{ nm}$ and $w = 245 \text{ nm}$, (b) by changing disk width w from 250 nm to 200 nm with constant $P = 400 \text{ nm}$ and d as a function of w , and (c) by changing period P from 350 nm to 600 nm with constant $d = 82 \text{ nm}$ and $P - w = 147 \text{ nm}$ 32
- Figure 3. Measured (black square) and simulated (red circle) results in the CIE 1931 xy chromaticity coordinates for three groups of disk array samples by changing (a) d , (b) w , and (c) P 33
- Figure 4. (a) Cross section of the time-averaged magnetic field (color map) and electric displacement (red arrows) distributions for a selected disk array (with $P = 400 \text{ nm}$, $w = 245 \text{ nm}$ and $d = 114 \text{ nm}$) at the resonance wavelength. (b) Cross section of the time-averaged optical power flow vector distribution. 34

Figure 5. Color palettes generated from square-shaped disk arrays with varying disk etching depth d , disk width w and unit cell period P ...	34
Figure 6. (a) Original landscape painting with different colors. (b) The measured bright-field optical microscope image of the plasmonic painting with size of $50\ \mu\text{m}$ by $35\ \mu\text{m}$. (c) SEM image of the fabricated plasmonic painting with various disk array patterns. (d) SEM image of the area outlined in panel (c). (e) SEM image of the area outlined in panel (d).	36
Figure 7. Simulated incident angle dependent (a) TE and (b) TM polarized optical reflection spectra for a selected disk array (with $P = 400\ \text{nm}$, $w = 245\ \text{nm}$ and $d = 114\ \text{nm}$). (c) Incident angle resolved chromaticity coordinates calculated from the reflection spectra for TE (red circle) and TM (black square) polarizations.	37

PAPER III

Figure 1. Multilayer metamaterial nanostructures.	47
Figure 2. Spontaneous emission enhancement of QDs on a multilayer structure.	49
Figure 3. Spontaneous emission enhancement of QDs on multilayer gratings.	53
Figure 4. Simulated electric field magnitude distribution of QDs with emission wavelengths of 550, 610, and 680 nm on top of a multilayer (a) and at 680 nm on and inside a multilayer grating (b).	54

PAPER IV

Figure 1. (a) Schematic of 2D multilayer nano-cavity made of alternate Au (4nm) and Al_2O_3 (6nm). Period of the multilayer is denoted by a , and dipole emitter is illustrated by the red dot. (b) IFC for multilayer metamaterials calculated from FFT (bronze colored lines) and EMT (white lines) at wavelength of 850 nm. The yellow circles represent the extracted resonating wavevectors of the designed cavity modes and the green circle represents the light cone of vacuum. (c) Eigen mode magnetic field distribution for cavity with size ($82.2\ \text{nm} \times 60\ \text{nm}$). (d, e) The magnetic field profiles along the horizontal and vertical middle line of eigen mode are fitted to extract the wavevectors inside each cavity.	66
Figure 2. Fundamental electric (a) and magnetic (b) mode excited by an electric dipole placed inside each cavity.	70

Figure 3. (a) Purcell factors of hyperbolic metamaterial nano-cavities as a function of k/k_0 . The red square and dot represent the Purcell factors calculated by total emission power with and without metal loss. The black up- and down- pointing triangle represent the Purcell factors calculated by Eq. (3) (b) Mode area as a function of wavevector. (c) Red dots represent Q_{rad} with the unique scaling law of $Q_{rad} \sim (k/k_0)^3$ 72

Figure 4. (a) Schematic of different dipole positions and orientations when it is coupled to the hyperbolic multilayer nano-cavity. (b) Dependence of Purcell factor on the dipole orientation, where θ is the angle between the dipole moment and the local electric field vector. $\theta = 0^\circ/180^\circ$ (90°) represents dipole moment along z (x) direction. (c, d). Calculated Purcell factor for dipole positions on top of the nanocavity moving along x/z directions (indicated by the white dashed lines). 73

PAPER V

Figure 1. (a), Schematic view of metamaterial PAs made of hexagonal array of holes on the Ag -SiO₂ -Ag three-layer structure with the spin-coated QD-polystyrene film. (b), SEM cross section of metamaterial PA fabricated by FIB with period of 230 nm and hole radius of 65 nm. (c-f), SEM images of four structures with different lattice geometrical parameters (c: P = 155 nm, r = 40 nm; d: P = 230 nm, r = 65 nm; e: P = 280 nm, r = 80 nm; f: P = 315 nm, r = 90 nm). 81

Figure 2. Measured optical reflectance spectra of QD-polystyrene coated metamaterial PA1 (a), PA2 (b), PA3 (c) and PA4 (d) with different geometrical parameters as designed and fabricated in Fig.1 82

Figure 3. Normalized TCSPC histograms and fitting results for QDs photoluminescence decays on the four metamaterial PAs and glass substrate. 83

Figure 4. Experiment and simulation results for spontaneous emission rate enhancement (a, b) and photoluminescence intensity enhancement (c, d) of the four metamaterial PAs coupled with QDs at 620 nm. 85

Figure 5. Top (a) and side (b) views of magnetic field intensity distribution excited by a z-polarized electric dipole emitter at 620nm, located at the center of the hole and 10nm above the surface of the four PAs. (c-d) shows the top and side views of electric field intensity distribution. 86

PAPER VI

- Figure 1. (a) 3D schematic of ellipse array multilayer structures consists of 45 nm top Au, 100 nm SiO₂ spacer and 130 nm Au reflector on silicon base. (b) Parameter of tilted ellipse enantiomer A and B with period P_x and P_y. Ellipse short and long axis are noted as a and b. θ is ellipse tilted angle. (c) Top view of SEM picture of two enantiomers. (d) Tilted view at 53 degree of SEM picture of two enantiomers. 95
- Figure 2. (a, b) Experimental (solid line) and simulation (dashed line) reflectance results of two enantiomers. (c) Experimental CDR of two enantiomers. (d, e) Experimental and simulation LCP and RCP component reflected spectrum of two enantiomers. (f). Electric field mode distribution of two enantiomers at different LCP and RCP incidence at resonance wavelength 725nm. The horizontal cross section is set 10nm beneath the top Au layer. (g) Electric field mode distribution at the vertical cross section at the right border of unit cell. 98
- Figure 3. (a) Top view of fabricated windmill pattern. (Scale bar: 10um (a)) (b) Windmill pictures with incidence LCP and RCP light of difference wavelength. (c) Reflectance difference spectrum with incidence of LCP and RCP light. 99
- Figure 4. (a, b) Reflectance spectrum with LCP and RCP incidence after coating polymer. (c, d) LCP and RCP component of photo luminescent emitted from quantum dot placed in two enantiomers. (e, f) Fluorescence lifetime decays of LCP and RCP emission light from two enantiomers. (f) LCP and RCP intensity difference of two enantiomers. (g) Experimental CD_PL of two enantiomers. (h) Simulated CD_PL of two enantiomers when QDs placed above Au top surface and in the middle SiO₂ layer. 102

SECTION

1. INTRODUCTION

1.1. BACKGROUND

Plasmon polaritons or plasmons are a collective oscillation movement of free electrons in metal at optical frequencies [1]. The free electron gas movement in metal play an important role in the interaction between metal and electromagnetic radiation. The metal's complex dielectric function is used to describe the physic of this free electron gas movement. Drude oscillator model and Lorentz oscillator model are well known simple classical microscopic theory that illustrate the metal's frequency dependent complex dielectric function [2]. The complex dielectric function frequency dependent behavior makes the metal property at optical frequencies behave totally different with that at other spectral ranges with lower frequency such as infrared and microwaves. The plasmons are unique characteristic interaction of metal or metal nanostructure with light. The scale invariance of Maxwell's equations is not useful between optical frequencies and other frequencies which make the model experiments at optical frequencies distinct from experiments operated at lower frequencies. This novel property makes the so called plasmonics or nanoplasmonics a rapid growing research field over the past few years [3]. Surface and volume charge density oscillations with distinct resonance frequencies can be sustained by free electron gas in metal. At the interface between a metal and a dielectric propagating surface charge density oscillation which are spatially confined near the meatal surface are very useful to create large optical near field intensity. Many innovative concepts

and applications have been developed such as perfect absorber, structural color printing, quantum emitters spontaneous emission enhancement.

In this dissertation two of the most important applications will be addressed. The first application is structure coloring and the other is to control the spontaneous emission rate of quantum emitters such as quantum dot, color center, etc.[4].

For particular interface shape such as nanogrooves or nanowires both propagating and non-propagating surface plasmon modes are supported. Extreme local charge accumulations accompanied by strongly enhanced optical fields can occur in particular shapes. In this case nanogrooves will be used as a fundamental perfect absorber structure unit for structural color printing. The details will be discussed in the first and two research projects.

For the alternative metal-dielectric multilayer, the electric permittivity can be adjusted arbitrarily to create artificial dielectrics, the so-called metamaterials. Also random metal-dielectric composites can exhibit artificial desired permittivity according to Metal-Dielectric composites mixing rules [5]. In the case of multilayer structures, artificial epsilon-near-zero metamaterial can be designed to support large local density of states and enhance quantum dot (QD) spontaneous emission rate. The Purcell effect [6] of quantum dot spontaneous emission with Ag-SiO₂ multilayer metamaterial nanostructures will be demonstrated by experiment and simulation in the third and fourth of research projects.

In the case of small subwavelength metal particle, the free electron gas oscillations will be confined in the three dimensions. The overall free electron gas oscillates around the positively charged lattice of the metal particle and give rise to non-propagating localized or particle-plasmon resonances depending on particle geometry at specific resonance

frequency. For metallic nanoholes the same localized plasmon can be found. The two-dimensional nanohole arrays in single metal layer or multi metal-dielectric layers sustain large localized plasmon resonance and the resulted high electric field density can support large density of states, so spontaneous emission rate of quantum emitters is greatly enhanced. This situation will be discussed in the fifth research project.

Also tilted ellipse array on trilayer can be used to achieve chiral-selective plasmonic absorber. Chirality is a fascinating geometrical property that chiral object and its mirror image cannot coincide with each other by rotational or translational operation. Both light and material can be chiral and their interaction such as circular dichroism have been investigated intensively. However, the control of chiral spontaneous emission of dipole emitters still remains open. Use chiral-selective plasmonic absorber based on tilted ellipse array on trilayer to control the chiral spontaneous emission property of dipole emitters such as quantum dots will be demonstrated in the sixth research project. These results will advance many applications in light-emitting devices, nanoscale lasers, quantum electrodynamics, and quantum information processing.

1.2. ORGANIZATION OF DISSERTATION

The main objective of this research is to investigate the application of plasmonic metamaterials: structure coloring and controlling the spontaneous emission rate of quantum emitters.

The first research topic is to demonstrate structural color printing based on all-aluminum plasmonic V-groove metasurfaces under both bright field and dark field illumination conditions. A broad visible color range is realized with the plasmonic V-

groove arrays etched on aluminum surface by simply varying the groove depth while keeping the groove period as a constant. Polarization dependent structural color printing is further achieved with interlaced V-groove arrays along both the horizontal and vertical directions. These results pave the way towards the use of all-aluminum structural color printing platform for many practical applications such as security marking and information storage.

The second research topic is to demonstrate an all-metal structural color printing platform based on aluminum plasmonic metasurfaces with high color performance using only one-step etching process on aluminum surface. A wide visible color range is realized with the designed metallic square-shaped disk arrays by simply adjusting geometrical parameters of the disk etching depth, disk width and unit cell period. The demonstrated all-metal microscale structural color printing on aluminum surface offers great potential for many practical color related applications.

The third research topic aims to demonstrate the Purcell effect of quantum dot (QD) spontaneous emission with Ag-SiO₂ multilayer metamaterial nanostructures in experiment and simulation. A broadband enhanced spontaneous emission rate of QDs is observed due to large local density of states in the epsilon-near-zero and hyperbolic regions of multilayer structures. Multilayer gratings are utilized to further enhance the QD spontaneous emission as the QDs located inside the grating grooves strongly interact with high-k coupled surface plasmon polariton modes. Photoluminescence decay measurements are in good agreement with both analytical treatment with a nonlocal effect and three-dimensional finite-element simulation. Detailed studies of QD position and polarization effects on emission rate enhancement for multilayer and multilayer grating nanostructures provide important

insight for understanding the coupling mechanisms of emitter-multilayer interaction and the engineering of local density of states in metamaterial nanostructures. These results will advance many applications in light-emitting devices, nanoscale lasers, quantum electrodynamics, and quantum information processing.

The fourth research topic aims to investigate the anomalous power law for the Purcell factor of cavity wavevector with dipole excitation. To control the spontaneous emission rate of dipole emitters, resonant cavity is widely used to provide large electromagnetic mode confinement and thus results in the enhanced Purcell effect. Here, hyperbolic metamaterial cavities with different wavevectors are designed to have identical fundamental mode at the same resonant frequency. Different from conventional photonic and plasmonic cavities, a fifth power law $PF \sim (k/k_0)^5$ for small wavevectors and a square law $PF \sim (k/k_0)^2$ for large wavevectors have been demonstrated. The unique optical properties and Purcell factor scaling law of hyperbolic metamaterial cavities will greatly benefit the applications in cavity electrodynamics, quantum optics, single photon sources, on-chip quantum computing and circuits.

The fifth research topic aims to enhance the spontaneous emission rate and photoluminescence intensity of CdSe/ZnS quantum dots spin-coated on the absorbers top surface. Metamaterial perfect absorbers were made of hexagonal array of holes on Ag-SiO₂-Ag thin films. Perfect absorption of incoming light happens at the wavelength where the impedance is matched to that of the free space. When QDs strongly excite both the electric and magnetic resonances at this perfect absorption wavelength, significant Purcell effect on the spontaneous emission process and enhanced radiative outcoupling of photoluminescence intensity are expected. For perfect absorbers with near-unity absorption

at the QDs emission wavelength of 620 nm, 5-fold Purcell enhancement of spontaneous emission rate and 3.6-fold enhancement of photoluminescence intensity are demonstrated in the time-resolved photoluminescence experiments, which are in good agreement with three-dimensional finite-difference time-domain simulation. These results will advance the understandings and applications of the metamaterial PAs-based light harvesting and emitting devices.

The sixth research topic aims to control chiral spontaneous emission of dipole emitters using chiral-selective plasmonic absorber based on tilted ellipse array on trilayer. The associated chiral-selective absorption band that strongly absorb one-handed circular polarized light and reflect the other results in significant circular dichroism. By position the QD on the top of metasurface, we demonstrate a sharp difference in their interaction with the right-hand polarized (RCP) and left-hand polarized (LCP) metasurface modes. The difference in RCP and LCP spontaneous emission lifetime and photoluminescence intensity were demonstrated experimentally. Theoretical mode analysis were conducted to explain the mode coupling mechanism. Our observations of chiral mode engineering for spontaneous emission control enable a variety of promising applications in active polarization manipulation, chiral imaging and sensing, chiroptical spectroscopy, Stereochemical enantiomer sensors.

The outcomes of the above research topics are expected to advance the knowledge of plasmonic metamaterials applications.

PAPER

I. REALIZING STRUCTURAL COLOR GENERATION WITH ALUMINUM PLASMONIC V-GROOVE METASURFACES

Wei Wang,¹ Daniel Rosenmann,² David A. Czaplewski,² Xiaodong Yang,¹ And Jie Gao¹

¹Department of Mechanical and Aerospace Engineering, Missouri University of Science and Technology, Rolla, MO 65409

²Center for Nanoscale Materials, Argonne National Laboratory, Argonne, IL 60439, USA

ABSTRACT

The structural color printing based on all-aluminum plasmonic V-groove metasurfaces is demonstrated under both bright field and dark field illumination conditions. A broad visible color range is realized with the plasmonic V-groove arrays etched on aluminum surface by simply varying the groove depth while keeping the groove period as a constant. Polarization dependent structural color printing is further achieved with interlaced V-groove arrays along both the horizontal and vertical directions. These results pave the way towards the use of all-aluminum structural color printing platform for many practical applications such as security marking and information storage.

Keywords: Subwavelength structures; Surface plasmons; Metamaterials; Color.

1. INTRODUCTION

Recently, various types of structural color printing techniques have been introduced to generate a wide range of visible colors with great potential to replace the traditional pigment-based color printing technology [1-4]. Among these techniques, plasmonic metamaterials and metasurfaces are becoming more attractive for structural color applications due to their advanced light manipulation capabilities [5-8]. Plasmonic metasurfaces are also widely used to generate color holography which is one kind of structural color printing technique [9-11]. Different kinds of plasmonic nanostructures have been employed to generate high resolution structural colors, including one-dimensional gratings [12-14], hole arrays [1-3, 15, 16], antenna arrays [7, 17-20], metal-insulator-metal structures [6, 21-25], and combined nanodisk and nanohole arrays [5, 26, 27]. Optical resonances across the whole visible spectrum can be achieved by adjusting the geometrical parameters of the plasmonic nanostructures, according to the tunable spectral responses of propagating surface plasmons (SP) [4, 28-32], localized surface plasmon resonances (LSPR) [4, 21, 33-38], and Fabry-Pérot cavity modes [4, 39]. Plasmonic color generation has been utilized in obtaining highly saturated color with narrow spectral width [4, 6, 40, 41], color filtering with extraordinary optical transmission [4, 12-14], high-resolution color imaging [4, 21, 39, 42], color filtering with polarization dependence [4, 32, 33, 43-45], and angle-insensitive structural colors [4, 39, 45]. Noble metals such as silver [13, 23, 26, 34] and gold [6] are widely used in previous plasmonic color printing works due to their lower ohmic losses in the visible spectrum. However, silver is not ideal for color generation because it is susceptible to oxidation and sulphidation [5, 17, 46] and gold has limitations for rendering blue colors due to the interband transition [4, 6, 47, 48].

Alternatively, aluminum has been used as an attractive plasmonic material for structural color generation due to its excellent optical response over the entire visible spectrum, chemical and thermal stability due to its self-limiting impermeable native oxidation layer, low cost, and complementary metal oxide semiconductor (CMOS) compatibility [7, 15, 16, 24, 25, 48, 49]. Although many aluminum based metasurfaces with plasmonic structures such as metal-insulator-metal structures [6, 13, 14, 22-25] or combined nanodisk and nanohole arrays [5, 26, 27] have been proposed for color printing, the complex fabrication process will not only increase the production cost but also degrade the color performance.

Here we propose and demonstrate structural color printing with high color performance based on plasmonic V-groove metasurfaces of an aluminum surface, by using a simple but efficient one-step focused ion beam milling process. A wide visible color range can be realized under both bright field and dark field illumination conditions by only varying the groove depth while maintaining a constant groove period. The optical mode analysis in aluminum V-groove arrays reveals the excitation of electric dipole and magnetic dipole resonances for the structural color generation. The incident angle dependent optical reflection and scattering from the V-groove metasurface color printing platform is also studied. Furthermore, polarization dependent structural color printing under both bright field and dark field illumination conditions is demonstrated with interlaced V-groove arrays along both the horizontal and vertical directions. The demonstrated all-aluminum structural color printing based on plasmonic V-groove metasurfaces provides great opportunities for many color related applications such as security marking, information storage, and microscale imaging.

2. METASURFACE FABRICATION AND CHARACTERIZATION

A typical one-dimensional V-shaped groove array on an aluminum surface designed as gap surface plasmon nanostructures for structural color printing is schematically illustrated in Fig. 1(a). By adjusting the groove depth, d , while keeping the groove period, p , constant, the plasmonic resonance frequency of the V-groove etched on the aluminum film with thickness, h , can be tuned across the whole visible spectrum and thus a wide visible color range can be realized. The designed aluminum plasmonic metasurfaces for color printing are fabricated as follows. A 250 nm aluminum film is deposited on a silicon wafer using a Lesker PVD250 electron-beam evaporator at a rate of 12 Å/sec. The designed V-groove arrays are then directly milled on the aluminum surface by a focused ion beam (FIB) milling process (FEI Helios Nanolab 600 DualBeam) with a gallium ion current of 9.7 pA and an accelerating voltage of 30 KeV. The groove period, p , is selected as 250 nm and the groove depth, d , is increased from 76 nm to 231 nm. Figs. 1(c)-1(j) are the cross-section SEM images of the fabricated V-groove arrays with eight groove depths from 76 nm to 231 nm at a tilted view angle of 52 degrees. During the FIB process, straight line patterns with designed width of 10 nm are milled on the aluminum surface. By controlling the ion beam exposure time, V-grooves with various depths are directly formed. The measured side wall angle of the V-groove is around 73 degrees. As shown in Figs. 1(c) and 1(d), when the groove depth is small, the bottom tip of the fabricated V-groove is not very sharp, but this geometrical imperfection will not affect the color performance since the groove depth is the major controlling parameter for the plasmonic spectral resonance.

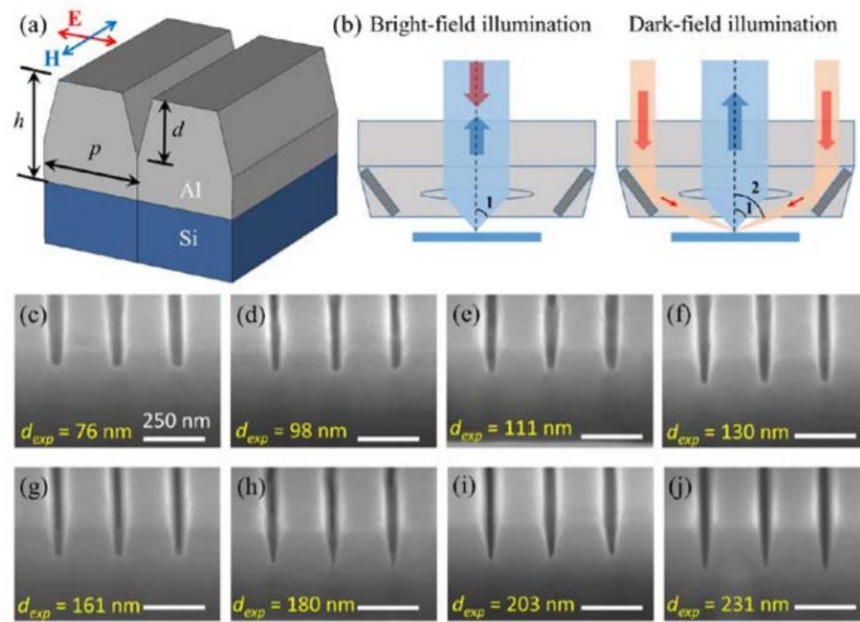


Figure 1. (a) Schematic of the V-groove array on an aluminum layer with silicon substrate. (b) Schematic of the optical reflection mode for the bright field and dark field illumination. Angle 1 represents the collection angle of the objective lens while angle 2 is the incident angle of the dark field condenser lens. (c-j) Cross-section SEM images of the fabricated V-groove arrays with the same groove period of 250 nm and eight different groove depths from 76 nm to 231 nm. Scale bars: 250 nm.

The optical reflection and scattering response from the fabricated V-groove arrays are measured under both bright field and dark field illumination conditions. Fig. 1(b) is the schematic of a typical optical reflection mode for the bright field and dark field illumination through a 20x microscope objective lens with $NA = 0.4$ (Nikon BD Plan). Under bright field illumination condition, the incident light is focused through the central lens and the reflected light from the metasurface is collected by the same optical path at a half Angle 1 of 23.6 degrees. Under dark field illumination condition, the incident light is focused onto the metasurface through the annular condenser lens at an incident Angle 2 around 70 degrees, and the back-scattered light from the sample is collected by the central lens in a confocal setup. Due to the limited penetration depth in the thick aluminum film for incident

light in the visible range, optical transmission from the V-groove metasurfaces will be effectively blocked. With the p-polarized light (where the electric field is perpendicular to the groove direction), a gap surface plasmon mode localized inside the V-groove will be excited. Depending on the groove depth, plasmonic modes at various resonance wavelengths will be realized across the visible range to provide different reflective colors.

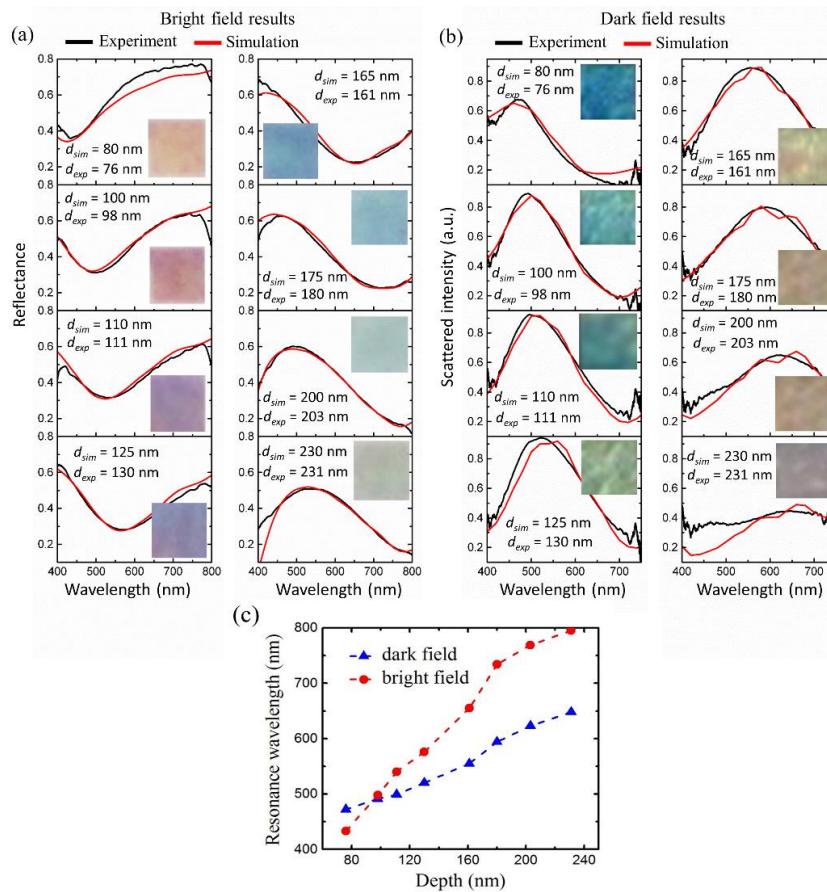


Figure 2. (a) Measured (black solid line) and simulated (red solid line) optical reflectance spectra under bright field illumination for the eight V-groove arrays with different groove depths from 76 nm to 231 nm. The simulation depth are also shown in the Fig. (b) Measured (black solid line) and simulated (red solid line) scattering intensity spectra under dark field illumination for the eight V-groove arrays. Insets show the corresponding bright field or dark field optical microscope images of $20 \times 20 \mu\text{m}^2$ V-groove arrays. (c) Dependence of red-shift of the plasmonic resonance dip (red) and the plasmonic resonance peak (blue) on the groove depth.

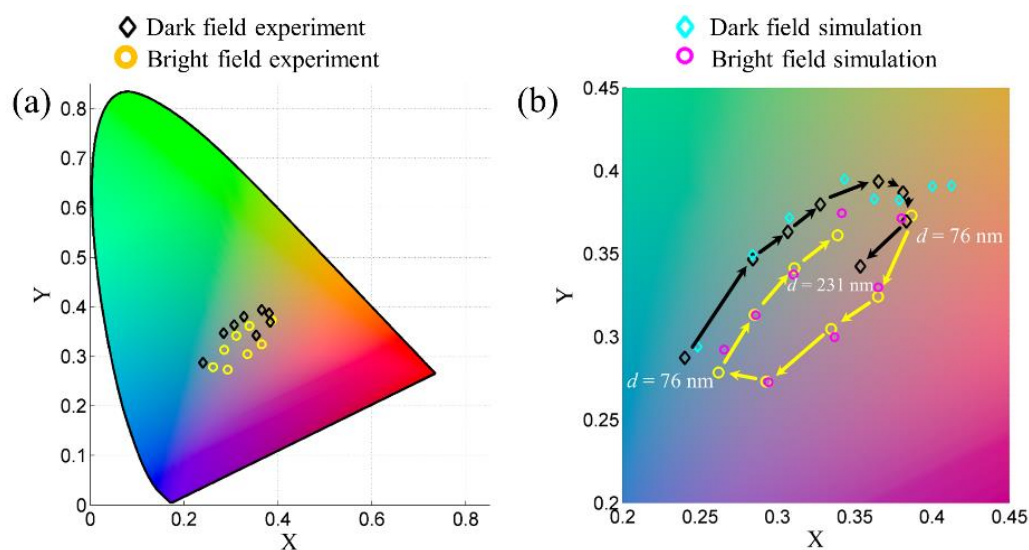


Figure 3. Measured and simulated results in the CIE 1931 xy chromaticity coordinates for the eight V-groove arrays with the increased groove depth from 76 nm to 231 nm. The circles and diamonds represent the bright field and dark field results, respectively.

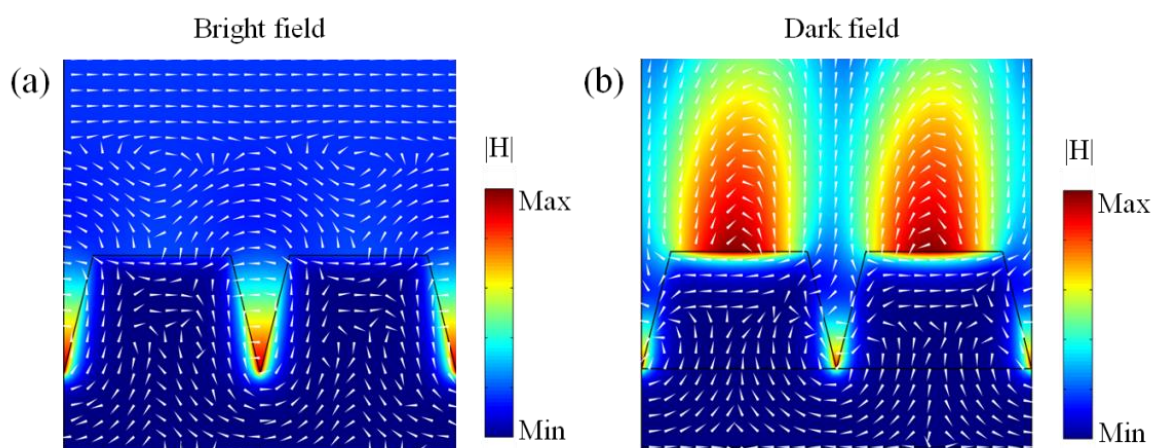


Figure 4. Cross sections of the time-averaged magnetic field (color map) and electric displacement (white arrows) distributions for the V-groove metasurface with depth of 150 nm at the resonance wavelength, under (a) the bright field illumination with vertical incident angle and (b) the dark field illumination with oblique incident angle of 70 degrees.

The optical reflectance and scattering intensity spectra from the fabricated V-groove arrays under bright field and dark field illumination are obtained within the visible wavelength range from 400 nm to 800 nm with a halogen lamp and an optical spectrometer (LR1, ASEQ instruments). Each fabricated V-groove metasurface has an area of $20 \times 20 \mu\text{m}^2$ in the measurements. Fig. 2 summarizes the measured optical reflection spectra under bright field illumination and the optical scattering intensity spectra under dark field illumination, as well as the corresponding microscope images shown in the insets, for the eight V-groove arrays shown in Figs. 1(c)-1(j) with different groove depths from 76 nm to 231 nm. The bright field reflectance spectra as shown in Fig. 2(a) exhibit a red-shifted plasmonic resonance dip changing from 433 nm to 795 nm. The reflective colors also change from yellow, magenta to cyan as the groove depth is increased, which are the primary colors of CMYK system. The simulation results calculated from finite-difference time-domain (FDTD) method are also plotted. In the bright field reflection simulation, a plane wave impinges vertically on the metasurface and the permittivities of aluminum (imaginary part multiplied by factor of 3 to account for fabrication-induced losses) and silicon substrate are obtained from the refractive index database [46]. In Fig. 2(b), the dark field scattering intensity spectra from the same set of V-groove arrays are presented. The spectral resonance peak varies from 474 nm to 656 nm as the groove depth is increased. The scattering colors also change from blue, green to orange, which cover the primary colors of the RGB system. It is noted that for the V-groove arrays with the depth of 250 nm, the resonance peak is shifted above 600 nm. However, the resonance peak is very broad with low scattering intensity so that grayish color is obtained. As the groove depth is increased, the scattering intensity contrast becomes smaller and the scattering spectrum

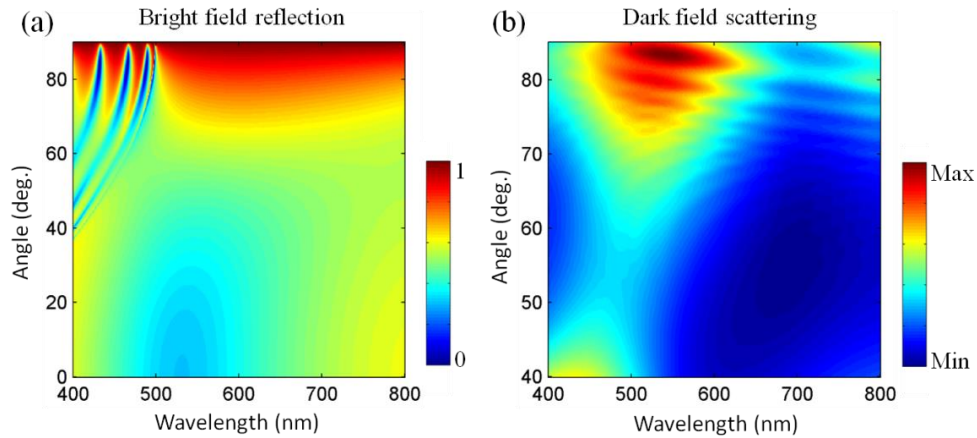


Figure 5. Simulated incident angle dependent (a) optical reflection spectra under the bright field illumination and (b) optical scattering intensity spectra under the dark field illumination for the V-groove metasurface with depth of 100 nm.

gets broader, because more optical energy in a wider wavelength range is absorbed due to the adiabatic nanofocusing [50]. The dependence of the red-shift of plasmonic resonance dip and plasmonic resonance peak on the groove depth are shown in Fig. 2(c). These results are applied to the final plasmonic color painting images. For the large depth cases in the dark field setting, because the energy penetrated through the Al film and dissipated in the Si substrate so the scattered signal is weak. Increase the aluminum film thickness may decrease the energy penetrated into the Si substrate and thus increase the scattered density. To further improve the color contrast changing material from aluminum to silver with low loss will improve the color performance, but silver should be protected by additional layer from oxidation and sulphidation. In the dark field scattering simulation, the metasurface is illuminated by a plane wave with an oblique incident angle of 70 degrees. The back scattered light in the simulation is collected over a conical solid angle corresponding to the numerical aperture of the 20x microscope objective lens used in the experiment. The far field scattering intensity is calculated and integrated within the half angle of 23.6 degrees

as illustrated in Fig. 1(b). A good match between the experimental and simulation results for both the bright field and dark field results are found in Fig. 2. The measured reflection spectra and scattering intensity spectra depicted in Fig. 2 are further converted as the discrete points in the CIE 1931 xy chromaticity coordinates based on color theory in Fig. 3, illustrating the color gamut of the fabricated V-groove metasurfaces. Fig. 3(b) shows the zoomed in data area in Fig. 3(a), together with the simulation results. It is shown that the chromaticity coordinates for the bright field reflection results evolve in a clockwise fashion while the dark field scattering results vary in a counterclockwise way, as the groove depth is increased. All the coordinates are around the achromatic point, demonstrating a large degree of the color range tuning for the designed V-groove metasurfaces.

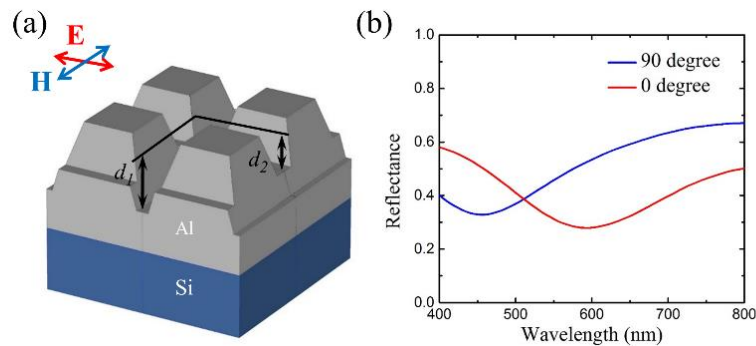


Figure 6. (a) Schematic of two-dimensional V-groove array on an aluminum layer with silicon substrate. The grooves in different directions have different depth, thus sample can appear different color when incident by different polarization light. (b) Simulation results of reflectance spectrum of sample illuminated by light with different polarization. Different polarization illumination results in different colors.

For the purpose of understanding the physical mechanism of the gap surface plasmon modes localized inside the V-groove nanostructure, time-averaged magnetic field (color map) and electric displacement (white arrows) distributions for the V-groove with

depth of 150 nm at the resonance wavelength are plotted in Fig. 4 under both the bright field and dark field illumination. As shown in Fig. 4(a) under the bright field illumination with vertical incident light, strong magnetic dipole resonance inside the V-groove is observed with the concentrated magnetic field surrounded by an electric displacement flow loop. At the same time, an electric dipole resonance is also excited on the top surface of the aluminum ridge. The excitation of the gap surface plasmon mode within the aluminum V-groove provides strong optical absorption for the vertical incident light at the resonance wavelength so that the subtractive color can be observed in the bright field reflection spectrum from the metasurface. Fig. 4(b) plots the optical mode distributions for the V-groove under the dark field illumination with oblique incident angle of 70 degrees. The magnetic dipole resonance confined inside the groove gets very weak, while a strong magnetic dipole resonance occurs around the top aluminum-air interface of the aluminum ridge, together with the electric dipole resonance at the top aluminum surface. It is observed that the electromagnetic energy is scattered away from the V-groove into the far field above the groove at the resonance wavelength. Therefore, the additive color can be obtained in the dark field scattering spectrum above the metasurface. The above mode analysis indicates that different structural colors will be realized under the bright field as well as under dark field illumination conditions.

The incident angle dependent optical spectral response is further studied in simulation for the V-groove metasurface with depth of 100 nm, under both the bright field and dark field illumination conditions. For the calculated optical reflection spectra under bright field illumination as shown in Fig. 5(a), when the incident angle changes from 0 degree (vertical direction) to around 50 degrees, the reflection resonance dip almost

remains at the same wavelength, giving unchanged color for different view angles. When the incident angle is larger than 50 degrees, the gap surface plasmon mode supported inside the V-groove disappears and the metasurface behaves like a broadband mirror. For the optical scattering intensity spectra under the dark field illumination as plotted in Fig. 5(b), the scattering resonance peak almost linearly red-shifts to longer wavelength when the incident angle increases, and the resonance peak width and scattering intensity also depend on the incident angle. It is shown that the scattering intensity will reach its maximum value at the incident angle of 84 degrees.

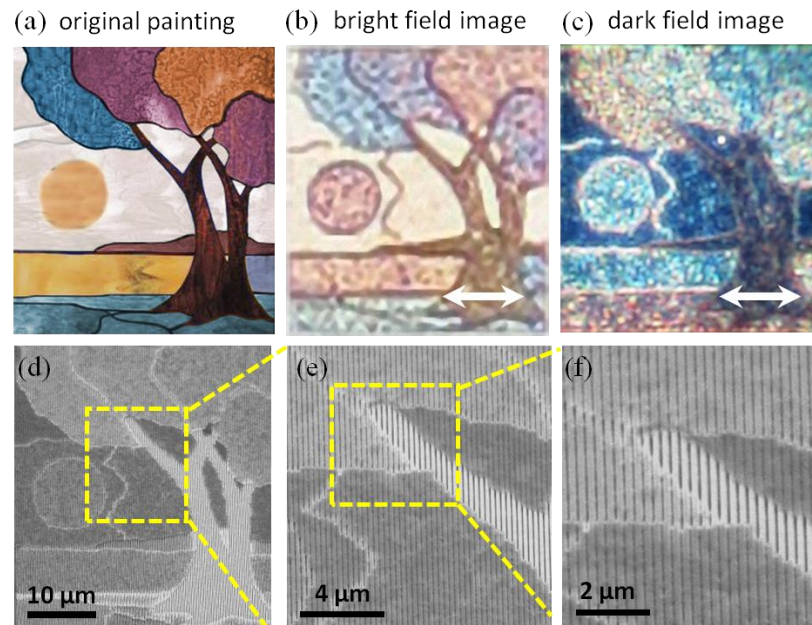


Figure 7. (a) Original landscape art painting with various colors. (b) The measured bright field microscope image of the plasmonic painting under the horizontal linear polarization (white arrow) with size of $40 \times 50 \mu\text{m}^2$. (c) The measured dark field microscope image. (d)-(f) SEM images of the fabricated plasmonic painting sample with V-groove arrays of different depths. SEM image in panel (f) is tilted at a view angle of 52 degrees.

When the grooves of the sample in different direction have different depth, sample can appear different color when incident by different polarization light. It is worth noting that even when the sample is illuminated by unpolarized light, the reflected light with different polarization also have different color which will be shown in the experiment results. For two-dimensional simulation, the demonstration results are shown in Fig. 6(b). The reflectance spectrum is different when the sample is illuminated by light with different polarization. The simulation schematic is shown in Fig. 6(a). The side wall angle is 73 degree. Due to the fabrication issue the V-groove will not be perfect, the groove bottom should has certain gap, the two-dimensional simulation show the real case. For polarization 0 degree the bottom width of the pyramid is 222 nm, the groove depth d_1 is 155 nm. For polarization 90 degree the bottom width of the pyramid is 190 nm, the groove depth d_2 is 100 nm. The simulation results are shown in Fig. 6(b).

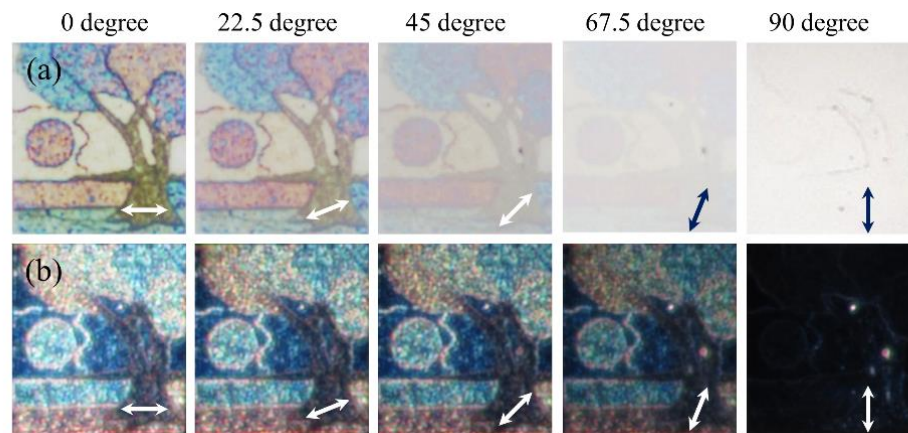


Figure 8. (a) Color response of one-dimensional groove sample illuminated by light with different polarization changes from vertical to the groove to parallel to the groove. The polarizer was placed in the incident beam path. (b) Different polarization color images of one-dimensional groove in the dark field setting with polarizer in the reflected beam path. The reflected beam from the sample is highly polarized.

3. PLASMONIC PAINTING OF COLOR IMAGES

In order to demonstrate the applicability and visual performance of the proposed aluminum plasmonic V-groove metasurfaces for structural color printing applications, a micrometer scale $40 \times 50 \mu\text{m}^2$ plasmonic printed copy of a landscape art painting drawn by ourselves, as displayed in Fig. 7(a), is fabricated. By choosing the V-groove array with certain groove depth in each pixel, the desired colors can be realized with high fidelity and visual contrast. The measured bright field microscope image of the plasmonic painting under the horizontal linear polarization (white arrow) as shown in Fig. 7(b) successfully reproduces the original image features and colors shown in Fig. 7(a). Fig. 7(c) illustrates the measured dark field microscope image, where nearly complementary colors are displayed as expected. The SEM images of the fabricated plasmonic painting sample with vertical V-groove arrays are shown in Figs. 7(d)-7(f). When the polarization is parallel to the grooves, the color will disappear which can be used in security applications. Fig. 8(a) show one-dimensional sample color response illuminated with different polarization in bright and dark field setting. In the bright field setting, the polarizer was placed in the incident beam path. The color will disappear when the polarization is parallel to the grooves. It is worth noting that when the sample was illuminated with unpolarized light, because different polarized beam has different plasmonic resonance, reflected beam with different polarization also have different color. In the dark field setting, the oblique incident beam polarization can't be controlled easily, so the polarizer was placed in the reflection beam path. The results in Fig. 8(b) show that the reflected beam is also highly polarized even when the incident beam is unpolarized because only p-polarized wave can be scattered. Since the current V-groove array works under a certain linear polarization perpendicular

to the groove direction, two-dimensional V-groove arrays along both the horizontal and vertical directions can be interlaced together for displaying images with polarization-dependent colors. Two original landscape art paintings with different color sets are displayed in Fig. 9(a), where the top one is designed to use vertical V-groove arrays under the horizontal linear polarization while the bottom one is for horizontal V-groove arrays under the vertical linear polarization. Fig. 9(b) gives the measured bright field microscope images under two different linear polarizations, showing the vivid image colors switching from one set to another once the linear polarization is tuned from horizontal to vertical (white arrows). The measured dark field microscope images are also switched under orthogonal linear polarization excitation. The SEM images of the fabricated plasmonic painting sample with the interlaced vertical and horizontal V-groove arrays are shown in Figs. 9(d)-9(f). Fig. 10 show two-dimensional sample color response illuminated with different polarization under bright and dark field illumination. When the polarizer rotates, the image will gradually changes from one color to another kind of color. The demonstrated plasmonic painting results indicate that the proposed all-aluminum structural color printing platform based on the V-groove metasurfaces is capable of creating high-resolution color images with high brightness and saturation.

4. CONCLUSIONS

An all-aluminum structural color printing platform based on plasmonic V-groove metasurfaces with high resolution and high color performance have been introduced and demonstrated, by using a one-step focused ion beam milling process. By only adjusting the groove depth, the plasmonic resonances of the V-groove arrays can be tuned across the

whole visible spectrum, resulting in either the subtractive colors obtained from the reflection spectra under the bright field illumination, or the complimentary additive colors resulting from the scattering spectra under the dark field illumination. The reproduced polarization dependent plasmonic paintings of color images under both the bright field and dark field illumination conditions manifest the feasibility and flexibility of all-aluminum plasmonic V-groove metasurfaces for structural color printing applications. The demonstrated aluminum plasmonic V-groove metasurfaces for high-performance and pigment-free structural color generation will open many new possibilities for realizing relevant applications such as security marking, information storage, and microscale imaging.

ACKNOWLEDGMENTS

The authors thank Zhigang Li for the useful discussion and acknowledge the facility support from the Materials Research Center at Missouri S&T. This work was performed, in part, at the Center for Nanoscale Materials, a U.S. Department of Energy, Office of Science, Office of Basic Energy Sciences User Facility under Contract No. DE-AC02-06CH11357.

REFERENCES

- [1] C. Genet and T. W. Ebbesen, "Light in tiny holes," *Nature* 445, 39-46 (2007).
- [2] Q. Chen and D. R. S. Cumming, "High transmission and low color cross-talk plasmonic color filters using triangular-lattice hole arrays in aluminum films," *Opt. Express* 18, 14056-14062 (2010).

- [3] D. Inoue, A. Miura, T. Nomura, H. Fujikawa, K. Sato, N. Ikeda, D. Tsuya, Y. Sugimoto, and Y. Koide, "Polarization independent visible color filter comprising an aluminum film with surface-plasmon enhanced transmission through a subwavelength array of holes," *Appl. Phys. Lett.* 98(9), 093113(2011).
- [4] Z. G. Li, W. Wang, D. Rosenmann, D. A. Czaplewski, X. D. Yang, and J. Gao, "All-metal structural color printing based on aluminum plasmonic metasurfaces," *Opt. Express* 24, 20472-20480 (2016).
- [5] S. J. Tan, L. Zhang, D. Zhu, X. M. Goh, Y. M. Wang, K. Kumar, C. W. Qiu, and J. K. W. Yang, "Plasmonic Color Palettes for Photorealistic Printing with Aluminum Nanostructures," *Nano Lett.* 14, 4023-4029 (2014).
- [6] A. S. Roberts, A. Pors, O. Albrektsen, and S. I. Bozhevolnyi, "Subwavelength Plasmonic Color Printing Protected for Ambient Use," *Nano Lett.* 14, 783-787 (2014).
- [7] J. S. Clausen, E. Hojlund-Nielsen, A. B. Christiansen, S. Yazdi, M. Grajower, H. Taha, U. Levy, A. Kristensen, and N. A. Mortensen, "Plasmonic Metasurfaces for Coloration of Plastic Consumer Products," *Nano Lett.* 14, 4499-4504 (2014).
- [8] Y.-W. Huang, W. T. Chen, W.-Y. Tsai, P. C. Wu, C.-M. Wang, G. Sun, and D. P. Tsai, "Aluminum Plasmonic Multicolor Meta-Hologram," *Nano Lett.* 15, 3122-3127 (2015).
- [9] S. Choudhury, U. Guler, A. Shaltout, V. M. Shalaev, A. V. Kildishev, and A. Boltasseva, "Pancharatnam–Berry Phase Manipulating Metasurface for Visible Color Hologram Based on Low Loss Silver Thin Film," *Adv. Opt. Mater.* 5, 1700196-n/a (2017).
- [10] X. Li, L. Chen, Y. Li, X. Zhang, M. Pu, Z. Zhao, X. Ma, Y. Wang, M. Hong, and X. Luo, "Multicolor 3D meta-holography by broadband plasmonic modulation," *Sci. Adv.* 2(2016).
- [11] W. Wan, J. Gao, and X. Yang, "Full-Color Plasmonic Metasurface Holograms," *ACS Nano* 10, 10671-10680 (2016).
- [12] H. J. Park, T. Xu, J. Y. Lee, A. Ledbetter, and L. J. Guo, "Photonic Color Filters Integrated with Organic Solar Cells for Energy Harvesting," *ACS Nano* 5, 7055-7060 (2011).
- [13] B. B. Zeng, Y. K. Gao, and F. J. Bartoli, "Ultrathin Nanostructured Metals for Highly Transmissive Plasmonic Subtractive Color Filters," *Sci. Rep.* 3, 2840(2013).
- [14] M. J. Uddin, T. Khaleque, and R. Magnusson, "Guided-mode resonant polarization-controlled tunable color filters," *Opt. Express* 22, 12307-12315 (2014).

- [15] S. Yokogawa, S. P. Burgos, and H. A. Atwater, "Plasmonic Color Filters for CMOS Image Sensor Applications," *Nano Lett.* 12, 4349-4354 (2012).
- [16] Z. B. Li, A. W. Clark, and J. M. Cooper, "Dual Color Plasmonic Pixels Create a Polarization Controlled Nano Color Palette," *ACS Nano* 10, 492-498 (2016).
- [17] G. Y. Si, Y. H. Zhao, J. T. Lv, M. Q. Lu, F. W. Wang, H. L. Liu, N. Xiang, T. J. Huang, A. J. Danner, J. H. Teng, and Y. J. Liu, "Reflective plasmonic color filters based on lithographically patterned silver nanorod arrays," *Nanoscale* 5, 6243-6248 (2013).
- [18] T. Ellenbogen, K. Seo, and K. B. Crozier, "Chromatic Plasmonic Polarizers for Active Visible Color Filtering and Polarimetry," *Nano Lett.* 12, 1026-1031 (2012).
- [19] J. Do, M. Fedoruk, F. Jackel, and J. Feldmann, "Two-Color Laser Printing of Individual Gold Nanorods," *Nano Lett.* 13, 4164-4168 (2013).
- [20] C. Saeidi and D. van der Weide, "Bandwidth-tunable optical spatial filters with nanoparticle arrays," *Opt. Express* 22, 12499-12504 (2014).
- [21] T. Xu, Y. K. Wu, X. G. Luo, and L. J. Guo, "Plasmonic nanoresonators for high-resolution colour filtering and spectral imaging," *Nat. Commun.* 1, 59(2010).
- [22] A. F. Kaplan, T. Xu, and L. J. Guo, "High efficiency resonance-based spectrum filters with tunable transmission bandwidth fabricated using nanoimprint lithography," *Appl. Phys. Lett.* 99(14), 143111(2011).
- [23] F. Cheng, J. Gao, T. S. Luk, and X. D. Yang, "Structural color printing based on plasmonic metasurfaces of perfect light absorption," *Sci. Rep.* 5, 11045(2015).
- [24] F. Cheng, J. Gao, L. Stan, D. Rosenmann, D. Czaplewski, and X. D. Yang, "Aluminum plasmonic metamaterials for structural color printing," *Opt. Express* 23, 14552-14560 (2015).
- [25] F. Cheng, X. D. Yang, D. Rosenmann, L. Stan, D. Czaplewski, and J. Gao, "Enhanced structural color generation in aluminum metamaterials coated with a thin polymer layer," *Opt. Express* 23, 25329-25339 (2015).
- [26] K. Kumar, H. G. Duan, R. S. Hegde, S. C. W. Koh, J. N. Wei, and J. K. W. Yang, "Printing colour at the optical diffraction limit," *Nat. Nanotechnol.* 7, 557-561 (2012).
- [27] X. M. Goh, Y. H. Zheng, S. J. Tan, L. Zhang, K. Kumar, C. W. Qiu, and J. K. W. Yang, "Three-dimensional plasmonic stereoscopic prints in full colour," *Nat. Commun.* 5, 5361(2014).

- [28] Y. C. Liang, W. Wang, J. S. Moon, and J. G. Winiarz, "Enhancement in the photorefractive performance of organic composites photosensitized with functionalized CdSe quantum dots," *Opt. Mater.* 58, 203-209 (2016).
- [29] N. Fang, H. Lee, C. Sun, and X. Zhang, "Sub-diffraction-limited optical imaging with a silver superlens," *Science* 308, 534-537 (2005).
- [30] L. Sun, X. D. Yang, W. Wang, and J. Gao, "Diffraction-free optical beam propagation with near-zero phase variation in extremely anisotropic metamaterials," *J. Opt.* 17(2015).
- [31] N. Liu, T. Weiss, M. Mesch, L. Langguth, U. Eigenthaler, M. Hirscher, C. Sonnichsen, and H. Giessen, "Planar Metamaterial Analogue of Electromagnetically Induced Transparency for Plasmonic Sensing," *Nano Lett.* 10, 1103-1107 (2010).
- [32] R. Adato, A. A. Yanik, J. J. Amsden, D. L. Kaplan, F. G. Omenetto, M. K. Hong, S. Erramilli, and H. Altug, "Ultra-sensitive vibrational spectroscopy of protein monolayers with plasmonic nanoantenna arrays," *Proc. Natl. Acad. Sci. U.S.A.* 106, 19227-19232 (2009).
- [33] H. Wei, Z. X. Wang, X. R. Tian, M. Kall, and H. X. Xu, "Cascaded logic gates in nanophotonic plasmon networks," *Nat. Commun.* 2, 387(2011).
- [34] Y. K. R. Wu, A. E. Hollowell, C. Zhang, and L. J. Guo, "Angle-Insensitive Structural Colours based on Metallic Nanocavities and Coloured Pixels beyond the Diffraction Limit," *Sci. Rep.* 3, 1194(2013).
- [35] T. Xu, H. F. Shi, Y. K. Wu, A. F. Kaplan, J. G. Ok, and L. J. Guo, "Structural Colors: From Plasmonic to Carbon Nanostructures," *Small* 7, 3128-3136 (2011).
- [36] M. A. Kats, R. Blanchard, P. Genevet, and F. Capasso, "Nanometre optical coatings based on strong interference effects in highly absorbing media," *Nat. Mater.* 12, 20-24 (2013).
- [37] K. Chung, S. Yu, C. J. Heo, J. W. Shim, S. M. Yang, M. G. Han, H. S. Lee, Y. Jin, S. Y. Lee, N. Park, and J. H. Shin, "Flexible, Angle-Independent, Structural Color Reflectors Inspired by Morpho Butterfly Wings," *Adv. Mater.* 24, 2375-2379 (2012).
- [38] T. W. Ebbesen, H. J. Lezec, H. F. Ghaemi, T. Thio, and P. A. Wolff, "Extraordinary optical transmission through sub-wavelength hole arrays," *Nature* 391, 667-669 (1998).
- [39] H. S. Lee, Y. T. Yoon, S. S. Lee, S. H. Kim, and K. D. Lee, "Color filter based on a subwavelength patterned metal grating," *Opt. Express* 15, 15457-15463 (2007).

- [40] H. Park, Y. Dan, K. Seo, Y. J. Yu, P. K. Duane, M. Wober, and K. B. Crozier, "Filter-Free Image Sensor Pixels Comprising Silicon Nanowires with Selective Color Absorption," *Nano Lett.* 14, 1804-1809 (2014).
- [41] K. Seo, M. Wober, P. Steinvurzel, E. Schonbrun, Y. P. Dan, T. Ellenbogen, and K. B. Crozier, "Multicolored Vertical Silicon Nanowires," *Nano Lett.* 11, 1851-1856 (2011).
- [42] C. L. Haynes, A. D. McFarland, L. L. Zhao, R. P. Van Duyne, G. C. Schatz, L. Gunnarsson, J. Prikulis, B. Kasemo, and M. Kall, "Nanoparticle optics: The importance of radiative dipole coupling in two-dimensional nanoparticle arrays," *J. Phys. Chem. B* 107, 7337-7342 (2003).
- [43] J. A. Schuller, E. S. Barnard, W. S. Cai, Y. C. Jun, J. S. White, and M. L. Brongersma, "Plasmonics for extreme light concentration and manipulation," *Nat. Mater.* 9, 193-204 (2010).
- [44] H. A. Atwater and A. Polman, "Plasmonics for improved photovoltaic devices," *Nat. Mater.* 9, 205-213 (2010).
- [45] H. X. Deng, T. C. Wang, J. Gao, and X. D. Yang, "Metamaterial thermal emitters based on nanowire cavities for high-efficiency thermophotovoltaics," *J. Opt.* 16(3), 035102(2014).
- [46] G. V. Naik, V. M. Shalaev, and A. Boltasseva, "Alternative Plasmonic Materials: Beyond Gold and Silver," *Adv. Mater.* 25, 3264-3294 (2013).
- [47] J. F. Zhang, J. Y. Ou, N. Papasimakis, Y. F. Chen, K. F. MacDonald, and N. I. Zheludev, "Continuous metal plasmonic frequency selective surfaces," *Opt. Express* 19, 23279-23285 (2011).
- [48] V. R. Shrestha, S. S. Lee, E. S. Kim, and D. Y. Choi, "Aluminum Plasmonics Based Highly Transmissive Polarization-Independent Subtractive Color Filters Exploiting a Nanopatch Array," *Nano Lett.* 14, 6672-6678 (2014).
- [49] V. Kulkarni, E. Prodan, and P. Nordlander, "Quantum Plasmonics: Optical Properties of a Nanomatryushka," *Nano Lett.* 13, 5873-5879 (2013).
- [50] T. Sondergaard, S. M. Novikov, T. Holmgaard, R. L. Eriksen, J. Beermann, Z. H. Han, K. Pedersen, and S. I. Bozhevolnyi, "Plasmonic black gold by adiabatic nanofocusing and absorption of light in ultra-sharp convex grooves," *Nat. Commun.* 3, 969(2012).
- [51] http://www.inplainviewwinnipeg.com/prairie_stained_glass.shtml,
<https://www.prairiestudioglass.com/>

II. ALL-METAL STRUCTURAL COLOR PRINTING BASED ON ALUMINUM PLASMONIC METASURFACES

Zhigang Li,^{1,3} Wei Wang,^{1,3} Daniel Rosenmann,² David A. Czaplewski,² Xiaodong Yang,¹ And Jie Gao¹

¹Department of Mechanical and Aerospace Engineering, Missouri University of Science and Technology, Rolla, MO 65409

²Center for Nanoscale Materials, Argonne National Laboratory, Argonne, IL 60439, USA

³These authors contributed equally to this work

ABSTRACT

An all-metal structural color printing platform based on aluminum plasmonic metasurfaces is proposed and demonstrated with high color performance using only one-step etching process on aluminum surface. A wide visible color range is realized with the designed metallic square-shaped disk arrays by simply adjusting geometrical parameters of the disk etching depth, disk width and unit cell period. The demonstrated all-metal microscale structural color printing on aluminum surface offers great potential for many practical color related applications.

Keywords: Subwavelength structures; Surface plasmons; Metamaterials; Color.

1. INTRODUCTION

Over the past decade, different kinds of structural color filtering and printing techniques have been used to reproduce vivid colors in nature with great advantages over

conventional colorant-based pigmentation [1–3]. In particular, plasmonic metamaterials and metasurfaces are receiving more attention for the next generation structural color applications due to their capability of controlling the light intensity, phase and polarization effectively [4–8]. Plasmonic nanostructures with various geometries have been developed for structural color generation with high resolution including one dimensional gratings [9–11], hole arrays [12–16], nanoantenna arrays [17–21], metal-insulator-metal (MIM) structures [10, 22–27], and combined nanodisk and nanohole arrays [28–30]. By tuning the geometries and dimensions of the plasmonic nanostructures, optical resonances in the visible frequency range can be achieved based on the mechanisms of propagating surface plasmons (SP) [12–16], localized surface plasmon resonances (LSPR) [18, 28–33], as well as Fabry-Pérot cavity modes [34]. Plasmonic color generation has been widely studied in realizing highly saturated color with narrow bandwidth [23, 25–27], color filtering with extraordinary optical transmission [35–37], high-resolution color pixels for imaging [10, 28, 34], polarization dependent [16, 17] or independent [18, 20, 21] color filtering and imaging, and angle-insensitive structural color printing [21, 34]. Noble metals like gold and silver have been traditionally employed in the color filtering and imaging platforms due to their lower ohmic losses within the visible spectrum [10,18,24,25,28,34,38]. However, the interband transition of gold limits the color range obtainable to below the wavelength of 550 nm [24,39], while silver is susceptible to oxidation and sulphidation which leads to the degradation of colors under ambient usage [18]. Consequently, a suitable substitute for noble metals, aluminum, has been highly attractive for structural color printing application due to its excellent optical response in the visible spectrum, chemical and thermal stability thanks to its natively formed oxidation layer, low cost, and

complementary metal oxide semiconductor (CMOS) compatibility [15, 16, 20, 26, 27, 40]. Recently, aluminum based metamaterials with complex nanostructures such as MIM structures [10, 22–27] and combined nanodisk and nanohole arrays [28–30] have been designed to exhibit excellent color performance, however, the fabrication processes are still sophisticated, which will not only increase the production cost but degrade the color performance due to fabrication imperfections.

In this work, we introduce and demonstrate an all-metal structural color printing platform based on aluminum plasmonic metasurfaces with high color performance using a simple, onestep focused ion beam milling process on aluminum surface. By adjusting the geometrical parameters of the designed aluminum square-shaped disk arrays, including the disk etching depth, disk width and unit cell period, a wide visible color range can be realized. The mechanism of structural color generation in aluminum square-shaped disk arrays is analyzed according to the excitation of electric dipole and magnetic dipole resonances. Furthermore, the polarization and incident angle dependent optical properties of the color printing platform have also been studied. The demonstrated all-metal structural color printing on aluminum surface offers great potential for many relevant applications such as microscale imaging, information storage, and security marking.

2. DEVICE DESIGN AND FABRICATION

The square-shaped disk array on aluminum surface designed for plasmonic structural color printing is schematically illustrated in Fig. 1(a). In order to vary the optical response of the designed disk arrays in the visible spectrum, the geometrical parameters of the disk etching depth (d), disk width (w) and the unit cell period (P) are tuned. First, a 250

nm thick aluminum layer is deposited on a silicon wafer by sputtering method at a deposition rate of $12 \text{ \AA} / \text{sec}$. Then the designed disk arrays are directly milled on the aluminum layer using the focused ion beam (FIB) milling process (FEI Helios Nanolab 600 DualBeam) with a gallium ion current of 9.7 pA and an accelerating voltage of 30 KeV . In order to investigate the effects from geometrical parameters, three groups of disk arrays are fabricated with varying d , w and P , respectively. It is noted that the unit cell period can be well represented during the ion beam milling process, while the etching depth and disk width experience slight deviations from the designed values but still in a reasonable range with $\pm 15 \text{ nm}$ variation. After the ion beam milling process, it is shown from Figs. 1(b)-1(d) that the top width of square disk will be smaller than the bottom width and thus there is a tapered angle around 83° for the disk sidewall. Optical transmission of the designed structure will be effectively blocked due to the limited penetration depth in the thick aluminum layer for incident light in the visible range.

3. RESULTS OF EXPERIMENTAL CHARACTERIZATION AND NUMERICAL SIMULATION

The optical reflection spectra from the fabricated square-shaped disk arrays are characterized within the visible range ($400 \sim 800 \text{ nm}$) by utilizing an optical spectrometer (LR1, ASEQ instruments). Optical reflection spectrum and the corresponding optical reflection microscope image are collected in the bright field from each fabricated disk array with an area of $20 \times 20 \text{ \mu m}^2$. Figs. 1(b)-1(d) show SEM images of three representative disk arrays with different geometrical parameters. The insets display the measured bright-field

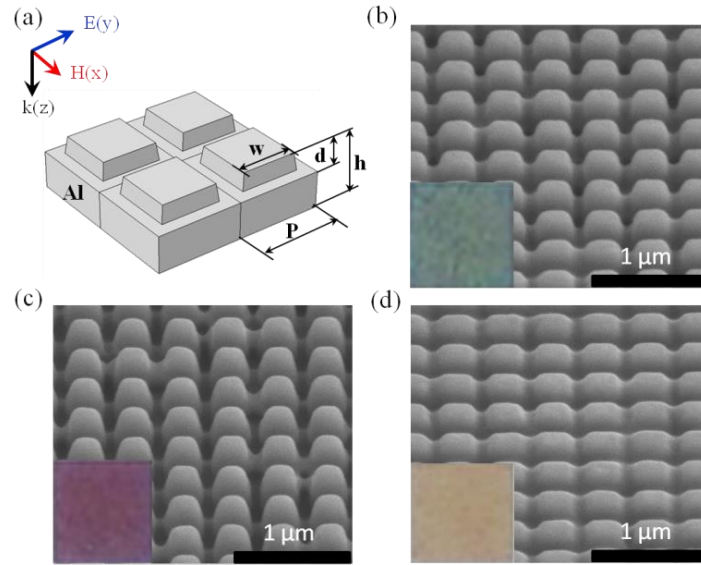


Figure 1. (a) Schematic of square-shaped disk array on aluminum surface. (b-d) SEM images of square-shaped disk arrays fabricated on $h = 250$ nm thick aluminum film with different geometric parameters of (b) $P = 400$ nm, $d = 135$ nm, $w = 245$ nm, (c) $P = 400$ nm, $d = 227$ nm, $w = 200$ nm, and (d) $P = 400$ nm, $d = 82$ nm, $w = 245$ nm. Insets: Optical reflection microscope images of $20 \times 20 \mu\text{m}^2$ disk arrays. Scale bars: $1 \mu\text{m}$.

optical microscope images of these disk arrays, showing three prime colors belonging to the Cyan-Magenta-Yellow (CMY) color model.

The effects of varying disk etching depth d , disk width w and unit cell period P for the square-shaped disk arrays on the optical reflection spectra and visible colors are further investigated. The measured optical reflection spectra and bright-field microscope images for three groups of disk arrays with varying d , w and P are shown in Fig. 2. In Fig. 2(a), the measured and simulated reflection spectra for disk arrays with varying d exhibit a red-shifted plasmonic resonance and a broader resonance dip as d is increased from 82 nm to 135 nm while $w = 245$ nm and $P = 400$ nm are constant. The colors of microscope images also change accordingly. As shown in Fig. 2(b), the similar optical response is also observed for disk arrays with reduced w from 250 nm to 200 nm and constant $P = 400$ nm. It is noted that d will depend on w during the FIB process due to the variation of ion beam

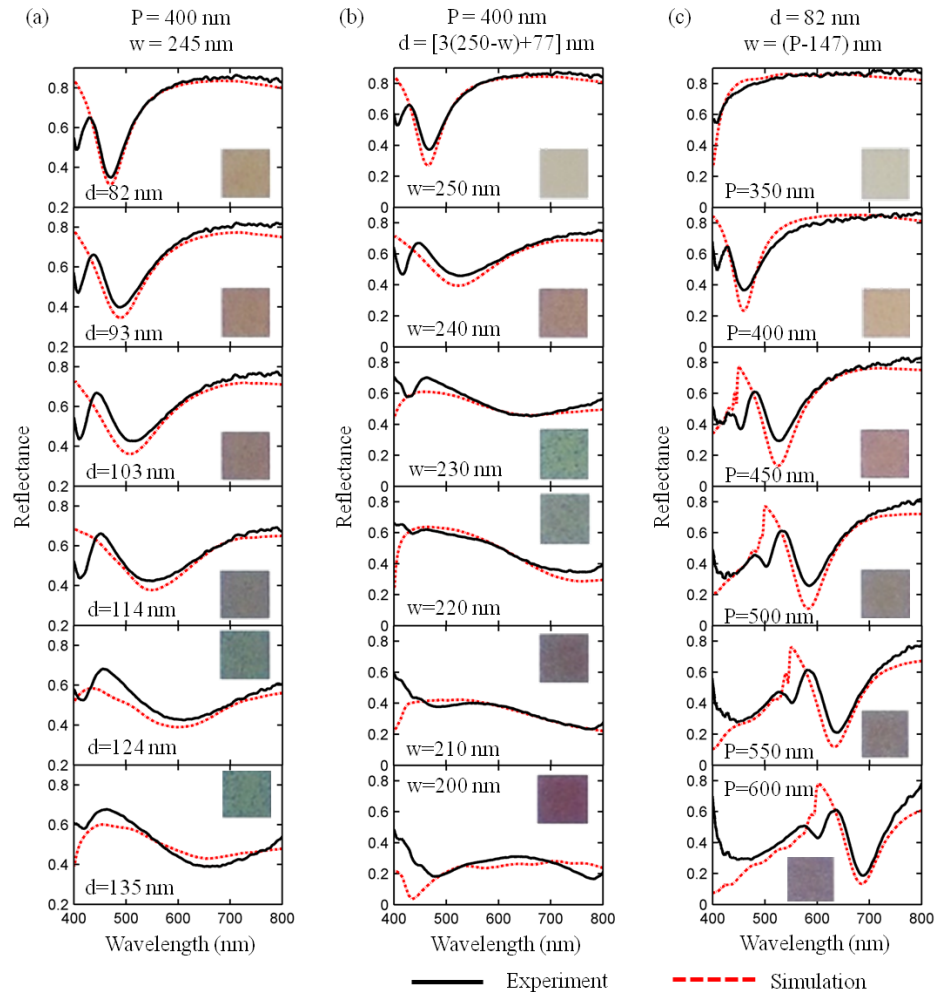


Figure 2. Measured (black solid line) and simulated (red dashed line) optical reflection spectra of three groups of disk array samples (a) by varying disk etching depth d from 82 nm to 135 nm with constant $P = 400$ nm and $w = 245$ nm, (b) by changing disk width w from 250 nm to 200 nm with constant $P = 400$ nm and d as a function of w , and (c) by changing period P from 350 nm to 600 nm with constant $d = 82$ nm and $P - w = 147$ nm. Insets show the optical reflection microscope images of $20 \times 20 \mu\text{m}^2$ disk arrays. Normal light incidence is employed.

exposure area, giving a rough expression of $d = [3(250-w)+77]$ nm. Especially for $w = 200$ nm case, a broad absorption band is obtained due to both the aluminum loss in visible and the excitation of gap plasmon modes. It is indicated that the obtained visible color range is dependent on both disk etching depth d and disk width w with a constant unit cell period P . Moreover, a wider range of color can be realized with simultaneous variation of both d

and w . In addition, Fig. 2(c) displays the results for disk arrays with varying P from 350 nm to 600 nm and $w = (P - 147)$ nm at a constant $d = 82$ nm. As both P and w are increased, the plasmonic resonance gets red-shifted. Numerical simulation results from the Finite Element Method (COMSOL Multiphysics) are also shown in Fig. 2. The geometrical parameters of square-shaped disk arrays used in simulation are measured from the SEM images. A good match between the experimental and simulation results can be found in Fig. 2. In order to understand the relationship between optical reflection spectra and color generation, all the experimental and simulated reflection spectra depicted in Figs. 2(a)-2(c) have been converted as the discrete points in the CIE 1931 xy chromaticity coordinates based on color theory in Figs. 3(a)-3(c), respectively. As the geometrical parameters of d , w and P for disk arrays vary, the chromaticity coordinates evolve clockwise close to the achromatic point, demonstrating the capability of aluminum metasurfaces for a relative large degree of visible color range tuning.

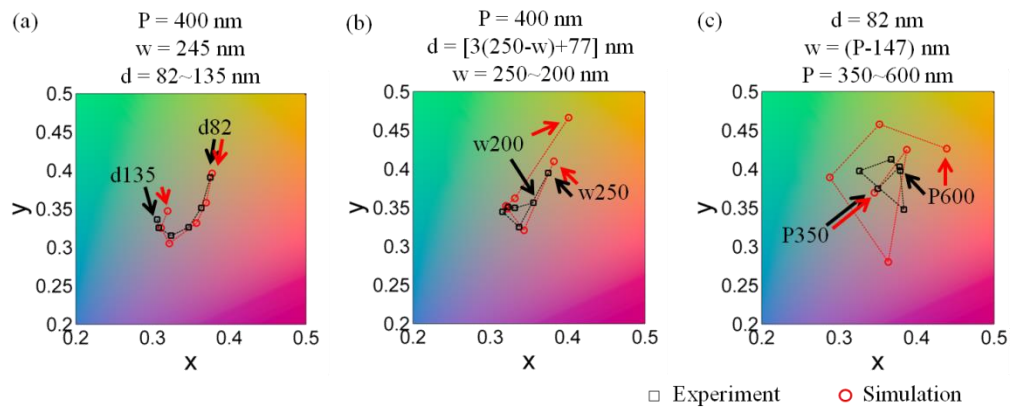


Figure 3. Measured (black square) and simulated (red circle) results in the CIE 1931 xy chromaticity coordinates for three groups of disk array samples by changing (a) d , (b) w , and (c) P . The reflection spectrum data are obtained from Figs 2(a)-2(c). The beginning and ending points of parameter variations are labeled for each case.

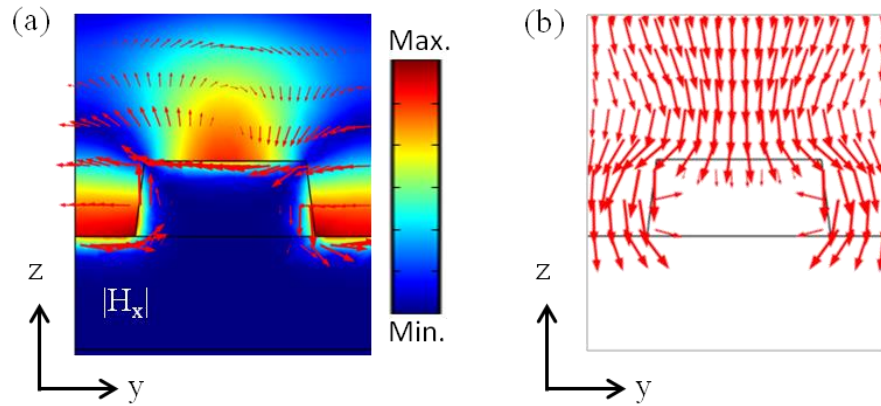


Figure 4. (a) Cross section of the time-averaged magnetic field (color map) and electric displacement (red arrows) distributions for a selected disk array (with $P = 400$ nm, $w = 245$ nm and $d = 114$ nm) at the resonance wavelength. (b) Cross section of the time-averaged optical power flow vector distribution.

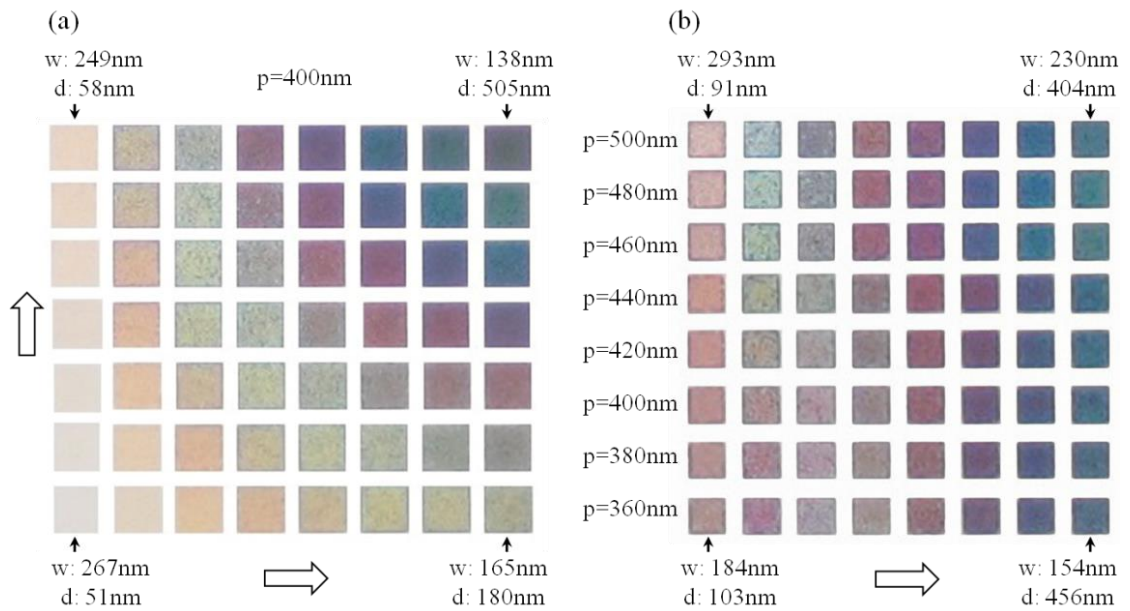


Figure 5. Color palettes generated from square-shaped disk arrays with varying disk etching depth d , disk width w and unit cell period P . (a) Color palette with constant $P = 400$ nm but varying w from 267 nm to 138 nm and d from 51 nm to 505 nm. Each fabricated disk array has an area of $15 \times 15 \mu\text{m}^2$. (b) Color palette with a certain P in each row changing from 360 nm to 500 nm and varying w from 293 nm to 154 nm and d from 91 nm to 456 nm. Each fabricated disk array has an area of $10 \times 10 \mu\text{m}^2$. The dimensions are measured from the SEM images.

In order to understand the mechanism of the plasmonic resonance for the square-shaped disk array, optical field distributions at the resonance wavelength of 546 nm is analyzed for one selected sample with $P = 400$ nm, $w = 245$ nm and $d = 114$ nm. As shown in Fig. 4(a), the time-averaged magnetic field (color map) and electric displacement (red arrows) distributions in the y - z cross section of the designed disk array indicate a strong magnetic dipole resonance with enhanced magnetic field concentrated within the air trench surrounded by three aluminum-air interfaces due to the anti-symmetric current flow. At the same time, an electric dipole resonance is also formed on the top aluminum-air interface of the disk. The time-averaged optical power flow distribution in Fig. 4(b) depicts the penetration of light into the aluminum surface layer. The excitation of resonant plasmonic modes will lead to the strong optical absorption for incident light at certain wavelength so that the subtractive color can be observed in the reflection from the disk array sample.

The designed square-shaped disk arrays on aluminum surface can exhibit various visible colors. In Fig. 5, the bright-field microscope images of two color palettes are displayed, where subtractive structural colors are generated from disk arrays with varying geometrical parameters in disk etching depth d , disk width w and unit cell period P . The color palette in Fig. 5(a) includes the disk arrays with constant $P = 400$ nm but varying w and d , where the dimensions are measured from the SEM images. While the color palette in Fig. 5(b) has the disk arrays with a certain P in each row changing from 360 nm to 500 nm and varying w and d . The etching depth beyond the total thickness of aluminum layer is also obtained in experiment, forming an aluminum-silicon two-layer post array on the silicon substrate. The absorption of incident light is further enhanced by the plasmonic resonance from the two-layer post as well as the optical loss in silicon substrate. As a result,

dark colors can be realized at the upper-right corner of the color palette in Fig. 5(a) and the right columns of the color palette in Fig. 5(b). The wide range of colors achieved with the designed aluminum metasurfaces can be used for structural color printing applications. A micrometer scale plasmonic printed copy [Fig. 6(b)] of a landscape painting we drawn [Fig. 6(a)] is fabricated according to the color palettes in Fig. 5, where the original image features and colors are successfully reproduced. The SEM images of the fabricated plasmonic painting are shown in Figs. 6(c)-6(e).

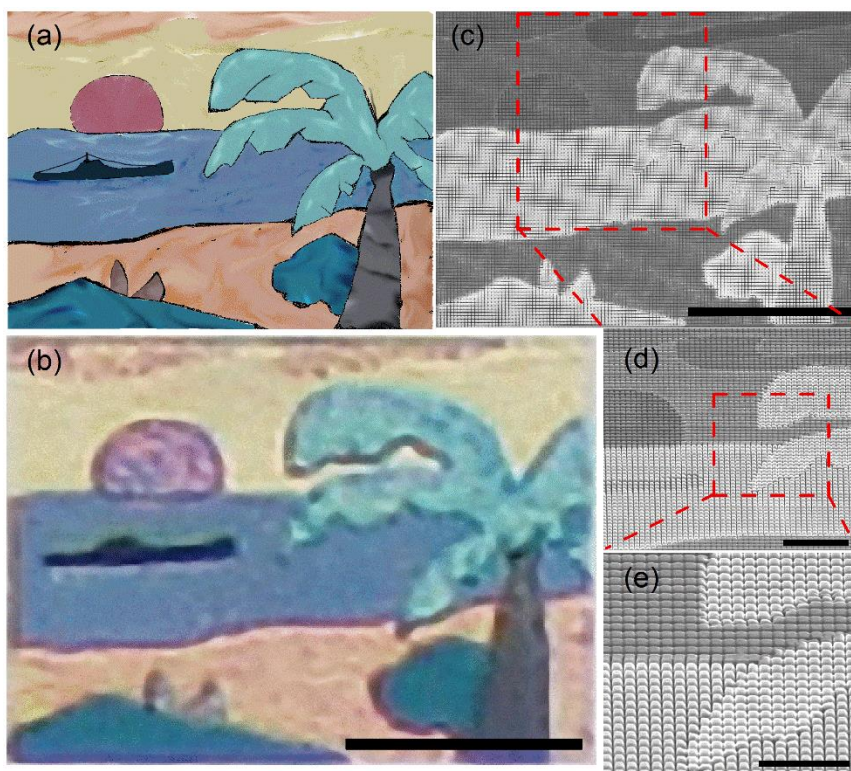


Figure 6. (a) Original landscape painting with different colors. (b) The measured bright-field optical microscope image of the plasmonic painting with size of $50\ \mu\text{m}$ by $35\ \mu\text{m}$. (c) SEM image of the fabricated plasmonic painting with various disk array patterns. (d) SEM image of the area outlined in panel (c). (e) SEM image of the area outlined in panel (d). Both SEM images in panels (d) and (e) are tilted with an angle of 52° to show clear three-dimensional disk array structures. Scale bars: $20\ \mu\text{m}$ in (b) and (c), $5\ \mu\text{m}$ in (d), and $3\ \mu\text{m}$ in (e).

4. INCIDENT ANGLE DEPENDENCE OF OPTICAL RESPONSE

By considering the realistic situation for structural color printing applications, incident angle dependence and polarization dependence of the optical spectral response are investigated in simulation for one designed square-shaped disk array with $P = 400$ nm, $w = 245$ nm and $d = 114$ nm. The calculated TE (electric field parallel to y axis) and TM (magnetic field parallel to y axis) polarized optical reflection spectra with varying incident angle from 0° to 80° are plotted in Figs. 7(a) and 7(b), respectively. For TE polarization, the plasmonic resonance gets a broader linewidth towards the longer wavelength range as the incident angle is increased. While for TM polarization, the bandwidth of strong optical absorption almost linearly extends into the longer wavelength as the incident angle is increased. Such incident angle dependence indicates that the excitation of plasmonic modes are relying on the grating coupling. Based on color theory, the TE and TM polarized reflection spectra are converted into the chromaticity coordinates as a function of the incident angle, as shown in Fig. 7(c).

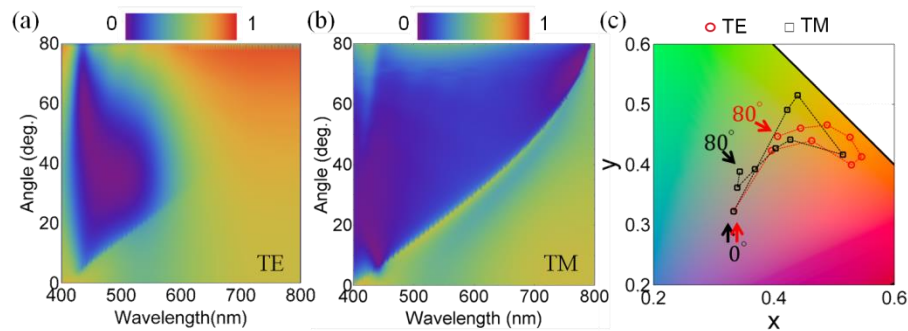


Figure 7. Simulated incident angle dependent (a) TE and (b) TM polarized optical reflection spectra for a selected disk array (with $P = 400$ nm, $w = 245$ nm and $d = 114$ nm). (c) Incident angle resolved chromaticity coordinates calculated from the reflection spectra for TE (red circle) and TM (black square) polarizations.

5. CONCLUSION

In summary, we have demonstrated an all-metal structural color printing platform based on aluminum plasmonic metasurfaces with high resolution and high color performance using a simple one-step focused ion beam milling process on aluminum surface. A wide range of visible colors has been achieved with the plasmonic metasurfaces by varying the geometrical parameters of square-shaped disk arrays including the disk etching depth, disk width and unit cell period. The subtractive colors are obtained from the reflection spectra due to the excitation of plasmonic electric and magnetic dipole resonances. The reproduced microscale landscape painting shows the feasibility and flexibility of all-metal plasmonic metasurfaces used for color printing applications. The demonstrated aluminum plasmonic metasurfaces for structural color printing will be well suited for applications such as microscale imaging, information storage, anti-counterfeit tag and security marking.

ACKNOWLEDGMENTS

The authors acknowledge the facility support from the Materials Research Center at Missouri S&T. This work was performed, in part, at the Center for Nanoscale Materials, a U.S. Department of Energy, Office of Science, Office of Basic Energy Sciences User Facility under Contract No. DE-AC02-06CH11357.

REFERENCES

- [1] K. Nassau, "The physics and chemistry of color: The 15 mechanisms," in *The Science of Color*, 2nd ed. (2003), pp. 247–280.

- [2] H. Park, Y. Dan, K. Seo, Y. J. Yu, P. K. Duane, M. Wober, and K. B. Crozier, "Filter-free image sensor pixels comprising silicon nanowires with selective color absorption," *Nano Lett.* 14(4), 1804–1809 (2014).
- [3] K. Seo, M. Wober, P. Steinvurzel, E. Schonbrun, Y. Dan, T. Ellenbogen, and K. B. Crozier, "Multicolored vertical silicon nanowires," *Nano Lett.* 11(4), 1851–1856 (2011).
- [4] L. Huang, X. Chen, H. Mühlenbernd, H. Zhang, S. Chen, B. Bai, Q. Tan, G. Jin, K.-W. Cheah, C.-W. Qiu, J. Li, T. Zentgraf, and S. Zhang, "Three-dimensional optical holography using a plasmonic metasurface," *Nat. Commun.* 4, 2808 (2013).
- [5] A. Poddubny, I. Iorsh, P. Belov, and Y. Kivshar, "Hyperbolic metamaterials," *Nat. Photonics* 7(12), 948–957 (2013).
- [6] N. Meinzer, W. L. Barnes, and I. R. Hooper, "Plasmonic meta-atoms and metasurfaces," *Nat. Photonics* 8(12), 889–898 (2014).
- [7] N. Yu and F. Capasso, "Flat optics with designer metasurfaces," *Nat. Mater.* 13(2), 139–150 (2014).
- [8] J. A. Schuller, E. S. Barnard, W. Cai, Y. C. Jun, J. S. White, and M. L. Brongersma, "Plasmonics for extreme light concentration and manipulation," *Nat. Mater.* 9(3), 193–204 (2010).
- [9] H. J. Park, T. Xu, J. Y. Lee, A. Ledbetter, and L. J. Guo, "Photonic color filters integrated with organic solar cells for energy harvesting," *ACS Nano* 5(9), 7055–7060 (2011).
- [10] B. Zeng, Y. Gao, and F. J. Bartoli, "Ultrathin nanostructured metals for highly transmissive plasmonic subtractive color filters," *Sci. Rep.* 3, 2840 (2013).
- [11] M. J. Uddin, T. Khaleque, and R. Magnusson, "Guided-mode resonant polarization-controlled tunable color filters," *Opt. Express* 22(10), 12307–12315 (2014).
- [12] C. Genet and T. W. Ebbesen, "Light in tiny holes," *Nature* 445(7123), 39–46 (2007).
- [13] Q. Chen and D. R. S. Cumming, "High transmission and low color cross-talk plasmonic color filters using triangular-lattice hole arrays in aluminum films," *Opt. Express* 18(13), 14056–14062 (2010).
- [14] D. Inoue, A. Miura, T. Nomura, H. Fujikawa, K. Sato, N. Ikeda, D. Tsuya, Y. Sugimoto, and Y. Koide, "Polarization independent visible color filter comprising an aluminum film with surface-plasmon enhanced transmission through a subwavelength array of holes," *Appl. Phys. Lett.* 98(9), 093113 (2011).

- [15] S. Yokogawa, S. P. Burgos, and H. A. Atwater, “Plasmonic color filters for CMOS image sensor applications,” *Nano Lett.* 12(8), 4349–4354 (2012).
- [16] Z. Li, A. W. Clark, and J. M. Cooper, “Dual color plasmonic pixels create a polarization controlled nano color palette,” *ACS Nano* 10(1), 492–498 (2016).
- [17] T. Ellenbogen, K. Seo, and K. B. Crozier, “Chromatic plasmonic polarizers for active visible color filtering and polarimetry,” *Nano Lett.* 12(2), 1026–1031 (2012).
- [18] G. Si, Y. Zhao, J. Lv, M. Lu, F. Wang, H. Liu, N. Xiang, T. J. Huang, A. J. Danner, J. Teng, and Y. J. Liu, “Reflective plasmonic color filters based on lithographically patterned silver nanorod arrays,” *Nanoscale* 5(14), 6243–6248 (2013).
- [19] J. Do, M. Fedoruk, F. Jäckel, and J. Feldmann, “Two-color laser printing of individual gold nanorods,” *Nano Lett.* 13(9), 4164–4168 (2013).
- [20] J. S. Clausen, E. Højlund-Nielsen, A. B. Christiansen, S. Yazdi, M. Grajower, H. Taha, U. Levy, A. Kristensen, and N. A. Mortensen, “Plasmonic metasurfaces for coloration of plastic consumer products,” *Nano Lett.* 14(8), 4499–4504 (2014).
- [21] C. Saeidi and D. van der Weide, “Bandwidth-tunable optical spatial filters with nanoparticle arrays,” *Opt. Express* 22(10), 12499–12504 (2014).
- [22] T. Xu, Y.-K. Wu, X. Luo, and L. J. Guo, “Plasmonic nanoresonators for high-resolution colour filtering and spectral imaging,” *Nat. Commun.* 1(5), 59 (2010).
- [23] A. F. Kaplan, T. Xu, and L. Jay Guo, “High efficiency resonance-based spectrum filters with tunable transmission bandwidth fabricated using nanoimprint lithography,” *Appl. Phys. Lett.* 99(14), 143111 (2011).
- [24] A. S. Roberts, A. Pors, O. Albrechtsen, and S. I. Bozhevolnyi, “Subwavelength plasmonic color printing protected for ambient use,” *Nano Lett.* 14(2), 783–787 (2014).
- [25] F. Cheng, J. Gao, T. S. Luk, and X. Yang, “Structural color printing based on plasmonic metasurfaces of perfect light absorption,” *Sci. Rep.* 5, 11045 (2015).
- [26] F. Cheng, J. Gao, L. Stan, D. Rosenmann, D. Czaplewski, and X. Yang, “Aluminum plasmonic metamaterials for structural color printing,” *Opt. Express* 23(11), 14552–14560 (2015).
- [27] F. Cheng, X. Yang, D. Rosenmann, L. Stan, D. Czaplewski, and J. Gao, “Enhanced structural color generation in aluminum metamaterials coated with a thin polymer layer,” *Opt. Express* 23(19), 25329–25339 (2015).

- [28] K. Kumar, H. Duan, R. S. Hegde, S. C. W. Koh, J. N. Wei, and J. K. W. Yang, "Printing colour at the optical diffraction limit," *Nat. Nanotechnol.* 7(9), 557–561 (2012).
- [29] X. M. Goh, Y. Zheng, S. J. Tan, L. Zhang, K. Kumar, C.-W. Qiu, and J. K. W. Yang, "Three-dimensional plasmonic stereoscopic prints in full colour," *Nat. Commun.* 5, 5361 (2014).
- [30] S. J. Tan, L. Zhang, D. Zhu, X. M. Goh, Y. M. Wang, K. Kumar, C. W. Qiu, and J. K. W. Yang, "Plasmonic color palettes for photorealistic printing with aluminum nanostructures," *Nano Lett.* 14(7), 4023–4029 (2014).
- [31] C. L. Haynes, A. D. McFarland, L. L. Zhao, R. P. Van Duyne, G. C. Schatz, L. Gunnarsson, J. Prikulis, B. Kasemo, and M. Käll, "Nanoparticle optics: The importance of radiative dipole coupling in two-dimensional nanoparticle arrays," *J. Phys. Chem. B* 107(30), 7337–7342 (2003).
- [32] S. Zou and G. C. Schatz, "Theoretical studies of plasmon resonances in one-dimensional nanoparticle chains: narrow lineshapes with tunable widths," *Nanotechnology* 17(11), 2813–2820 (2006).
- [33] V. A. Markel and A. K. Sarychev, "Propagation of surface plasmons in ordered and disordered chains of metal nanospheres," *Phys. Rev. B* 75(8), 085426 (2007).
- [34] Y.-K. R. Wu, A. E. Hollowell, C. Zhang, and L. J. Guo, "Angle-insensitive structural colours based on metallic nanocavities and coloured pixels beyond the diffraction limit," *Sci. Rep.* 3, 1194 (2013).
- [35] T. W. Ebbesen, H. J. Lezec, H. F. Ghaemi, T. Thio, P. A. Wolff, T. Thio, and P. A. Wolff, "Extraordinary optical transmission through sub-wavelength hole arrays," *Nature* 391, 1114–1117 (1998).
- [36] L. Martín-Moreno, F. J. García-Vidal, H. J. Lezec, K. M. Pellerin, T. Thio, J. B. Pendry, and T. W. Ebbesen, "Theory of extraordinary optical transmission through subwavelength hole arrays," *Phys. Rev. Lett.* 86(6), 1114–1117 (2001).
- [37] H. Liu and P. Lalanne, "Microscopic theory of the extraordinary optical transmission," *Nature* 452(7188), 728–731 (2008).
- [38] R. J. H. Ng, X. M. Goh, and J. K. W. Yang, "All-metal nanostructured substrates as subtractive color reflectors with near-perfect absorptance," *Opt. Express* 23(25), 32597–32605 (2015).
- [39] J. Zhang, J.-Y. Ou, N. Papasimakis, Y. Chen, K. F. Macdonald, and N. I. Zheludev, "Continuous metal plasmonic frequency selective surfaces," *Opt. Express* 19(23), 23279–23285 (2011).

- [40] V. R. Shrestha, S. S. Lee, E. S. Kim, and D. Y. Choi, "Aluminum plasmonics based highly transmissive polarization-independent subtractive color filters exploiting a nanopatch array," *Nano Lett.* 14(11), 6672–6678 (2014).
- [41] L. Wang, R. J. H. Ng, S. S. Dinachali, M. Jalali, Y. Yu, and J. K. W. Yang, "Large area plasmonic color palettes with expanded gamut using colloidal self-assembly," *ACS Photonics* 3(4), 627–633 (2016).
- [42] T. Søndergaard, S. M. Novikov, T. Holmgaard, R. L. Eriksen, J. Beermann, Z. Han, K. Pedersen, and S. I. Bozhevolnyi, "Plasmonic black gold by adiabatic nanofocusing and absorption of light in ultra-sharp convex grooves," *Nat. Commun.* 3, 969 (2012).
- [43] T. Søndergaard and S. I. Bozhevolnyi, "Theoretical analysis of plasmonic black gold: Periodic arrays of ultrasharp grooves," *New J. Phys.* 15, 013034 (2013).
- [44] S. Westland, C. Ripamonti, and V. Cheung, "Computing CIE tristimulus values," in *Computational Colour Science Using MATLAB®* (John Wiley and Sons, Ltd., 2012), pp. 27–47.
- [45] V. A. Fedotov, P. L. Mladyonov, S. L. Prosvirnin, and N. I. Zheludev, "Planar electromagnetic metamaterial with a fish scale structure," *Phys. Rev. E Stat. Nonlin. Soft Matter Phys.* 72(5), 056613 (2005).
- [46] W. Cai, U. K. Chettiar, H.-K. Yuan, V. C. de Silva, A. V. Kildishev, V. P. Drachev, and V. M. Shalaev, "Metamagnetics with rainbow colors," *Opt. Express* 15(6), 3333–3341 (2007).
- [47] Z. Fang, Y.-R. Zhen, L. Fan, X. Zhu, and P. Nordlander, "Tunable wide-angle plasmonic perfect absorber at visible frequencies," *Phys. Rev. B* 85(24), 1–7 (2012).
- [48] T. Xu, H. Shi, Y. K. Wu, A. F. Kaplan, J. G. Ok, and L. J. Guo, "Structural colors: From plasmonic to carbon nanostructures," *Small* 7(22), 3128–3136 (2011).

III. ENHANCED QUANTUM DOT SPONTANEOUS EMISSION WITH MULTILAYER METAMATERIAL NANOSTRUCTURES

Ling Li,¹ Wei Wang,¹ Ting S. Luk,² Xiaodong Yang,¹ and Jie Gao²

¹Department of Mechanical and Aerospace Engineering, Missouri University of Science and Technology, Rolla, MO 65409

²Center for Integrated Nanotechnologies, Sandia National Laboratories, Albuquerque, New Mexico 87185, United States

ABSTRACT

The Purcell effect of quantum dot (QD) spontaneous emission with Ag-SiO₂ multilayer metamaterial nanostructures has been demonstrated in experiment and simulation. A broadband enhanced spontaneous emission rate of QDs is observed due to large local density of states in the epsilon-near-zero and hyperbolic regions of multilayer structures. Multilayer gratings are utilized to further enhance the QD spontaneous emission as the QDs located inside the grating grooves strongly interact with high-k coupled surface plasmon polariton modes. Photoluminescence decay measurements are in good agreement with both analytical treatment with a nonlocal effect and three-dimensional finite-element simulation. Detailed studies of QD position and polarization effects on emission rate enhancement for multilayer and multilayer grating nanostructures provide important insight for understanding the coupling mechanisms of emitter-multilayer interaction and the engineering of local density of states in metamaterial nanostructures. These results will advance many applications in light-emitting devices, nanoscale lasers, quantum electrodynamics, and quantum information processing.

Keywords: metamaterials, quantum dots, Purcell effect, spontaneous emission enhancement, light-matter interaction

1. INTRODUCTION

Multilayer metamaterials consisting of alternating sub-wavelength layers of a metal and a dielectric have been studied extensively in recent years. The periodic spatial layout of metal and dielectric layers makes multilayer metamaterials artificial uniaxial anisotropic materials with unique optical properties compared with their counterparts in nature. Electromagnetic waves propagating through them undergo a transition from closed elliptical to open hyperbolic dispersions when one or two principle components of the permittivity tensor pass through zero at specific wavelengths. At these wavelengths, the appearance of ultralong wavelengths accompanying epsilon-near-zero (ENZ) behaviors of electromagnetic waves manifests as extreme slow phase modulation, which is highly desirable in wavefront shaping and directional emission [1-6]. In the hyperbolic region of the multilayer metamaterials, optical modes with anomalously large wave vectors enabled by coupled surface plasmon polaritons (SPPs) on metal-dielectric interfaces provide tremendous capabilities of near-field subwavelength imaging and large local density of states (LDOS) for spontaneous emission rate enhancement [3, 5, 7-17]. The wide tunability of the anisotropic optical property by changing the metal filling ratio and layer thickness leads to broad applications for multilayer metamaterials [3, 5, 18].

Spontaneous emission enhancement is very important for advances in single-photon sources, light-emitting devices, low threshold photonics, and plasmonic lasers. Among many systems, microcavities and photonic crystals have been extensively studied

for spontaneous emission rate enhancement by the cavity Purcell effect [19, 20]. They provide a high resonant quality factor, tight electromagnetic field confinement, and thus large spontaneous emission rate enhancement. However, the resonant requirement limits the spectral bandwidth for the cavity Purcell effect, hindering the broadband emission operation. This resonance requirement also exists in a parallel line of studies on spontaneous emission rate enhancement using plasmonic nanostructures such as nanoparticles and nanoantenna [21-23]. The coupling strength between an emitter and the plasmonic resonant mode is enhanced due to the subwavelength mode volumes of plasmonic nanostructures. Compared to all these resonant structures with narrow spectral widths and spatially localized electromagnetic modes, planar multilayer metamaterial nanostructures are capable of providing broadband Purcell effects on spontaneous emission. In the hyperbolic dispersion regime, these multilayer metamaterials possess ideally divergent LDOS, leading to very large Purcell factors in the broadband [9, 6, 17].

Various hyperbolic multilayer metamaterials have been used to enhance spontaneous emission of fluorescent emitters such as dye molecules and QDs [10, 11, 15, 17, 24]. Subwavelength gratings were also fabricated in multilayer structures to further couple spontaneous emission to high wave vector modes inside those hyperbolic multilayer metamaterials [15, 17, 24, 25]. In these studies, an effective medium theory (EMT) approximation is normally employed to predict the ENZ wavelength and calculate the Purcell factor, guiding the design of multilayer metamaterials for tunable spontaneous emission enhancement. However, without the consideration of nonlocal effects of multilayers, it is not able to fully predict or explain the measurements on the ENZ response and Purcell factor of multilayer structures [26-29].

In this work, Ag-SiO₂ multilayer metamaterial and multilayer grating nanostructures are utilized to realize a 3- to 6-fold enhanced spontaneous emission rate of CdSe/ZnS QDs in a broad wavelength range from 570 to 680 nm. For a multilayer structure, a large LDOS in the ENZ and hyperbolic regions results in a higher Purcell factor and QD emission rate enhancement compared to the elliptical region. Multilayer gratings facilitate the positioning of QDs inside grating grooves and strengthen the QDs' interaction with high-k coupled SPP modes so that the spontaneous emission rate is further enhanced. Time-resolved fluorescence experiments are performed to measure emission rate enhancement, which are in good agreement with theoretical analysis and numerical simulation based on actual multilayer parameters. Moreover, we investigate the spatial and polarization dependence of emission rate enhancement, as well as the electric field distributions excited by dipole emitters. It is revealed that the z-polarized dipole dominates the emission rate enhancement on a multilayer surface due to the coupling with an SPP wave, while a y-polarized dipole possesses a large emission rate enhancement inside grating grooves due to the strong excitation of high-k coupled SPP modes in the multilayer gratings (see coordinates in Fig. 1(a)). The results pave the way to the understanding of enhanced light-matter interactions between quantum emitters and metamaterial nanostructures, as well as the advancement of metamaterial-based applications in light-emitting devices, nanoscale lasers, optical sensing, quantum electrodynamics, and quantum information processing.

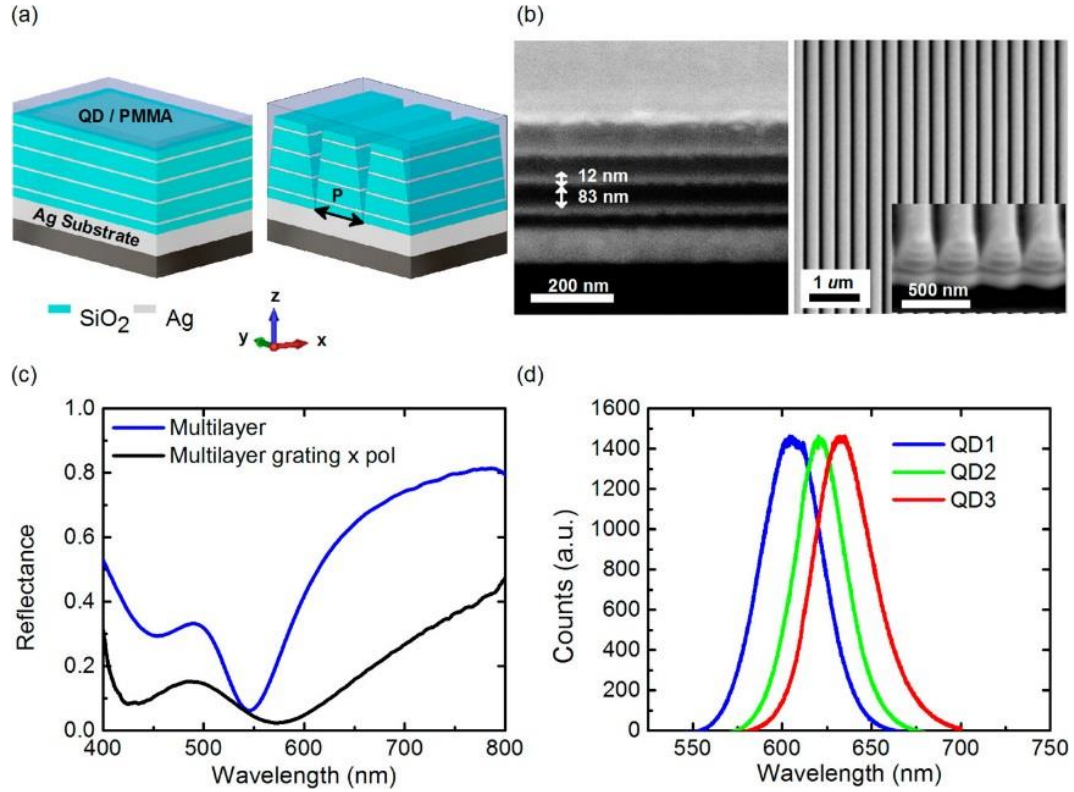


Figure 1. Multilayer metamaterial nanostructures. (a, b) Schematic and SEM for a multilayer structure and multilayer gratings. The multilayer is composed of four pairs of Ag layers (thickness $a_m = 12$ nm) and SiO₂ layers (thickness $a_d = 83$ nm), with unit cell thickness $a = a_m + a_d = 95$ nm and a total thickness of 380 nm. The multilayer is deposited on the 100 nm Ag substrate as a reflector. A multilayer grating nanostructure with a grating period $P = 300$ nm is fabricated, and the bottom angle of the grating groove trapezium is 82.5° . A thin layer of QDs in PMMA is spin-coated on the surface of the multilayer nanostructures. (c) Reflection spectra of a multilayer and multilayer gratings. (d) Emission spectra of the three sets of CdSe/ZnS QDs on a glass substrate.

2. RESULTS AND DISCUSSION

Fig. 1a shows a schematic of the Ag-SiO₂ multilayer metamaterial and multilayer grating nanostructures. The multilayer consists of four alternating pairs of Ag and SiO₂ layers, with the designed layer thickness of a_m and a_d for Ag and SiO₂, respectively. A half-layer of SiO₂ is deposited as top and bottom layers in order to achieve symmetric

multilayer structures and also to protect the Ag layer from oxidizing. The filling ratio of Ag, $f_m = a_m/a$, where $a = a_m + a_d$ is the multilayer unit cell thickness, can be chosen to achieve spontaneous emission rate enhancement within specific wavelength range. Subwavelength gratings are designed on the multilayer with a grating period $P = 300$ nm. A thin layer of QDs in poly (methyl methacrylate) (PMMA) is spin-coated on the surface of multilayer nanostructures. Scanning electron micrographs (SEM) of a multilayer and multilayer grating are shown in Fig. 1b. The left panel shows the cross-section view of the multilayer structure, where Ag and SiO₂ layers are visible as bright and dark bands, with layer thicknesses of 12 nm (a_m) and 83 nm (a_d), respectively. These layer thicknesses are obtained by fitting the multilayer reflection spectrum using the transfer-matrix method. The right panel of Fig. 1b shows a top-view SEM of periodic gratings fabricated in the multilayer structure with multilayer ridges (bright color) and air grooves (dark color). The inset shows a tilted-view SEM of a multilayer grating where individual layers are also clearly presented. The permittivity of Ag and SiO₂ layers is also characterized during the multilayer deposition process. The reflection spectra of both a multilayer and multilayer grating are shown in Fig. 1c. The multilayer ENZ wavelength retrieved using nonlocal EMT based on the transfer-matrix method is at 600 nm, vastly different from 561 nm, which is derived by local EMT. Fig. 1d shows the photoluminescence spectra of three sets of CdSe/ZnS QDs, with center emission wavelengths of 604 nm (QD1), 620 nm (QD2), and 630 nm (QD3), respectively. They provide a broadband emission wavelength range spanning from 550 to 700 nm to ensure probing the Purcell effect of QD emission in elliptical, ENZ, and hyperbolic regions of the multilayer metamaterial nanostructures.

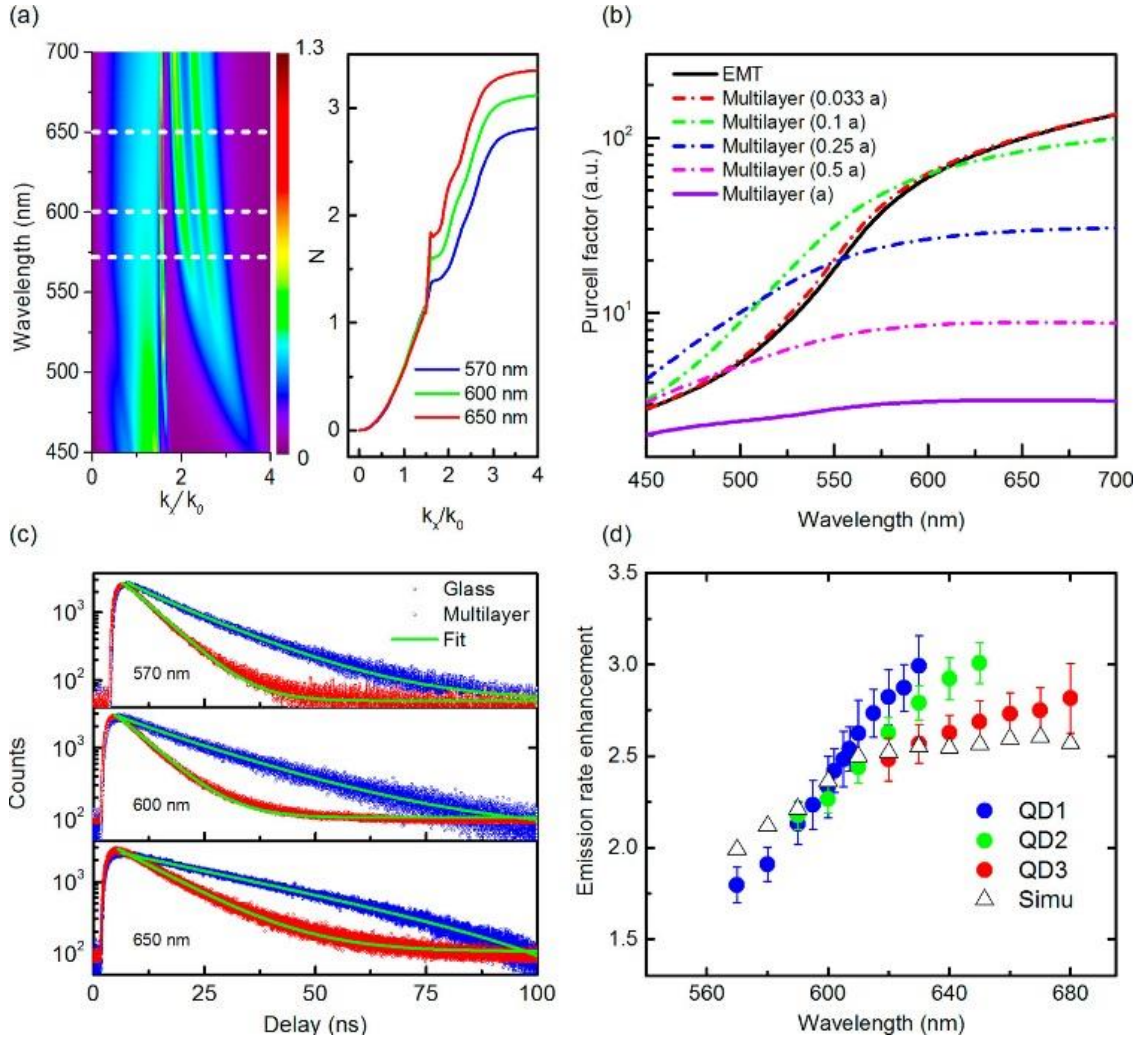


Figure 2. Spontaneous emission enhancement of QDs on a multilayer structure. (a) Left: normalized dissipated power spectrum (intensity on a logarithmic scale) for dipole emission at a distance of 10 nm above the multilayer surface; right: cumulative LDOS of dipole emission at wavelengths of 570 nm (elliptical), 600 nm (ENZ), and 650 nm (hyperbolic), as denoted by the three white dashed lines in the left panel. (b) Theoretical Purcell factor calculations for multilayer metamaterials with varying unit cell thickness and EMT approximation. (c) Photoluminescence decay measurements for QD emission on glass (blue circle) and the multilayer (red circle) at wavelengths of 570, 600, and 650 nm. The green lines are a theoretical fitting using a modified exponential model. (d) QD emission rate enhancement shown in dots by normalizing the QD photoluminescence decay lifetime obtained from the measurements on the glass substrate with that on the multilayer sample and 3D simulation results of the emission rate enhancement shown as hollow triangles.

In order to understand the LDOS and Purcell effect of the multilayer metamaterial, we first investigate the Purcell factor of the multilayer theoretically based on the multilayer parameters in the fabricated sample. Fig. 2a shows the normalized dissipated power spectrum and the accumulated LDOS enhancement of an electric dipole 10 nm above the multilayer surface. The theoretical normalized dissipated power spectrum in the left panel is obtained by averaging two orthogonal polarizations to estimate the random dipole orientation in the experiment, i.e., $\frac{1}{3} \frac{dP_{\perp}}{dk_x} + \frac{2}{3} \frac{dP_{\parallel}}{dk_x}$. To show that the LDOS of the multilayer structure evolving from elliptical to hyperbolic dispersion regions cross the ENZ wavelength, the right panel of Fig. 2a compares the cumulative LDOS, $N(u) = \int_0^u \left(\frac{1}{3} \frac{dP_{\perp}}{dk_x} + \frac{2}{3} \frac{dP_{\parallel}}{dk_x} \right)$, at emission wavelengths of 570, 600, and 650 nm, as correspondingly marked as three white dashed lines in the left panel, where $u = k_x/k_0$ is the normalized wave vector component parallel to multilayer surface. It is shown that the dipole emitter couples almost equally to the low-k propagation modes at the three wavelengths, but interacts with the high-k coupled SPP modes existing at the multilayer interfaces with much stronger coupling strengths in the ENZ and hyperbolic regions (600 and 650 nm), resulting in higher dissipated power and larger LDOS compared to the elliptical region (570 nm). Fig. 2b shows the theoretical prediction of the Purcell factor for QD emission on the surface of a multilayer structure with $a = 95$ nm (purple solid curve), which gives an average Purcell factor of 2.5. The influence of the multilayer unit cell thickness on the Purcell factor is examined with decreasing the unit cell thickness but fixing the Ag filling ratio, as shown by the dashed curves in Fig. 2b. It demonstrates that smaller unit cell thickness leads to a larger Purcell factor due to stronger couplings between SPPs on metal-dielectric interfaces

and higher cutoff wave vectors in the integration of LDOS. When the multilayer unit cell thickness is decreased to infinitely small, the calculated Purcell factor approaches the result based on EMT (black solid curve). It is worth noting that the EMT approximation overestimates the Purcell factor of QD emission on an actual multilayer structure because EMT ignores the finite layer thickness and includes infinitely large wave vector modes contributing to the Purcell factor 1 order of magnitude higher.

To demonstrate the Purcell effect of a metamaterial multilayer, time-resolved photoluminescence decay measurements of QDs on a multilayer and glass (control) are conducted. Fig. 2c presents the photoluminescence decay data from QDs on the multilayer at emission wavelengths of 570, 600, and 650 nm, which show faster decay than that on the glass substrate. It is also observed that the QD spontaneous emission lifetime at wavelengths of 600 and 650 nm is shorter compared to that at 570 nm, indicating a stronger Purcell effect in the ENZ and hyperbolic regions. QD concentration and laser excitation power are carefully controlled in these experiments at an extremely low level to make sure the observed photoluminescence decays are very close to single-exponential decays. All the decay curves at different emission wavelengths are fitted using a modified exponential relaxation model [30-33]. The fitted decay times for these curves of QDs on the multilayer (glass) in Fig. 2c are 7.91 (14.44) ns at 570 nm, 8.27 (19.35) ns at 600 nm, and 12.79 (34.10) ns at 650 nm. Fig. 2d illustrates the emission rate enhancement of the multilayer structure as a function of wavelength, which is obtained by normalizing the QDs' photoluminescence decay lifetime on the glass substrate with that on the multilayer sample. The error bar at each wavelength reflects the variation of the measured lifetime at more than 10 different spots on the sample surfaces. It is shown that the emission rate

enhancement from all three sets of QDs covering a broad wavelength range increases from the elliptical to the hyperbolic dispersion region of the multilayer structure. There is some discrepancy of the measured emission rate enhancement between different sets of QDs especially at the longer wavelengths, due to different number densities, optical and chemical environment, and size distribution of QDs originating from the synthesis process. The emission rate enhancement is also modeled with three-dimensional (3D) finite-element simulation using the geometric and material properties as detailed in Fig. 1. The simulation takes into account the dipole position, polarization, and quantum efficiency effects on emission rate enhancement as a function of wavelength [11, 17, 34, 35]. The simulation results (hollow triangles in Fig. 2(d) are averaged from 10 vertical dipole positions and three orthogonal polarizations for each emission, which show excellent agreement with the measurements.

To further enhance the interaction between QDs and multilayer metamaterials, a subwavelength grating nanostructure is introduced into the multilayer to provide larger spatial overlap and enable stronger coupling between QDs inside the grating grooves and the high- k SPP mode of the multilayer structure [17, 24]. Representative photoluminescence decays of QDs at two emission wavelengths measured on a multilayer and multilayer grating are shown in Fig. 3a. We observe that data from both nanostructures can be fitted by the modified exponential decay model very well, and QDs on multilayer gratings have shorter decay times compared to QDs on a multilayer. The fitted decay times for these curves of QDs on a multilayer grating (multilayer) in Fig. 3a are 6.11 (9.97) ns for 620 nm and 6.53 (12.79) ns for 650 nm. Subsequently, emission rate enhancement of a multilayer and a multilayer grating structure at all wavelengths covered by QDs emission

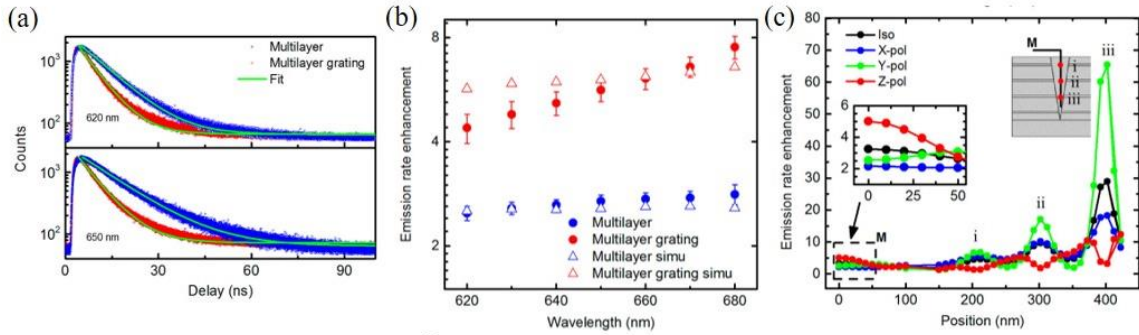


Figure 3. Spontaneous emission enhancement of QDs on multilayer gratings. (a) Photoluminescence decay measurements for QD emission wavelengths at 620 and 650 nm on a multilayer (blue circle) and a multilayer grating (red circle). (b) Emission rate enhancement obtained by normalizing the measured QDs' photoluminescence decay lifetime on a glass substrate with that on multilayer nanostructures shown by dots, together with the 3D simulation results averaging from different dipole positions and polarizations on the nanostructures. (c) Simulation of emission rate enhancement for x-, y-, and z-polarized dipole emission at 620 nm at various locations and the average of three polarizations, labelled as Iso. The x-axis represents the distance starting from the grating ridge centre (M point) to all the positions along the black line toward the grating groove bottom (shown in the inset schematic).

is obtained by normalizing the QD photoluminescence decay lifetime on a glass substrate with that on a multilayer and a multilayer grating, denoted by solid dots in Fig. 3b, together with the well-matching 3D finite-element simulation results (solid lines). The spatial and polarization dependence of the emission rate enhancement are also investigated by simulation of dipole emission at different locations on a multilayer grating as depicted in Fig. 3c. The position axis measures distances from the QD site 10 nm above the center of a grating ridge surface toward the grating groove surface and then down to the grating groove bottom, as illustrated by the black line in the schematic inset of Fig. 3c. The red dots on that curve denote three QD locations (i, ii, iii) inside the grating groove at the position of silver layers, and correspondingly three peaks in emission rate enhancement are

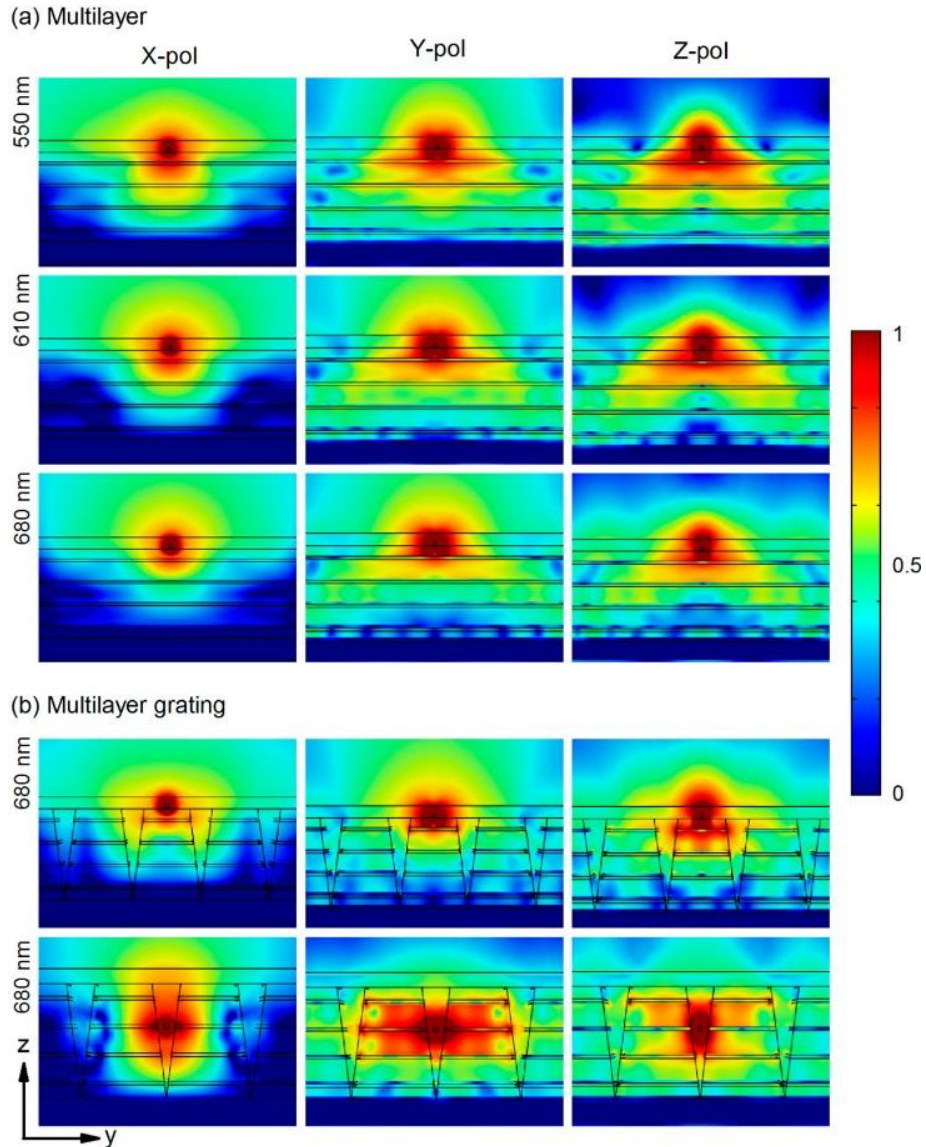


Figure 4. Simulated electric field magnitude distribution of QDs with emission wavelengths of 550, 610, and 680 nm on top of a multilayer (a) and at 680 nm on and inside a multilayer grating (b). Three columns of electric field distributions are from dipole emission with x polarization (X-pol), y polarization (Y-pol), and z polarization (Z-pol), respectively.

observed with strong Purcell effects at these locations. Moreover, emission rate enhancement shows different dipole polarization dependence when the emitter is located on the top of the grating surface and at the bottom of the grating groove. When a QD emitter is located at the grating ridge center, the contribution from z-polarization dominates the

averaged emission rate enhancement over x- and y-polarization because the SPP wave in the multilayer structure can be excited well by the z-polarized dipole. When the emitter resides in positions (i, ii, iii) inside the groove, emission rate enhancement for the y-polarized dipole shows a large Purcell effect due to the strong excitation of the high-k coupled SPP modes in the multilayer gratings. Additionally, as the groove width shrinks, the coupling gets even stronger, leading to the significantly increased emission rate enhancement at position (iii).

To show more clearly the influence of an emitter's positions and polarizations on the Purcell effect of multilayer metamaterial nanostructures, electric field distributions of a dipole emitter 10 nm above the multilayer surface and inside the multilayer grating groove are illustrated in Fig. 4. Fig. 4a shows electric field magnitude distributions inside a multilayer at three emission wavelengths, 550, 610, and 680 nm, to demonstrate the increasing LDOS for a dipole emitter on top of a multilayer surface from the elliptical to the hyperbolic dispersion region. The third column of Fig. 4a shows that the z-polarized dipole strongly couples to the multilayer and contributes mostly to the Purcell factor. As emission wavelength moves from the elliptical to the ENZ and hyperbolic regions, the electric fields from dipole emission penetrate deeper into the multilayer. Fig. 4b presents the electric field magnitude distribution from an emitter with an emission wavelength at 680 nm on top of and inside the groove of a multilayer grating structure. The electric field intensity distributions of x-, y-, and z-polarized dipole emission in Fig. 4b correspond to the emission rate enhancement results shown in Fig. 3c. It is noteworthy that inside the grating groove y polarized dipole emission efficiently excites the high-k coupled SPP modes across all the metal-dielectric interfaces in the grating nanostructures (as shown in

the middle plot of the bottom row in Fig. 4b), indicating the enhanced dipole- multilayer coupling with the y-polarized dipole which provides the major contribution to the high emission rate enhancement inside the grating groove.

3. CONCLUSIONS

We have demonstrated multilayer metamaterial and multilayer grating nanostructures with broadband Purcell effects for CdSe/ZnS QD emission. Several-fold emission rate enhancement is achieved with a large LDOS as the emission wavelength goes from the elliptical to the hyperbolic dispersion regime across the ENZ region of a multilayer metamaterial. Multilayer gratings further enhance the QDs' spontaneous emission as the QDs located inside the grating grooves strongly interact with high-k coupled SPP modes. Position and polarization effects on QD emission rate enhancement are studied to reveal the coupling mechanisms and further engineer the LDOS in metamaterial nanostructures. Our results provide insight into the understanding of QD-metamaterial interactions, especially the broadband Purcell effect, LDOS manipulations with different dispersions, and coupling to the high-k coupled SPP modes, which have the potential for the development of promising applications in light-matter interactions such as light-emitting devices [36, 37], nanoscale lasers [38, 39], quantum electrodynamics, and quantum information processing [40, 41].

4. METHODS

An electron beam evaporation system is used to deposit the multilayer stack on silicon substrates at the rate of 0.2 \AA/s for both Ag and SiO₂ layers. The designed thickness

for the Ag and SiO₂ layer is 10 and 85 nm, respectively. Characterization of the optical constant of each material is performed with a variable-angle spectroscopic ellipsometer (VASE, J. A. Woollam Co. VB400/ HS-190). To obtain Ag and SiO₂ layer thickness as denoted in Fig. 1, we measure the reflection spectrum of the multilayer under normal incidence and fit it using the transfer-matrix method. The grating on a multilayer is fabricated using focused ion beam milling (FEI Helios Nanolab 600 DualBeam) with a gallium ion current of 9.7 pA and an accelerating voltage of 30 keV. To prepare samples for time-resolved photoluminescence measurements, the original CdSe/ZnS QD solution (QD weight ratio 3%, solvent: chloroform) is diluted with a mixed solution of PMMA (weight ratio 2%, solvent: anisole), anisole, and chloroform, resulting in a final volume ratio of PMMA:anisole:chloroform = 1:3:4 and final weight ratios for QDs and PMMA of 0.05% and 0.2%, respectively. Then the diluted QDs-PMMA solution was spin-coated on surfaces of the multilayer, multilayer grating, and glass samples. The spin lasted for 1 min with a spin speed of 1200 rpm, resulting in one very thin PMMA matrix layer with an estimated thickness of 50 nm.

QDs are treated as ideal electric dipoles with internal quantum efficiency η . The quantum efficiency for QDs is interpolated as a function of wavelength using experimental values [35]. The Purcell factors experienced by a dipole emitter placed at a distance of d above the planar multilayer with polarization perpendicular (\perp) or parallel (\parallel) to the multilayer interface are [34]

$$F_{\perp} = 1 - \eta + \eta Re \int_0^{\infty} \frac{dP_{\perp}}{du} du \quad (1)$$

$$F_{\parallel} = 1 - \eta + \eta Re \int_0^{\infty} \frac{dP_{\parallel}}{du} du \quad (2)$$

The two integrands are the normalized dissipated power spectra for the perpendicular and parallel polarizations of the dipole emitter with respect to that of a dipole in a vacuum[34]. In the weak coupling regime, the semiclassical theory is equivalent to the quantum mechanical approach, and the LDOS enhancement and the normalized dipole dissipated power density are equivalent [12, 26, 34, 42]. The corresponding LDOS enhancement is[34]

$$\frac{dP_{\perp}}{du} = \frac{3k_0}{2k_z} \left(\frac{u}{\sqrt{\varepsilon_1}} \right)^3 [1 + r_p e^{2ik_z d}] \quad (3)$$

$$\frac{dP_{\parallel}}{du} = \frac{3k_0}{2k_z \sqrt{\varepsilon_1}} \left\{ 1 + r_s e^{2ik_{\perp} d} + \frac{k_z^2}{\varepsilon_1 k_0^2} [1 - r_p e^{2ik_z d}] \right\} \quad (4)$$

where k_0 is the magnitude of the wave vector in a vacuum, $u = k_x / k_0$ is the wavevector component parallel to the multilayer surface normalized by the vacuum wavevector, $k_z = k_0 \sqrt{\varepsilon_1 - u^2}$ is the component of the wavevector perpendicular to the multilayer interface, ε_1 is the relative permittivity for the host material, PMMA, and $r_{p,s}$ is the reflection coefficient at the interfaces for a p- or s-polarized wave, respectively. In our theoretical calculation, the relative permittivity for PMMA (ε_1) is obtained from a reference, and those for Ag and SiO₂ are from our own characterization data obtained during the fabrication process (see Supporting Information). All FEM simulations are carried out in COMSOL Multiphysics. A point electric dipole is used to simulate the Purcell factor for a dipole emitter on multilayer nanostructures. Results of the electric dipole with polarization parallel (PF_∥) and perpendicular (PF_⊥) to the multilayer surface are used to get the average Purcell factor: $PF_{iso} = (1/3)PF_{\parallel} + (2/3)PF_{\perp}$, where $PF_i = 1 - \eta + \eta (P_{i,rad} + P_{i,nonrad}) / P_0$ ($i = \parallel, \perp$). In the simulation, P_0 , $P_{i,rad}$, and $P_{i,nonrad}$ are

evaluated as the total dipole emission power into the homogeneous dielectric environment (PMMA), total dipole radiative power into the far field, and the dissipated power in the multilayer nanostructures, respectively [11, 17, 34, 43]. To compare with emission rate enhancement obtained from photoluminescence decay measurements, dipole emitters at different heights away from the top surface of the multilayers and at different locations inside the multilayer grating grooves are considered in the simulations.

QDs' spontaneous emission lifetime is measured by using a time-correlated single photon counting system (PicoQuant Photonics). A picosecond-pulsed excitation source is operated at an emission wavelength of 402 nm, minimum pulse width of 52 ps, repetition rate of 10 MHz, and mean excitation power of 0.25 μ W measured at the entrance to an objective lens (NA 0.5). This objective lens was used to couple both excitation to and emission from the QDs. A single photon counting module was synchronized with the pulsed excitation source to obtain the time-resolved photoluminescence intensity of the QD emission, by detecting the emission signals from an optical fiber mounted on the side exit slit of a spectrometer (Horiba IHR550). The QDs' emission spectra are obtained from a liquid N₂ cooled CCD detector.

The spontaneous emission lifetime of the QDs on the multilayer sample and glass substrate are obtained by fitting the experimental photoluminescence decay data using a modified exponential relaxation model [30-33]:

$$I(t) = I_0 e^{-(t/\tau)^\beta} + I_b \quad (5)$$

where τ is the decay lifetime after which the photoluminescence intensity $I(t)$ exponentially drops to $1/e$ of its initial value I_0 . The modification parameter β describes the deviation of a realistic multiexponential photoluminescence decay measured in

experiments from an ideal single-exponential decay model that recovers when $\beta = 1$. The stretched exponential relaxation model is a common choice to fit multicomponent exponential decays such as QD emission presented in this study [30]. Photoluminescence decay data within the full delay time limit (100 ns) are used in the curve fitting with eq. 5. The fitted β values for the photoluminescence decay curves of QDs on a multilayer (glass) in Fig. 2c are 1.10 (0.94) at 570 nm, 1.09 (0.94) at 600 nm, and 1.02 (0.97) at 650 nm. The fitted β values for QD decay curves on a multilayer grating (multilayer) in Fig. 3a are 1.00 (1.07) at 620 nm and 0.98 (1.02) at 650 nm. The coefficients of determination (R -squared) for all these curve fittings are very close to 1 (ranging from 0.975 to 0.997), indicating the model (eq 5) fits all data very well. Berbera Santos et al. [30] have proved that the ensemble average emission rate constant can be described as β/τ . Because all our fitted β values are very close to 1, the emission rate enhancement is obtained from the normalized fitted decay lifetime in the current study to demonstrate enhancement effects of the multilayer nanostructures for all possible QD emission channels.

ACKNOWLEDGMENTS

The authors acknowledge the support from the National Science Foundation under grants ECCS-1653032, CBET- 1402743, and DMR-1552871. This work was performed, in part, at the Center for Integrated Nanotechnologies, an Office of Science User Facility operated for the U.S. Department of Energy (DOE) Office of Science. Sandia National Laboratories is a multiprogram laboratory managed and operated by the Sandia Corporation, a wholly owned subsidiary of the Lockheed Martin Corporation, for the U.S.

Department of Energy's National Nuclear Security Administration under contract DE-AC04-94AL85000.appreciated.

REFERENCES

- [1] Subramania, G., A. Fischer, and T. Luk, Optical properties of metal-dielectric based epsilon near zero metamaterials. *Applied Physics Letters*, 2012. 101(24): p. 241107.
- [2] Shekhar, P., J. Atkinson, and Z. Jacob, Hyperbolic metamaterials: fundamentals and applications. *Nano Convergence*, 2014. 1(1): p. 14.
- [3] Yang, X., et al., Experimental demonstration of near-infrared epsilon-near-zero multilayer metamaterial slabs. *Optics express*, 2013. 21(20): p. 23631-23639.
- [4] Poddubny, A., et al., Hyperbolic metamaterials. *Nature Photonics*, 2013. 7(12): p. 948-957.
- [5] Maas, R., et al., Experimental realization of an epsilon-near-zero metamaterial at visible wavelengths. *Nature Photonics*, 2013. 7(11): p. 907-912.
- [6] Gao, J., et al., Experimental realization of epsilon-near-zero metamaterial slabs with metal-dielectric multilayers. *Applied Physics Letters*, 2013. 103(5): p. 051111.
- [7] Lu, D., et al., Enhancing spontaneous emission rates of molecules using nanopatterned multilayer hyperbolic metamaterials. *Nature nanotechnology*, 2014. 9(1): p. 48-53.
- [8] Shalaginov, M.Y., et al., Broadband enhancement of spontaneous emission from nitrogen-vacancy centers in nanodiamonds by hyperbolic metamaterials. *Applied Physics Letters*, 2013. 102(17): p. 173114.
- [9] Galfsky, T., et al., Active hyperbolic metamaterials: enhanced spontaneous emission and light extraction. *Optica*, 2015. 2(1): p. 62-65.
- [10] Ferrari, L., et al., Enhanced spontaneous emission inside hyperbolic metamaterials. *Optics express*, 2014. 22(4): p. 4301-4306.
- [11] Sreekanth, K., T. Biaglow, and G. Strangi, Directional spontaneous emission enhancement in hyperbolic metamaterials. *Journal of Applied Physics*, 2013. 114(13): p. 134306.
- [12] Newman, W.D., C.L. Cortes, and Z. Jacob, Enhanced and directional single-photon emission in hyperbolic metamaterials. *JOSA B*, 2013. 30(4): p. 766-775.

- [13] Krishnamoorthy, H.N., et al., Topological transitions in metamaterials. *Science*, 2012. 336(6078): p. 205-209.
- [14] Kim, J., et al., Improving the radiative decay rate for dye molecules with hyperbolic metamaterials. *Optics express*, 2012. 20(7): p. 8100-8116.
- [15] Jacob, Z., I.I. Smolyaninov, and E.E. Narimanov, Broadband Purcell effect: Radiative decay engineering with metamaterials. *Applied Physics Letters*, 2012. 100(18): p. 181105.
- [16] Iorsh, I., et al., Spontaneous emission enhancement in metal–dielectric metamaterials. *Physics Letters A*, 2012. 376(3): p. 185-187.
- [17] Wood, B., J. Pendry, and D. Tsai, Directed subwavelength imaging using a layered metal-dielectric system. *Physical Review B*, 2006. 74(11): p. 115116.
- [18] Ferrari, L., et al., Hyperbolic metamaterials and their applications. *Progress in Quantum Electronics*, 2015. 40: p. 1-40.
- [19] Choy, J.T., et al., Enhanced single-photon emission from a diamond-silver aperture. *Nature Photonics*, 2011. 5(12): p. 738-743.
- [20] Tomaš, M.-S. and Z. Lenac, Spontaneous-emission spectrum in an absorbing Fabry-Perot cavity. *Physical Review A*, 1999. 60(3): p. 2431.
- [21] Zhukovsky, S., et al., Hyperbolic metamaterials based on quantum-dot plasmon-resonator nanocomposites. *Optics express*, 2014. 22(15): p. 18290-18298.
- [22] Belacel, C., et al., Controlling spontaneous emission with plasmonic optical patch antennas. *Nano letters*, 2013. 13(4): p. 1516-1521.
- [23] Ozel, T., et al., Anisotropic emission from multilayered plasmon resonator nanocomposites of isotropic semiconductor quantum dots. *ACS nano*, 2011. 5(2): p. 1328-1334.
- [24] Sreekanth, K.V., et al., Large spontaneous emission rate enhancement in grating coupled hyperbolic metamaterials. *Scientific reports*, 2014. 4.
- [25] Sreekanth, K.V., A. De Luca, and G. Strangi, Experimental demonstration of surface and bulk plasmon polaritons in hypergratings. *Scientific reports*, 2013. 3.
- [26] Sun, L., et al., Experimental characterization of optical nonlocality in metal-dielectric multilayer metamaterials. *Optics express*, 2014. 22(19): p. 22974-22980.
- [27] Kidwai, O., S.V. Zhukovsky, and J. Sipe, Effective-medium approach to planar multilayer hyperbolic metamaterials: Strengths and limitations. *Physical Review A*, 2012. 85(5): p. 053842.

- [28] Orlov, A.A., et al., Engineered optical nonlocality in nanostructured metamaterials. *Physical Review B*, 2011. 84(4): p. 045424.
- [29] Kidwai, O., S.V. Zhukovsky, and J. Sipe, Dipole radiation near hyperbolic metamaterials: applicability of effective-medium approximation. *Optics letters*, 2011. 36(13): p. 2530-2532.
- [30] Leistikow, M., et al., Size-dependent oscillator strength and quantum efficiency of CdSe quantum dots controlled via the local density of states. *Physical Review B*, 2009. 79(4): p. 045301.
- [31] Ford, G.W. and W.H. Weber, Electromagnetic interactions of molecules with metal surfaces. *Physics Reports*, 1984. 113(4): p. 195-287.
- [32] Berberan-Santos, M.N., A luminescence decay function encompassing the stretched exponential and the compressed hyperbola. *Chemical Physics Letters*, 2008. 460(1): p. 146-150.
- [33] Lee, K.B., et al., Application of the stretched exponential function to fluorescence lifetime imaging. *Biophysical Journal*, 2001. 81(3): p. 1265-1274.
- [34] Schlegel, G., et al., Fluorescence decay time of single semiconductor nanocrystals. *Physical Review Letters*, 2002. 88(13): p. 137401.
- [35] Berberan-Santos, M., E. Bodunov, and B. Valeur, Mathematical functions for the analysis of luminescence decays with underlying distributions 1. Kohlrausch decay function (stretched exponential). *Chemical Physics*, 2005. 315(1): p. 171-182.
- [36] Le-Van, Q., et al., Electrically driven optical metamaterials. *Nature communications*, 2016. 7.
- [37] Shalaginov, M.Y., et al., Enhancement of single-photon emission from nitrogen-vacancy centers with TiN/(Al, Sc) N hyperbolic metamaterial. *Laser & Photonics Reviews*, 2015. 9(1): p. 120-127.
- [38] Meng, X., et al., Wavelength-tunable spasing in the visible. *Nano letters*, 2013. 13(9): p. 4106-4112.
- [39] Oulton, R.F., et al., Plasmon lasers at deep subwavelength scale. *Nature*, 2009. 461(7264): p. 629-632.
- [40] Jha, P.K., et al., Coherence-driven topological transition in quantum metamaterials. *Physical review letters*, 2016. 116(16): p. 165502.
- [41] Jin, X.R., et al., Quantum entanglement in plasmonic waveguides with near-zero mode indices. *Optics letters*, 2013. 38(20): p. 4078-4081.

IV. SCALING LAW OF PURCELL FACTOR IN HYPERBOLIC METAMATERIAL CAVITIES WITH DIPOLE EXCITATION

Wei Wang,¹ Xiaodong Yang,¹ Jie Gao¹

¹Department of Mechanical and Aerospace Engineering, Missouri University of Science and Technology, Rolla, MO 65409

ABSTRACT

To control the spontaneous emission rate of dipole emitters, resonant cavity is widely used to provide large electromagnetic mode confinement and thus results in the enhanced Purcell effect. Here, hyperbolic metamaterial cavities with different wavevectors are designed to have identical fundamental mode at the same resonant frequency. The anomalous power law for the Purcell factor of cavity wavevector is investigated with dipole excitation. Different from conventional photonic and plasmonic cavities, a fifth power law $PF \sim (k/k_0)^5$ for small wavevectors and a square law $PF \sim (k/k_0)^2$ for large wavevectors have been demonstrated. The unique optical properties and Purcell factor scaling law of hyperbolic metamaterial cavities will greatly benefit the applications in cavity electrodynamics, quantum optics, single photon sources, on-chip quantum computing and circuits.

Keywords: Metamaterials; Multilayers; Quantum optics; Subwavelength structures, nanostructures; Resonators.

1. INTRODUCTION

Control of spontaneous emission of emitters such as quantum dots [1-3], molecules [4], color centers [5], etc. plays an important role in the study of non-classical light emission, fluorescence detection, quantum optics and quantum information processing [6-12]. According to Purcell effect [13], spontaneous emission rates of single emitters can be modified by photonic and plasmonic cavities [14-16] which possess both high quality factors and small electromagnetic mode volumes. Recently, hyperbolic metamaterials have drawn a lot of attentions due to the large photonic density of states supported in the metamaterials [17-22]. In addition, hyperbolic metamaterial cavities in infrared frequencies have been realized to offer ultrahigh mode refractive indices and small mode volumes [23-25]. Quite different from previously studied photonic and plasmonic cavities, one unique optical property of hyperbolic metamaterial cavities is that, along the hyperbolic dispersion curve, a series of nano-cavities with different resonating wavevectors k can be designed to have the same resonant frequency. It provides us an opportunity to study the scaling law for the Purcell factor of the resonance wavevector at a fixed resonant frequency of the cavities (i.e., the emission frequency of the emitters).

2. HYPERBOLIC MULTILAYER NANO-CAVITY DESIGN

A schematic of two-dimensional (2D) hyperbolic multilayer nano-cavity is shown in Fig. 1(a), where the multilayer consists of alternative 4 nm Au and 6 nm Al₂O₃ layers (40% fill ratio of gold). The permittivity of Au is described by the Drude model $\epsilon_m = \epsilon_\infty - \omega_p^2 / (\omega^2 + i\omega\gamma)$, with permittivity constant $\epsilon_\infty = 1$, plasma frequency $\omega_p = 1.37 \times 10^{16}$ rad/s and damping factor $\gamma = 4.08 \times 10^{13}$ rad/s. The dielectric constant of Al₂O₃ is $\epsilon_d = 2.28$. The multilayer metamaterial permittivity can be described using the effective media theory (EMT) [19] with a

uniaxial dielectric tensor $\vec{\epsilon}(\vec{r}) = \text{diag}(\epsilon_{xx}, \epsilon_{yy}, \epsilon_{zz})$ [15, 31], where $\epsilon_{xx} = \epsilon_{yy} = p\epsilon_m + (1-p)\epsilon_d$, $\epsilon_{zz} = \epsilon_m\epsilon_d/[(1-p)\epsilon_m + p\epsilon_d]$, p is the fill ratio of metal, ϵ_m and ϵ_d is permittivity of metal and dielectric respectively. When the extraordinary (TM-polarized) wave propagating in strongly anisotropic metamaterial, iso-frequency contour (IFC) can be drawn according to the following equation [17]:

$$\frac{k_x^2}{\epsilon_{\perp}} + \frac{k_z^2}{\epsilon_{\parallel}} = \frac{\omega^2}{c^2} \quad (1)$$

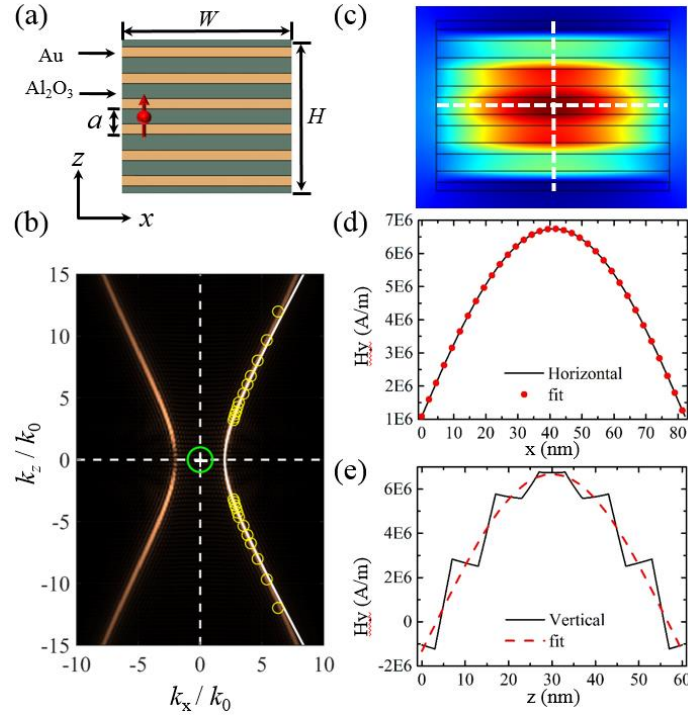


Figure 1. (a) Schematic of 2D multilayer nano-cavity made of alternate Au (4nm) and Al_2O_3 (6nm). Period of the multilayer is denoted by a , and dipole emitter is illustrated by the red dot. (b) IFC for multilayer metamaterials calculated from FFT (bronze colored lines) and EMT (white lines) at wavelength of 850 nm. The yellow circles represent the extracted resonating wavevectors of the designed cavity modes and the green circle represents the light cone of vacuum. (c) Eigen mode magnetic field distribution for cavity with size (82.2 nm \times 60 nm). (d, e) The magnetic field profiles along the horizontal and vertical middle line of eigen mode are fitted to extract the wavevectors inside each cavity.

Within the interested wavelength range of a typical quantum dot dipole emitter, for example at 850 nm, real part of the permittivity principal components of the multilayer metamaterials have opposite signs, which leads to the hyperbolic IFC as shown in Fig. 1(b) (white lines). For multilayers with finite layer thicknesses, optical nonlocality leads to the effective permittivity tensor that is not only related to the frequency but also to the wavevector [26]. The IFC considered the nonlocal effect can be obtained by spatial Fourier analysis(FFT) of the electric field excited by a dipole emitter placed inside the multilayer [27], shown as bronze colored lines in Fig. 1(b) . In the low k region ($k \ll 2\pi/a$), the IFC calculated from EMT matches with the Fourier analysis. In the high k region where the wavelength gets close to the period of the multilayers, the dispersion curve deviates from the effective medium calculation at the edge of the first Brillouin zone [23, 27]. Metamaterials with hyperbolic IFCs can support very large wavevectors and optical density of states, which will strongly enhance light-matter interaction such as spontaneous emission [17, 19]. Furthermore, nano-cavities can be designed based on hyperbolic multilayer metamaterials with extreme large refractive index and ultrasmall mode volume [27]. As illustrated in Fig. 2(a), a series of ten 2D nano-cavities consisting of 4 to 13 pairs of Au-Al₂O₃ layer (corresponding to cavity height H from 40 nm to 130 nm) are designed with identical fundamental resonances at 850 nm. The top and bottom layer is set to Al₂O₃ with half the normal dielectric layer thickness as 3nm to protect the Au layer. The cavity width W can be approximately expressed as $w \approx 2\pi/\sqrt{|\epsilon_{\perp}|(\omega^2/c^2 - \pi^2/(|\epsilon_{\parallel}|H^2))}$ according to the EMT and dispersion relation [28]. Further tunings of the cavity widths are performed in the Eigen-frequency analysis with the approximated W values as initial design parameter, and the final geometric dimensions of the nano-cavities are optimized in order to ensure that a series of nano-cavities with different sizes all support fundamental resonant mode at 850nm. For example as shown in Fig. 1(c), Eigen-frequency analysis gives the width

design of 82.2nm for cavity with height of 60nm, and the magnetic field distribution of the fundamental Eigen mode is presented. Wavevector k_x and k_z of the cavity mode can be extracted by fitting the magnetic field profiles along the middle cut lines in Fig. 1(c) with $H_y(x, z) = A_1 \cos(k_x x + \varphi_1) A_2 \cos(k_z z + \varphi_2)$, as shown in Figs. 1 (d-e). Yellow circles in Fig. 1(b) marks all the extracted wavevectors for all the designed cavities, which coincide with the multilayer hyperbolic IFC very well.

3. SCALING LAW OF PURCELL FACTOR

Purcell effect is the enhancement of a quantum emitter's spontaneous emission rate by its environment [14]. The Purcell factor (PF) defined as the ratio between the modified spontaneous emission rate γ_{SE} in nanostructures and free-space γ_0 can be obtained by [29]

$$PF = 1 - \eta + \eta(P/P_0) \quad (2)$$

in full wave electromagnetic simulation, where $P(P_0)$ is total emission power from the dipole emitter including both the radiated and dissipated power in nanostructures (free space) calculated by integrating the power flow through the boundaries and η is internal quantum efficiency (we set it to unity for our calculation) [17, 19]. In order to investigate the scaling law for Purcell factors of wavevectors, for each designed nano-cavity, an electric dipole emitter with dipole moment along z direction is placed inside the cavity and total dipole emission power is calculated with FEM simulation. The position of the dipole is chosen to be in the middle dielectric layer where the maximum of electric field locates, as illustrated in Fig. 1(a). Under dipole excitation, identical fundamental modes have been excited at 850 nm as confirmed by the electric field and magnetic field distributions of each cavity presented in Fig. 2. Taking the ratio of total emission power from the dipole inside the nano-cavity and in free space, Purcell factors as a function of the resonating

wavevectors of a 2D cavity mode are plotted in Fig. 3(a), where red circle and square represent the cases with ideal lossless metal and realistic lossy metal respectively. We can observe that a clear fifth power scaling law of $PF \sim (k/k_0)^5$ can be seen in the log-log plot (red dashed line) for lossless case. When metal loss is considered, the Purcell factor scaling law still follows the fifth power for small wavevectors however $PF \sim (k/k_0)^2$ is presented for large wavevectors shown as the black dashed line. The results reveal that for hyperbolic metamaterial nano-cavities which support very large wavevectors and high mode indices, Purcell factors grows rapidly and follow distinct scaling laws in the large and small wavevector regions.

In order to further understand the underlying physics about the scaling law and compare to the case of conventional optical cavities, quality factors and mode areas of hyperbolic metamaterial 2D nano-cavities are investigated as a function of resonating wavevectors, and Purcell factors can be evaluated by the following equation[14]:

$$PF = \frac{1}{\pi^2} \left(\frac{\lambda}{n}\right)^2 \frac{Q}{A} \left(\frac{|E|}{|E_{max}|} \cos\theta\right)^2 \quad (3)$$

where n is effective refraction index, λ is wavelength in vacuum, Q is the cavity quality factor, A is the cavity mode area, E is the electric field at the position of the emitter, and θ is the angle between the dipole moment and the local electric field. The mode area A is defined as the ratio of electromagnetic energy in the entire space over the maximum electromagnetic energy density[30, 31], $A = \left[\int \varepsilon(\vec{r}) |\vec{E}(\vec{r})|^2 d^2\vec{r} \right] / \max \left[\varepsilon(\vec{r}) |\vec{E}(\vec{r})|^2 \right]$. As shown in Fig. 2(a), most of the electromagnetic energy is confined inside the cavity due to the extremely high refractive mode index, but the cavity corners still scatter high k waves and result in radiation energy loss. Total energy in the entire space is integrated across all the simulation area ($\sim 1.5 \mu\text{m} \times 1.5 \mu\text{m}$), which is large enough compared to the cavity size and sufficient to include all the electromagnetic energy.

The maximum energy density is found at the middle dielectric layer where the electric dipole is also placed. Fig. 3(b) shows the relation between mode area and wavevector for all cavities in a log-log plot. The scaling law of $A \sim (k/k_0)^2$ (red dashed line) is shown. The relationship between mode volume and wavevector in 3D situation will follow a third power law as expected [32].

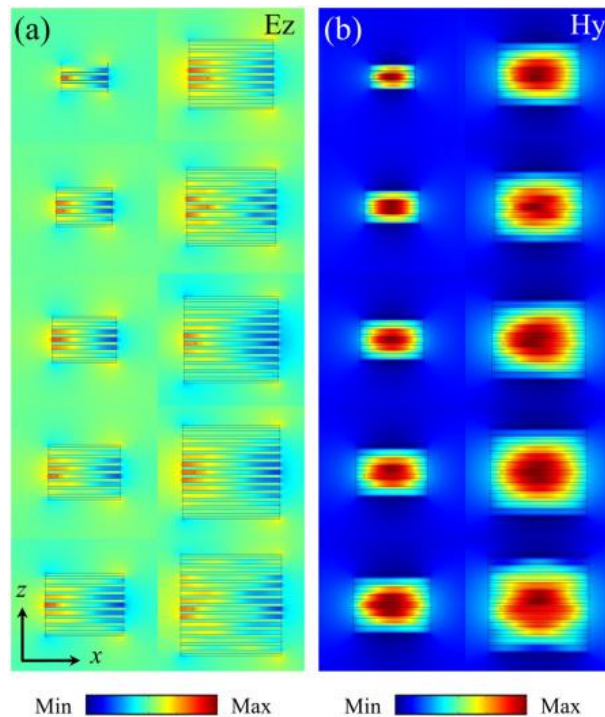


Figure 2. Fundamental electric (a) and magnetic (b) mode excited by an electric dipole placed inside each cavity. The electric dipole is positioned at the middle dielectric layer where the electric field is the maximum. All cavities are resonating with fundamental mode order (1, 1) at 850 nm.

To examine the quality factor of each designed nano-cavity, emission spectrum from an electric dipole from 750 nm to 1000 nm is obtained and fitted with the Lorentzian function [27]. The total quality factor is calculated by $Q_{tot} = \omega/\Delta\omega$, where ω is the cavity resonance frequency and $\Delta\omega$ is the full width at half maximum of the spectrum. As shown in Fig. 3(c), Q_{tot} gradually

increases and approaches to a constant of ~ 70 with the increase of wavevector. Both radiation and absorption contribute to the total quality factor $1/Q_{tot} = 1/Q_{rad} + 1/Q_{abs}$, however Q_{rad} dominates when there is no metal loss while Q_{abs} determines the upper bound when realistic metal loss and absorption is considered. Green triangles in Fig. 3(c) depicts that Q_{abs} is almost a constant and is independent of wavevector since absorption is strongly related to the material loss rather than the cavity geometry. However in contrary to the conventional 2D cavities, Q_{rad} scales inversely with the cavity size and is proportional to the wavevector following a third power law, giving $Q_{rad} \sim (k/k_0)^3$ as the red dashed line shows. This is because larger refractive mode index is supported and less radiation energy leaks out of cavity with increasing wavevectors for hyperbolic metamaterial nano-cavities [23]. This relationship can also be understood as $Q_{rad} \sim n/\alpha_{rad}$, where α_{rad} is radiation loss due to total internal reflection which is proportional to $(k/k_0)^2$ in two dimensions and n is proportional to k/k_0 , so Q_{rad} is linear proportional with $(k/k_0)^3$ [14, 27]. Thus at small wavevectors, Q_{tot} follows the $(k/k_0)^3$ scaling law as Q_{rad} , and gradually approaches Q_{abs} when k/k_0 increase.

Purcell factors can be obtained by Eq. (3) with the calculated quality factor and mode area, showing as the black up- and down- pointing triangles in Fig. 3(a). When the size of the cavity decreases and the corresponding wavevector increases, mode area of each cavity decreases but quality factor increases, which lead to the increase of Purcell factor. Without metal loss, a universal fifth power law $PF \sim (k/k_0)^5$ for the Purcell factor of the wavevector is demonstrated, agreed very well with the emission power ratio calculation. When metal loss and absorption is considered, at small wavevectors, the Purcell factor scaling law follows a fifth power law because radiation dominates the quality factor in this regime; while at large wavevectors, the scaling law follows a square law $PF \sim (k/k_0)^2$ as the black dashed line indicates. The reason is that huge moment mismatch between the cavity and free space reduces the radiation loss and the absorption dominates

the quality factor in the high k regime. Also most of the Purcell effect enhanced total dipole emission power radiates out from the cavity into far-field in small k regime but dissipates inside the cavity in the high k regime. Although the simulation is carried out in 2D, the relationship between Purcell factor and wavevector in 3D will follow a seventh power law with small wavevectors ($Q_{\text{rad}} \sim n/\alpha_{\text{rad}} \sim (k/k_0)^4$ and $V \sim (k/k_0)^3$) and approach to a third power law with large wavevectors, as predicated from the 2D results.

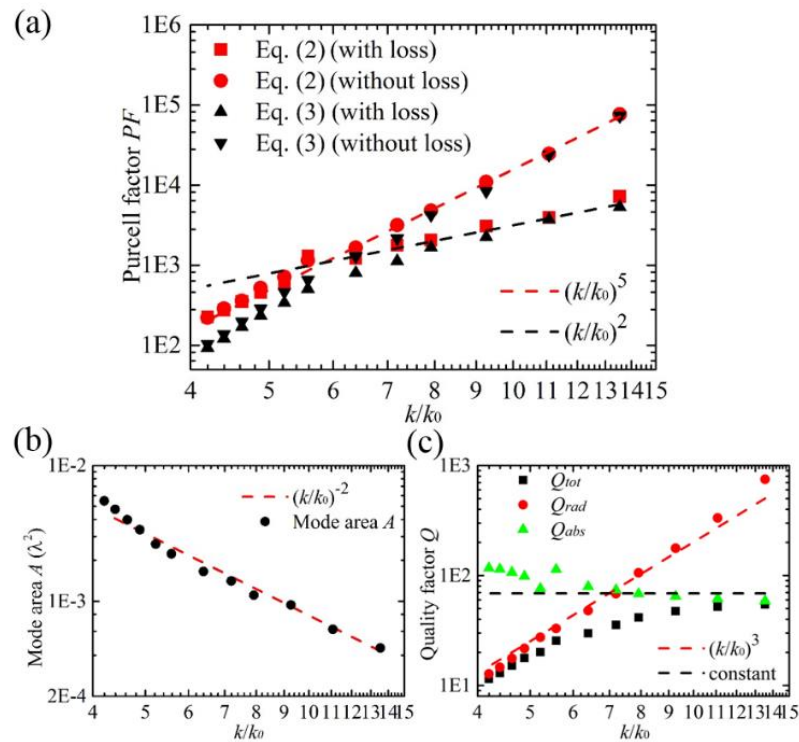


Figure 3. (a) Purcell factors of hyperbolic metamaterial nano-cavities as a function of k/k_0 . The red square and dot represent the Purcell factors calculated by total emission power with and without metal loss. The black up- and down- pointing triangle represent the Purcell factors calculated by Eq. (3) (b) Mode area as a function of wavevector. (c) Red dots represent Q_{rad} with the unique scaling law of $Q_{\text{rad}} \sim (k/k_0)^3$. Black squares and green triangulars represent Q_{tot} and Q_{abs} .

Furthermore, the dependences of Purcell factors on the dipole positions and moment orientations are investigated to reveal the possible experimental situations when quantum dots couple to the nano-cavities with random orientations and at various positions as shown in Fig. 4(a). Fig. 4(b) shows that Purcell factor reaches maximum when dipole locates at the electric field maximum and dipole moment is aligned parallel to the electric field E_z , and decreases when the dipole moment rotates due to the inefficient coupling to the cavity mode. Figs. 4(c, d) show the Purcell factor drops when dipole is placed on top of nano-cavity and vanishes when dipole moves along the x/z direction to the locations where electromagnetic fields are very weak. The calculated Purcell factors from emission power ratio agree very well with the Cos function and electric field distribution terms explicitly shown in Eq. (3).

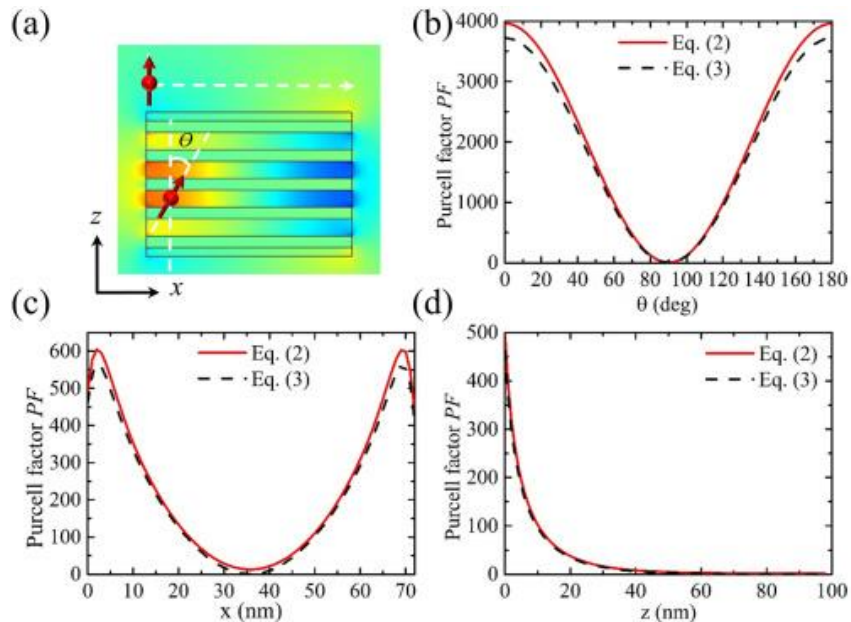


Figure 4. (a) Schematic of different dipole positions and orientations when it is coupled to the hyperbolic multilayer nano-cavity. (b) Dependence of Purcell factor on the dipole orientation, where θ is the angle between the dipole moment and the local electric field vector. $\theta = 0^\circ/180^\circ$ (90°) represents dipole moment along z (x) direction. (c, d). Calculated Purcell factor for dipole positions on top of the nanocavity moving along x/z directions (indicated by the white dashed lines).

4. CONCLUSION

Anomalous power law for the Purcell factors has been demonstrated for hyperbolic metamaterial cavities with dipole excitation. Contrary to conventional optical cavities, identical fundamental resonance mode is supported in a series of hyperbolic multilayer nano-cavities with different resonating wavevectors. A fifth power law $PF \sim (k/k_0)^5$ for small wavevectors and a square law $PF \sim (k/k_0)^2$ for large wavevectors have been shown for 2D hyperbolic cavities. The Purcell factors calculated from emission power ratio can be understood well from the scaling laws for quality factor and mode area of the cavity mode. The results provide a new aspect for investigating Purcell factors in hyperbolic metamaterial cavities, and could be of great interest for nanophotonic applications including cavity quantum electrodynamics, single photon sources, optical nonlinearities, optomechanics, fluorescence biosensing, and quantum communication.

ACKNOWLEDGMENTS

We thank Qian Wang for the help of discussion.

REFERENCES

- [1] Alivisatos, A.P., Semiconductor clusters, nanocrystals, and quantum dots. *science*, 1996. 271(5251): p. 933-937.
- [2] Liang, Y., et al., Functionalization of CdSe semiconductor nanocrystals with organic charge-transporting ligands. *Journal of Materials Chemistry C*, 2015. 3(16): p. 4134-4140.
- [3] Moon, J.-S., et al., Formation of water soluble wavelength tunable InGaP and InP quantum dots. *Polymer Bulletin*, 2016. 73(9): p. 2463-2475.
- [4] Eisaman, M.D., et al., Invited review article: Single-photon sources and detectors. *Review of scientific instruments*, 2011. 82(7): p. 071101.

- [5] Shalaginov, M.Y., et al., Enhancement of single-photon emission from nitrogen-vacancy centers with TiN/(Al, Sc) N hyperbolic metamaterial. *Laser & Photonics Reviews*, 2015. 9(1): p. 120-127.
- [6] Castelletto, S. and R. Scholten, Heralded single photon sources: a route towards quantum communication technology and photon standards. *The European Physical Journal-Applied Physics*, 2008. 41(3): p. 181-194.
- [7] Liang, Y., et al., Enhancement in the photorefractive performance of organic composites photosensitized with functionalized CdSe quantum dots. *Optical Materials*, 2016. 58: p. 203-209.
- [8] Toishi, M., et al., High-brightness single photon source from a quantum dot in a directional-emission nanocavity. *Optics express*, 2009. 17(17): p. 14618-14626.
- [9] Jin, X.R. and J. Gao, Quantum phase flip gate based on plasmonic double-bar resonators. *Optics letters*, 2013. 38(12): p. 2110-2112.
- [10] Jin, X.R., et al., Quantum entanglement in plasmonic waveguides with near-zero mode indices. *Optics letters*, 2013. 38(20): p. 4078-4081.
- [11] Flauraud, V., et al., In-plane plasmonic antenna arrays with surface nanogaps for giant fluorescence enhancement. *Nano letters*, 2017. 17(3): p. 1703-1710.
- [12] Moon, J.-S., et al., Off-resonance photosensitization of a photorefractive polymer composite using PbS nanocrystals. *The Journal of Physical Chemistry C*, 2015. 119(24): p. 13827-13835.
- [13] Purcell, E.M., H.C. Torrey, and R.V. Pound, Resonance absorption by nuclear magnetic moments in a solid. *Physical review*, 1946. 69(1-2): p. 37.
- [14] Englund, D., et al., Controlling the spontaneous emission rate of single quantum dots in a two-dimensional photonic crystal. *Physical review letters*, 2005. 95(1): p. 013904.
- [15] Guclu, C., et al., Radiative emission enhancement using nano-antennas made of hyperbolic metamaterial resonators. *Applied Physics Letters*, 2014. 105(12): p. 123101.
- [16] Lu, D., et al., Enhancing spontaneous emission rates of molecules using nanopatterned multilayer hyperbolic metamaterials. *Nature nanotechnology*, 2014. 9(1): p. 48.
- [17] Krishnamoorthy, H.N., et al., Topological transitions in metamaterials. *Science*, 2012. 336(6078): p. 205-209.

- [18] Chebykin, A., et al., Strong Purcell effect in anisotropic ϵ -near-zero metamaterials. *Physical Review B*, 2015. 91(20): p. 205126.
- [19] Li, L., et al., Enhanced quantum dot spontaneous emission with multilayer metamaterial nanostructures. *ACS Photonics*, 2017. 4(3): p. 501-508.
- [20] Li, Z., et al., All-metal structural color printing based on aluminum plasmonic metasurfaces. *Optics express*, 2016. 24(18): p. 20472-20480.
- [21] Sun, L., et al., Diffraction-free optical beam propagation with near-zero phase variation in extremely anisotropic metamaterials. *Journal of Optics*, 2015. 17(3): p. 035101.
- [22] Wang, W., et al., Realizing structural color generation with aluminum plasmonic V-groove metasurfaces. *Optics express*, 2017. 25(17): p. 20454-20465.
- [23] Yao, J., et al., Three-dimensional nanometer-scale optical cavities of indefinite medium. *Proceedings of the National Academy of Sciences*, 2011. 108(28): p. 11327-11331.
- [24] Ferrari, L., et al., Hyperbolic metamaterials and their applications. *Progress in Quantum Electronics*, 2015. 40: p. 1-40.
- [25] He, Y., et al., Infrared perfect absorber based on nanowire metamaterial cavities. *Optics letters*, 2013. 38(7): p. 1179-1181.
- [26] Chebykin, A., et al., Nonlocal effective medium model for multilayered metal-dielectric metamaterials. *Physical Review B*, 2011. 84(11): p. 115438.
- [27] Yang, X., et al., Experimental realization of three-dimensional indefinite cavities at the nanoscale with anomalous scaling laws. *Nature Photonics*, 2012. 6(7): p. 450.
- [28] Orlov, A.A., et al., Engineered optical nonlocality in nanostructured metamaterials. *Physical Review B*, 2011. 84(4): p. 045424.
- [29] Saleh, B.E., M.C. Teich, and B.E. Saleh, *Fundamentals of photonics*. Vol. 22. 1991: Wiley New York.
- [30] Li, Z., et al., Wavelength-selective mid-infrared metamaterial absorbers with multiple tungsten cross resonators. *Optics express*, 2018. 26(5): p. 5616-5631.
- [31] Koenderink, A.F., On the use of Purcell factors for plasmon antennas. *Optics letters*, 2010. 35(24): p. 4208-4210.
- [32] Englund, D., I. Fushman, and J. Vuckovic, General recipe for designing photonic crystal cavities. *Optics express*, 2005. 13(16): p. 5961-5975.

V. ENHANCED QUANTUM DOTS SPONTANEOUS EMISSION WITH METAMATERIAL PERFECT ABSORBERS

Wei Wang,¹ Xiaodong Yang,¹ Ting S. Luk², and Jie Gao¹

¹Department of Mechanical and Aerospace Engineering, Missouri University of Science and Technology, Rolla, MO 65409

²Center for Integrated Nanotechnologies, Sandia National Laboratories, Albuquerque, NM 87185, USA

ABSTRACT

Metamaterial perfect absorbers made of hexagonal array of holes on Ag-SiO₂-Ag thin films have been realized and utilized to enhance the spontaneous emission rate and photoluminescence intensity of CdSe/ZnS quantum dots spin-coated on the absorbers top surface. Perfect absorption of incoming light happens at the wavelength where the impedance is matched to that of the free space. When QDs strongly excite both the electric and magnetic resonances at this perfect absorption wavelength, significant Purcell effect on the spontaneous emission process and enhanced radiative outcoupling of photoluminescence intensity are expected. For perfect absorbers with near-unity absorption at the QDs emission wavelength of 620 nm, 5-fold Purcell enhancement of spontaneous emission rate and 3.6-fold enhancement of photoluminescence intensity are demonstrated in the time-resolved photoluminescence experiments, which are in good agreement with three-dimensional finite-difference time-domain simulation. These results will advance the understandings and applications of the metamaterial PAs-based light harvesting and emitting devices.

1. INTRODUCTION

Semiconductor quantum dots (QDs) emitters are widely used in various photonic and optoelectronic applications such as light-emitting devices [1], solar cells [2, 3], photodetectors [4], nano-lasers [5], single-photon sources [6], and photorefractive devices [7, 8]. Enhancing the spontaneous emission rates of QDs is essential for the fundamental research of quantum electrodynamics [9], and also important for the advances in single photon sources, low-threshold photonic and plasmonic lasers [10]. QDs spontaneous emission can be manipulated by engineering the local density of optical states and the cavity Purcell effect [11]. Over the past years, various optical nanostructures including nano-cavities [12-14], photonic crystals [15-17], plasmonic nano-antennas [18, 19] and metamaterials [20-23] have been extensively studied for the enhancement of the spontaneous emission rate and the photoluminescence radiative efficiency. Recently, metamaterial perfect absorbers (PAs) have drawn much attentions due to their capability to efficiently absorb light with subwavelength unit cells and have been widely used in many applications such as thermal photovoltaics [24], thermal emitters [25], sensors [26, 27] and color printing [28-31]. Perfect absorption arises from the presence of both electric resonance and magnetic resonance which results in the matched impedance to the free space. The impedance match condition implies that the radiative damping and resistive damping are identical for the eigenmode in perfect absorber devices [32, 33]. Coupling with metamaterial PA eigenmodes which have equal resistive dissipation and radiative outcoupling, QDs emitters will experience strong plasmon-exciton interactions and optimized radiative outcoupling at the desired wavelength, resulting in shortened QDs

photoluminescence decay lifetimes, large spontaneous emission Purcell factors and enhanced far-field photoluminescence intensity.

In this letter, the enhancement of spontaneous emission rate and photoluminescence intensity of CdSe/ZnS QDs coupled with metamaterial perfect absorbers was demonstrated. Metamaterial PAs made of hexagonal array of holes on Ag-SiO₂-Ag thin layers with near-unity perfect absorption were realized, and the PA resonance wavelengths can be tuned across 200 nm in the visible wavelength range by changing the period and hole radius of the unit cell structure. CdSe/ZnS QDs in polystyrene thin layer was spin-coated on the surface of the metamaterial PAs. Time-resolved and spectral-resolved photoluminescence measurements were performed to characterize the spontaneous emission rate and photoluminescence intensity from the QD-PA devices. For the on-resonance PAs with high absorption at the QDs emission wavelength, 5-fold Purcell enhancement of spontaneous emission rate and 3.6-fold enhancement of photoluminescence intensity were observed. Numerical simulations of the emission rate and intensity enhancement, as well as the dipole-excited electric and magnetic field distributions, were carried out with 3D finite-difference time-domain (FDTD) method, which agrees well with the experimental findings. This work not only has shown the enhanced QDs spontaneous emission rates when the dipole emitters strongly couple to the on-resonance perfect absorbers, but also has revealed that maximum photoluminescence intensity enhancement is achieved at the same time due to the satisfied impedance match condition for the PA eigenmode with balanced resistive dissipation and radiative outcoupling at the resonance wavelength. The results pave the way to the understanding of enhanced QDs spontaneous emission and radiative outcoupling processes in the

metamaterial perfect absorbers, also the advancement of metamaterial PAs-based applications in light harvesting, light-emitting devices, solar cells, photodetectors, optical sensors, nano-scale lasers and single-photon sources.

2. MATERIALS AND METHODS

Fig. 1 (a) shows the three-dimensional schematic of metamaterials PAs with hexagonal array of holes patterned on the top silver layer of the Ag-SiO₂-Ag three-layer structure. The bottom 100nm Ag layer is deposited using an electron-beam evaporator system on top of a silicon wafer. The 45 nm SiO₂ spacer and the top 25 nm Ag layer are then deposited with sputtering method (Kurt J. Lesker), where Ag is deposited at the rate of 0.4 Å/sec and SiO₂ is deposited at 0.2 Å/sec. The optical constant of both materials and the film thicknesses are characterized with the variable angle spectroscopic ellipsometry (VASE, J. A. Woollam Co. VB400/HS-190). A layer of polystyrene mixed with CdSe/ZnS QDs [34] is spin-coated over the PAs surface. A one-step Focused Ion Beam (FIB) milling (FEI Helios Nanolab 600 Dual Beam, 30 KV, 9.7 pA) is used to fabricate the nanostructures, and Fig. 1 (b) presents the typical scanning electron microscope (SEM) cross section view of the PAs. By changing the structure period P and hole radius r , the PA resonance frequency can be tuned across the whole visible frequency region [35]. In order to match the QDs emission wavelength at 620 nm, PA2 with period P of 230 nm and hole radius r of 65 nm is designed to be on-resonance with the QDs emission and the SEM image is shown in Fig.1 (d). Three other PAs with absorption resonances detuned from the QDs emission wavelength are also designed and fabricated, and the SEM images are shown in

Fig. 1(c, e, f) with different lattice geometrical parameters (c: $P = 155$ nm, $r = 40$ nm; e: $P = 280$ nm, $r = 80$ nm; f: $P = 315$ nm, $r = 90$ nm).

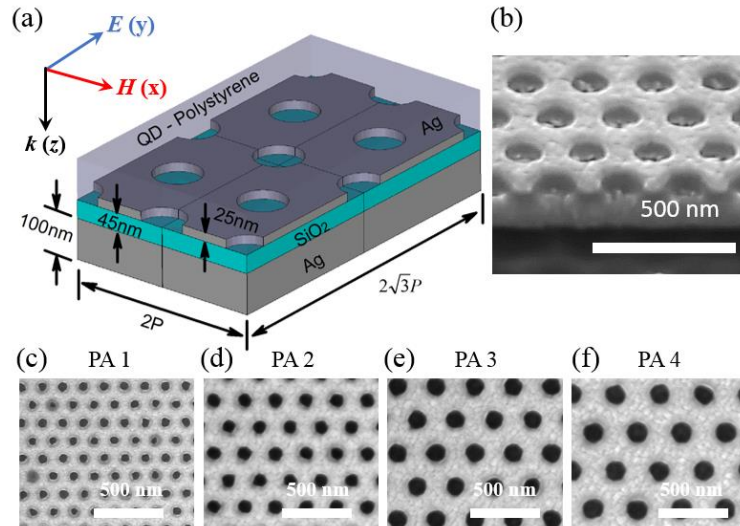


Figure 1. (a), Schematic view of metamaterial PAs made of hexagonal array of holes on the Ag -SiO₂ -Ag three-layer structure with the spin-coated QD-polystyrene film. (b), SEM cross section of metamaterial PA fabricated by FIB with period of 230 nm and hole radius of 65 nm. (c-f), SEM images of four structures with different lattice geometrical parameters (c: $P = 155$ nm, $r = 40$ nm; d: $P = 230$ nm, $r = 65$ nm; e: $P = 280$ nm, $r = 80$ nm; f: $P = 315$ nm, $r = 90$ nm).

Reflectance spectra of the fabricated four metamaterial PAs are measured by a home-built microscope with a halogen lamp and a fiber-coupled spectrometer, and the plots are shown in Fig.2 (a-d) respectively. Narrow resonances with nearly perfect absorption and very low reflectance are obtained at 524 nm, 618 nm, 683 nm, and 737 nm respectively for the device PA1, PA2, PA3 and PA4 covered with QDs layer. The gray shaded area (PL₀) in Fig. 2 represents the photoluminescence emission spectrum of CdSe/ZnS QDs centered on 620nm. As depicted clearly, the absorption resonance in the reflectance spectrum of PA2 with period 230 nm and radius 65 nm matches with the QDs emission

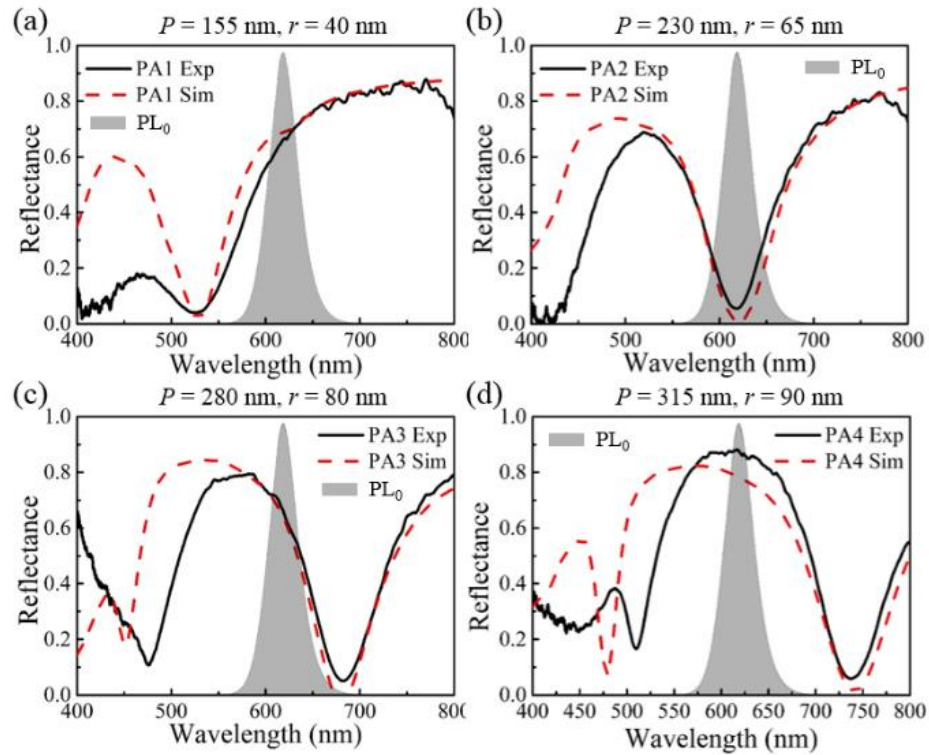


Figure 2. Measured optical reflectance spectra of QD-polystyrene coated metamaterial PA1 (a), PA2 (b), PA3 (c) and PA4 (d) with different geometrical parameters as designed and fabricated in Fig.1. The red dashed lines are simulated reflectance spectra using the FDTD method.

wavelength perfectly with nearly perfect absorption ($A = 0.95$) and nearly zero reflectance ($R = 0.05$); while the resonance of PA1 (PA3) is blue-shifted (red-shifted) relative to the center of the QDs emission and the absorption is 0.33 (0.35) at 620 nm. PA4 is largely off-resonance and the absorption at the QDs emission wavelength is very low ($A = 0.13$). Notably, perfect absorption of incoming light in PA2 at 620 nm arises from the presence of both electric resonance and magnetic resonances which results in the matched impedance to the free space [33]. Therefore, the coupling strength between QDs and the PA resonant mode, which plays an essential role in the QDs emission process, is greatly enhanced. The on-resonance PA2 is expected to have the most significant Purcell effect

which leads to the largest spontaneous emission rate among the four designed devices, as well as the maximum radiative outcoupling and photoluminescence intensity enhancement when working with impedance match condition. The red dashed lines in Fig. 2 are simulation results using FDTD method, which agree very well with the measured resonance wavelengths and reflectance spectra.

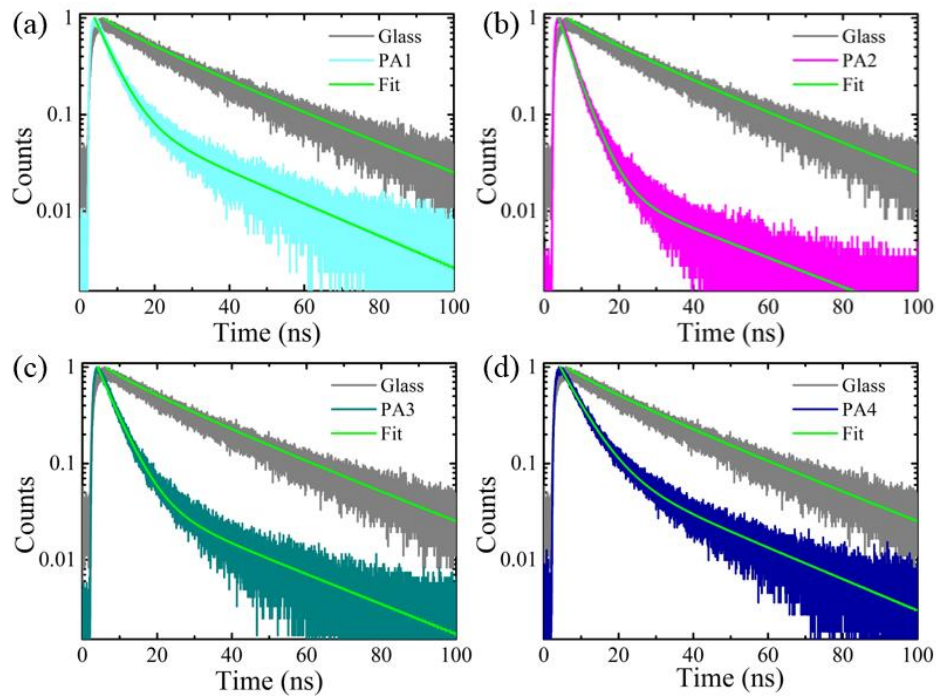


Figure 3. Normalized TCSPC histograms and fitting results for QDs photoluminescence decays on the four metamaterial PAs and glass substrate.

To demonstrate the Purcell effect of the metamaterial perfect absorbers, time-resolved photoluminescence decay measurements of QDs on the PAs and glass substrate (control) are carried out using a time-correlated single photon counting (TCSPC) system and a 402 nm picosecond pulsed laser with $0.25 \mu\text{W}$ excitation power. Fig. 3 (a-d) shows the photoluminescence decay data from QDs on the four PAs at emission wavelength of

620 nm, where faster decays are observed on the four PAs than that on the glass substrate. It is also observed that the photoluminescence decay on PA2 is faster compared to that on other PAs, indicating a stronger Purcell effect of the on-resonance PA2 with nearly perfect absorption. Spontaneous emission decay lifetime of the QDs is obtained by fitting the experimental photoluminescence decay curves using a two-exponential relaxation model [20, 22] and averaged from ten measurements for each PA designs. For on-resonance PA2, the photoluminescence firstly decays with a shorter lifetime of $t_1 \sim 4.28 \pm 0.06$ ns which is attributed to the QDs strongly coupled to the PA resonant mode and slows down to a longer lifetime of $t_2 \sim 32.04 \pm 0.97$ ns which is determined mainly by those QDs away from the PA surface, whereas the QDs decay on the glass substrate control sample shows a similar long lifetime of $t_0 \sim 20.88 \pm 0.01$ ns. The shortened QDs decay lifetime on device PA1, PA3 and PA4 are 4.77 ± 0.12 ns, 4.81 ± 0.09 ns and 5.89 ± 0.11 ns respectively. Fig. 4(a) illustrates the emission rate enhancement of the four PAs, which is obtained by normalizing the QDs decay lifetime t_0 on the glass substrate with the decay lifetime t_1 of QDs coupled to the PAs. Five-fold emission rate enhancement from PA2 is shown, which is the largest among the four devices. The strengthened coupling between QDs and PA resonant mode in PA2 with perfect absorption and impedance match at 620 nm contributes to the enhanced spontaneous emission rate in the measurement. For PA1 and PA3 with absorption of 0.33 and 0.35 at 620nm, similar level of emission rate enhancement (~ 4.3) is observed. However, small emission rate enhancement is reported for the most off-resonance PA4 due to the weak coupling strength between QDs and the PA mode in this device. The emission rate enhancement is also modeled with 3D FDTD simulation and averaged from electrical dipole emitters with three orthogonal polarizations and at 28 different positions (in first

quadrant due to symmetry) located 15 nm above the PAs surface. The simulation results in Fig. 4(b) show excellent agreement with the experiment results for the comparison of QDs emission rate enhancement on the four PAs.

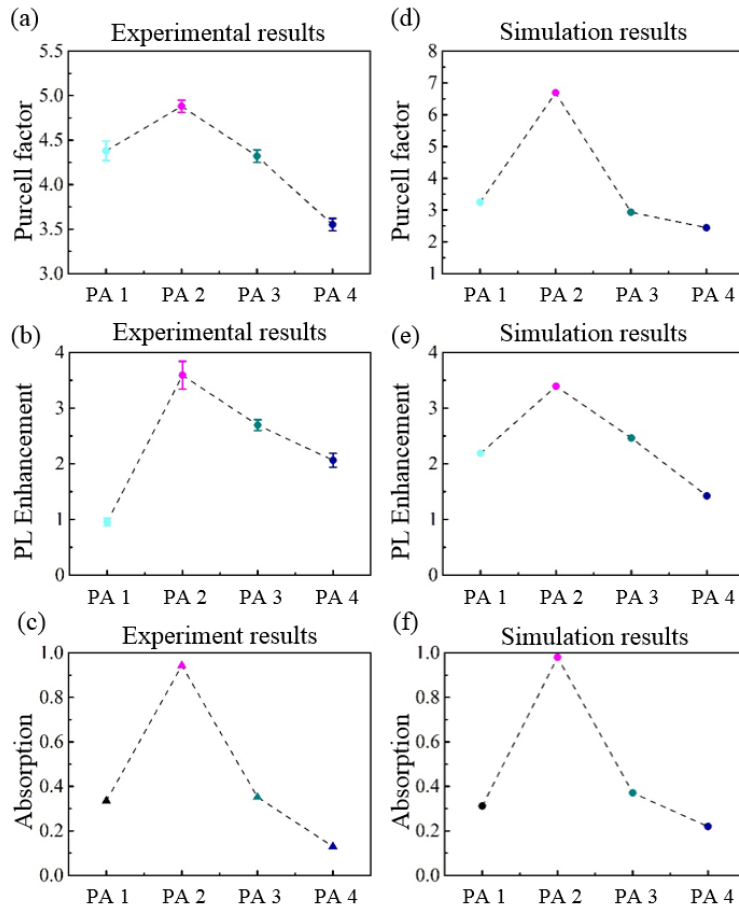


Figure 4. Experiment and simulation results for spontaneous emission rate enhancement (a, b) and photoluminescence intensity enhancement (c, d) of the four metamaterial PAs coupled with QDs at 620 nm.

In order to understand the enhancement effect on photoluminescence intensity radiated from the PAs, photoluminescence spectra from the four QD-PA devices is measured by a Horiba spectrometer and a liquid N₂ cooled CCD. Photoluminescence

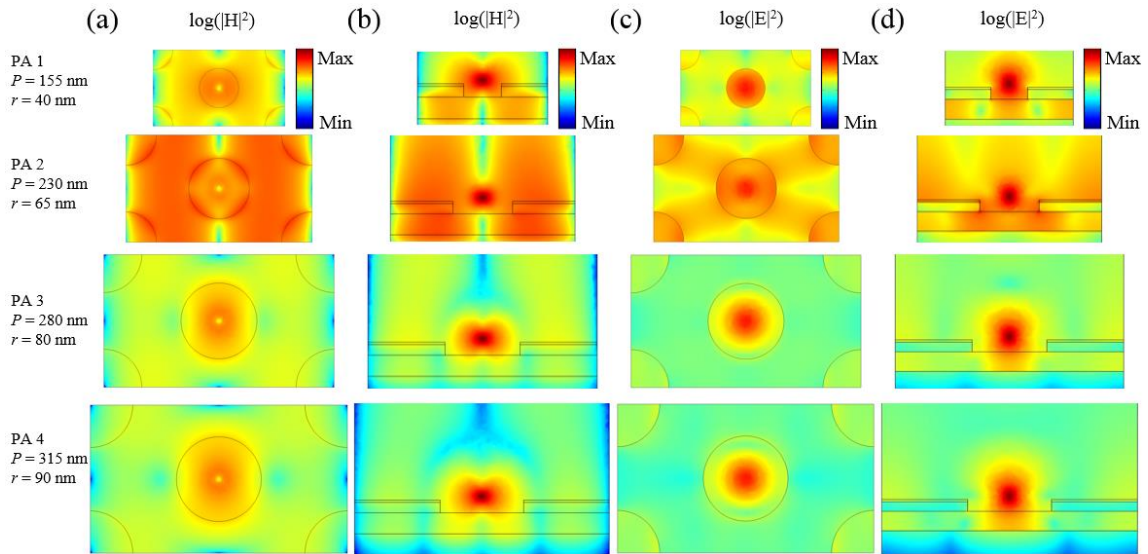


Figure 5. Top (a) and side (b) views of magnetic field intensity distribution excited by a z-polarized electric dipole emitter at 620 nm, located at the center of the hole and 10 nm above the surface of the four PAs. (c-d) shows the top and side views of electric field intensity distribution.

intensity from the four PAs at 620 nm is obtained and the intensity enhancement is shown in Fig. 4(c) by normalizing to the QDs photoluminescence intensity on glass substrate. The on-resonance PA2 shows the largest photoluminescence intensity enhancement ~ 3.6 among the four devices, resulting from both enhanced QDs emission rate and radiative outcoupling when QDs couple strongly with the PA resonant mode with impedance match condition. Simulation results of photoluminescence intensity collected within the collection angle 33.4 degree (corresponds to the objective lens NA = 0.55 used in experiment) at a far-field plane from the PAs surface normalized by that from glass substrate are presented in Fig. 4(d), which also agrees with the observations in the experiment observations. It is worth mentioning that the general trend of spontaneous emission rate enhancement and photoluminescence intensity enhancement for the four PAs devices is more or less the same with the trend of PAs absorption, which suggests that the

QDs spontaneous emission process and the radiative outcoupling are greatly enhanced in the metamaterial PAs with high absorption and impedance match at the desired emission wavelength.

To show more clearly the excitation of the absorption resonances in the metamaterial PAs by QDs emitters and the efficient outcoupling from the QD-PA devices, electric and magnetic field intensity distributions are illustrated in Fig. 5 with the excitation from an electric dipole emitter with dipole moment along the vertical z direction and emission wavelength of 620 nm. The top view cut at the middle of the top silver layer is shown in Fig. 5(a, c) and the side cross-section view is presented in Fig. 5(b, d). As expected, the dipole emission strongly excites the electric and magnetic resonances in PA2, and both the intensive electromagnetic resonant mode confinement and the strong radiative outcoupling contribute to the observed spontaneous emission rate enhancement and photoluminescence intensity enhancement in the experiment. Furthermore, simulations also verify that placing QDs in the middle of SiO_2 spacing layer at the locations of the electromagnetic fields maxima will result in stronger exciton-plasmon coupling and larger Purcell factors.

3. CONCLUSIONS

We have experimentally demonstrated the enhancement of CdSe/ZnS QDs spontaneous emission rates and photoluminescence intensity with metamaterial perfect absorbers, which consist of hexagonal array of holes on a Ag- SiO_2 -Ag thin films through rational design, and possess near-unity absorption at the QDs emission wavelength. Numerical simulations of the emission rate and intensity enhancement on the four studied

QD-PA devices, as well as the electromagnetic fields distribution under dipole emitter excitation, have been conducted to assist the comprehensive understanding of the experimental observations. The enhanced plasmon-exciton couplings between the emitters and PA resonate modes provides the possibility of controlling the QDs emission processes towards the useful applications in the metamaterial PAs-based light harvesting and emitting devices.

ACKNOWLEDGMENTS

The authors thank Drs. Yichen Liang, Ling Li and Fei Cheng for the useful discussion. The authors acknowledge the support from the National Science Foundation (ECCS-1653032 and DMR-1552871) and the Office of Naval Research (No. N00014-16-1-2408). This work was performed, in part, at the Center for Integrated Nanotechnologies, an Office of Science User Facility operated for the U.S. Department of Energy (DOE) Office of Science. Sandia National Laboratories is a multi-program laboratory managed and operated by Sandia Corporation, a wholly owned subsidiary of Lockheed Martin Corporation, for the U.S. Department of Energy's National Nuclear Security Administration under contract DE-AC04- 94AL85000.

REFERENCES

- [1] Shirasaki, Y., et al., Emergence of colloidal quantum-dot light-emitting technologies. *Nature Photonics*, 2013. **7**(1): p. 13.
- [2] Nozik, A., Quantum dot solar cells. *Physica E: Low-dimensional Systems and Nanostructures*, 2002. **14**(1-2): p. 115-120.

- [3] Robel, I., et al., Quantum dot solar cells. Harvesting light energy with CdSe nanocrystals molecularly linked to mesoscopic TiO₂ films. *Journal of the American Chemical Society*, 2006. 128(7): p. 2385-2393.
- [4] Konstantatos, G., et al., Ultrasensitive solution-cast quantum dot photodetectors. *Nature*, 2006. 442(7099): p. 180.
- [5] Strauf, S., et al., Self-tuned quantum dot gain in photonic crystal lasers. *Physical review letters*, 2006. 96(12): p. 127404.
- [6] Michler, P., et al., A quantum dot single-photon turnstile device. *science*, 2000. 290(5500): p. 2282-2285.
- [7] Liang, Y., et al., Enhancement in the photorefractive performance of organic composites photosensitized with functionalized CdSe quantum dots. *Optical Materials*, 2016. 58: p. 203-209.
- [8] Moon, J.-S., et al., Off-resonance photosensitization of a photorefractive polymer composite using PbS nanocrystals. *The Journal of Physical Chemistry C*, 2015. 119(24): p. 13827-13835.
- [9] Cohen-Tannoudji, C., J. Dupont-Roc, and G. Grynberg, Photons and Atoms-Introduction to Quantum Electrodynamics. *Photons and Atoms-Introduction to Quantum Electrodynamics*, by Claude Cohen-Tannoudji, Jacques Dupont-Roc, Gilbert Grynberg, pp. 486. ISBN 0-471-18433-0. Wiley-VCH, February 1997., 1997: p. 486.
- [10] Oulton, R.F., et al., Plasmon lasers at deep subwavelength scale. *Nature*, 2009. 461(7264): p. 629.
- [11] Purcell, E.M., H.C. Torrey, and R.V. Pound, Resonance absorption by nuclear magnetic moments in a solid. *Physical review*, 1946. 69(1-2): p. 37.
- [12] Toishi, M., et al., High-brightness single photon source from a quantum dot in a directional-emission nanocavity. *Optics express*, 2009. 17(17): p. 14618-14626.
- [13] Gan, X., et al., Controlling the spontaneous emission rate of monolayer MoS₂ in a photonic crystal nanocavity. *Applied physics letters*, 2013. 103(18): p. 181119.
- [14] Russell, K.J., et al., Large spontaneous emission enhancement in plasmonic nanocavities. *Nature Photonics*, 2012. 6(7): p. 459.
- [15] Noda, S., M. Fujita, and T. Asano, Spontaneous-emission control by photonic crystals and nanocavities. *Nature photonics*, 2007. 1(8): p. 449.

- [16] Englund, D., et al., Controlling the spontaneous emission rate of single quantum dots in a two-dimensional photonic crystal. *Physical review letters*, 2005. 95(1): p. 013904.
- [17] Lodahl, P., S. Mahmoodian, and S. Stobbe, Interfacing single photons and single quantum dots with photonic nanostructures. *Reviews of Modern Physics*, 2015. 87(2): p. 347.
- [18] Kinkhabwala, A., et al., Large single-molecule fluorescence enhancements produced by a bowtie nanoantenna. *Nature Photonics*, 2009. 3(11): p. 654.
- [19] Flauraud, V., et al., In-plane plasmonic antenna arrays with surface nanogaps for giant fluorescence enhancement. *Nano letters*, 2017. 17(3): p. 1703-1710.
- [20] Li, L., et al., Enhanced quantum dot spontaneous emission with multilayer metamaterial nanostructures. *ACS Photonics*, 2017. 4(3): p. 501-508.
- [21] Lu, D., et al., Enhancing spontaneous emission rates of molecules using nanopatterned multilayer hyperbolic metamaterials. *Nature nanotechnology*, 2014. 9(1): p. 48.
- [22] Krishnamoorthy, H.N., et al., Topological transitions in metamaterials. *Science*, 2012. 336(6078): p. 205-209.
- [23] Sun, L., et al., Diffraction-free optical beam propagation with near-zero phase variation in extremely anisotropic metamaterials. *Journal of Optics*, 2015. 17(3): p. 035101.
- [24] Atwater, H.A. and A. Polman, Plasmonics for improved photovoltaic devices. *Nature materials*, 2010. 9(3): p. 205.
- [25] Tsai, M.-W., et al., High performance midinfrared narrow-band plasmonic thermal emitter. *Applied physics letters*, 2006. 89(17): p. 173116.
- [26] Liu, N., et al., Infrared perfect absorber and its application as plasmonic sensor. *Nano letters*, 2010. 10(7): p. 2342-2348.
- [27] Cheng, F., X. Yang, and J. Gao, Enhancing intensity and refractive index sensing capability with infrared plasmonic perfect absorbers. *Optics letters*, 2014. 39(11): p. 3185-3188.
- [28] Cheng, F., et al., Enhanced structural color generation in aluminum metamaterials coated with a thin polymer layer. *Optics express*, 2015. 23(19): p. 25329-25339.
- [29] Li, Z., et al., All-metal structural color printing based on aluminum plasmonic metasurfaces. *Optics express*, 2016. 24(18): p. 20472-20480.

- [30] Wang, W., et al., Realizing structural color generation with aluminum plasmonic V-groove metasurfaces. *Optics express*, 2017. 25(17): p. 20454-20465.
- [31] Cheng, F., et al., Aluminum plasmonic metamaterials for structural color printing. *Optics express*, 2015. 23(11): p. 14552-14560.
- [32] Cui, Y., et al., Plasmonic and metamaterial structures as electromagnetic absorbers. *Laser & Photonics Reviews*, 2014. 8(4): p. 495-520.
- [33] He, Y., et al., Infrared perfect absorber based on nanowire metamaterial cavities. *Optics letters*, 2013. 38(7): p. 1179-1181.
- [34] Liang, Y., et al., Functionalization of CdSe semiconductor nanocrystals with organic charge-transporting ligands. *Journal of Materials Chemistry C*, 2015. 3(16): p. 4134-4140.
- [35] Cheng, F., et al., Structural color printing based on plasmonic metasurfaces of perfect light absorption. *Scientific reports*, 2015. 5: p. 11045.

VI. SELECTIVE CHIRAL SPONTANEOUS EMISSION OF QUANTUM DOTS ON CHIRAL METASURFACE

Wei Wang,¹ Xiaodong Yang,¹ Jie Gao¹

¹Department of Mechanical and Aerospace Engineering, Missouri University of Science and Technology, Rolla, MO 65409

ABSTRACT

Chirality is a fascinating geometrical property that chiral object and its mirror image cannot coincide with each other by rotational or translational operation. Both light and material can be chiral and their interaction such as circular dichroism have been investigated intensively. However, the control of chiral spontaneous emission of dipole emitters still remains open. We designed and demonstrated theoretically and experimentally a chiral-selective plasmonic absorber based on tilted ellipse array on trilayer to control the chiral spontaneous emission property of dipole emitters such as quantum dots. The associated chiral-selective absorption band that strongly absorb one-handed circular polarized light and reflect the other results in significant circular dichroism. By position the QD on the top of metasurface, we demonstrate a sharp difference in their interaction with the right-hand polarized (RCP) and left-hand polarized (LCP) metasurface modes. The difference in RCP and LCP spontaneous emission lifetime and photoluminescence intensity were demonstrated experimentally. Theoretical mode analysis were conducted to explain the mode coupling mechanism. Our observations of chiral mode engineering for spontaneous emission control enable a variety of promising

applications in active polarization manipulation, chiral imaging and sensing, chiroptical spectroscopy, Stereochemical enantiomer sensors.

1. INTRODUCTION

Chirality has long been investigated in various subjects such as physics, chemistry, mathematics and biology [1]. According to the definition by Lord Kelvin, chirality is a fascinating geometrical property that chiral object and its mirror image cannot coincide with each other by rotational or translational operation[2]. The two enantiomorphs of a chiral object have left- and right-handed version that possess the same chemical and physical properties but different response on circular polarized light which can be represented by the superposition by two independent linear polarized light by the phase difference of 90 degree. Extensive research has been performed on the interaction between circular polarized light and chiral object, but research on controlling of chiral spontaneous emission of dipole emitters is limited. The control of spontaneous emission of dipole emitters on photonic structures relies on enhanced light-matter interactions named Purcell effect due to highly localized electric field and longer interaction time, i.e., small mode volume and high quality factor [3, 4]. Material with large optical chirality is desired for such a purpose because the chiral material provide higher density of state for one circular polarized photon than that of the other and thus the dipole emitter emits more corresponding circular polarized than the other. For natural materials, optical chirality is usually very weak, thus chiral metamaterials that has large chiral dichroism (CD) has been widely investigated in recent years. Metamaterial and metasurface consist of nondiffracting subwavelength array of structures act as meta-atom have been developed for several years

widely used in many applications such as negative refractive and epsilon-near-zero metamaterials[5, 6], perfect absorbers[7, 8], and color printings[9, 10]. 3D metamaterials always show large chiral optical response can enhance chiral optical response for several orders of magnitude than natural material, but the fabrication process is complicated which significantly reduce their application potentials[11]. 2D metasurface as a new emerging materials which use metallic nanostructure localized surface plasmon resonances to create chiral metamaterials that have high sensitivity to circular polarized light could significantly simplify the fabrication process and inheritable compatible with Complementary metal–oxide–semiconductor (COMS) process [12-16]. The 2D chiral plasmonic metasurface can enormously enhance chiral spontaneous emission due to strong field confinement and the ability to support good coupling to free space.

In this paper, we have designed and demonstrated the tilted ellipse array on Au-SiO₂-Au trilayers that has large CDR at visible wavelength for the first time. Maximum absorption of selected circular polarized light exceeding 80% associated with CDR over 0.65 at 725nm were achieved experimentally. To tailor the chiral spontaneous emission of dipole emitter, we spin coated the CdSe/ZnS quantum dots[17, 18] loaded in polymer on the top of chiral metasurface and measured the spectral resolved and time resolved LCP and RCP photonluminescence (PL). The high CDR which originates from the circularly dichroic mode coupling process greatly facilitate the control of chiral spontaneous emission and the circular dichroism of photonluminescence (CDPL) as much as 0.1 was observed which match our expectation. Mode analysis and PL simulation was performed using finite element method in order to further elucidate this chiral optical mechanism. This coupling mechanism opens a new opportunity to control the spontaneous emission of dipole emitters

and this kind of chiral metasurface can greatly benefit the sensing and generation of circular polarized light. Particularly, the negative structure allows for inherent electrical connection among all elements which greatly facilitate the optoelectric device design. At the same time, our design offer simple fabrication and low cost manufacturing method. This pave the way towards novel functional chiroptical devices such as chiroptical spectroscopy, Stereochemical enantiomer sensors, and chiral-selective thermal emitters.

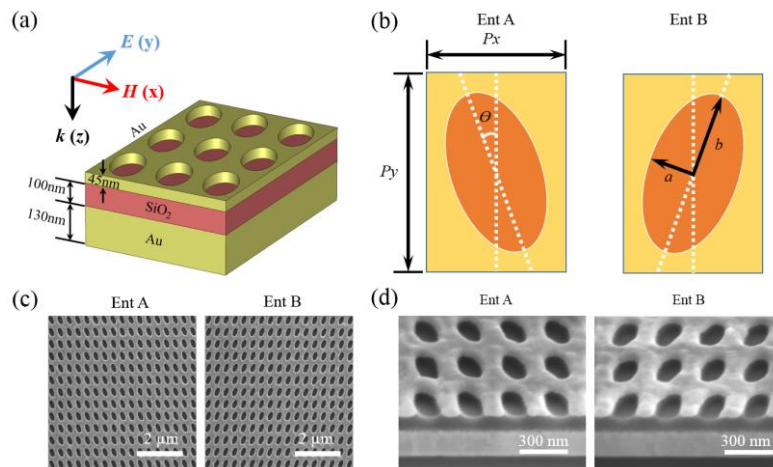


Figure 1. (a) 3D schematic of ellipse array multilayer structures consists of 45 nm top Au, 100 nm SiO₂ spacer and 130 nm Au reflector on silicon base. (b) Parameter of tilted ellipse enantiomer A and B with period P_x and P_y . Ellipse short and long axis are noted as a and b . θ is ellipse tilted angle. (c) Top view of SEM picture of two enantiomers. (d) Tilted view at 53 degree of SEM picture of two enantiomers.

2. CHIRAL METASURFACE DESIGN AND CHARACTERIZATION

Fig. 1 (a) shows the three-dimensional schematic of chiral metasurface with tilted elliptical hole arrays patterned on the top Au layer of the Au-SiO₂-Au multilayer stack. An electron beam evaporation system is used to deposit the multilayer stack on silicon

substrates. Top view schematics of the two enantiomers A and B are shown in Fig. 1(b), where the unit cell periods $P_x = 300$ nm, $P_y = 400$ nm, semi-minor axis of the ellipse $a = 200$ nm, semi-major axis of the ellipse $b = 300$ nm, and ellipse tilted angle $\theta = 20^\circ$ (-20°) for enantiomer A (B). The tilted elliptical arrays are fabricated on the top Au layer via focused ion beam milling (FEI Helios Nanolab 600 Dual Beam) with a gallium ion current of 9.7 pA and an accelerating voltage of 30 KeV. Scanning electron microscope (SEM) images in Fig.1 (c-d) present the top views and cross-section views of the fabricated chiral metasurfaces with arrays of two enantiomer A and B.

The reflectance spectrum (Fig. 2 (a, b)) of chiral metasurface was measured by a home-build microscope setup to characterize the chiral optical properties of the two enantiomers. The reflectance spectrum of the two samples were measured with illumination of left-handed circular polarized (LCP) and right-handed circular polarized (RCP) waves respectively. For enantiomer A, as illustrated in Fig. 2 (a) at around 725nm the chiral sensitive absorption band was clearly identified. The enantiomer A absorb LCP and reflect RCP light within this band. In order to further illustrate the chiral reflection property, circular polarization dependent analysis of reflectance spectrum was performed and depicted in Fig. 2 (d). For enantiomer A, the LCP/RCP component of reflected was separated using quarter wave plate and liner polarizer and denoted as R_{LL}/R_{RL} and R_{LR}/R_{RR} when illuminated with LCP/RCP light as illustrated in Fig. 2 (d). Due to the symmetry, R_{LR} and R_{RL} should be same and the experiment results justify this claim. The chiral selective absorption was due to the huge difference between R_{RR} and R_{LL} at resonant wavelength around 725nm. It is worth noting that at resonant wavelength (around 725nm), the reflected light will preserve its initial circular polarization whereas the regular mirror

which flip the spin state of circular polarized light upon reflection. Such as in Fig. 2 (c), when enantiomer A was illuminated by RCP light with wavelength around 725nm, R_{LR} almost equal to zero and most of the reflected light is RCP light. To elucidate the physical mechanism of the chiral response, charge-oscillation Eigen mode analysis was also performed under illumination of RCP and LCP incidence light at 725nm. Electric field mode distributions of the two enantiomers at horizontal plane 10nm under top Au surface were plotted in Fig. 2 (f). Fig. 2 (g) shows the electric field mode distribution at the vertical cross section at the right border of unit cell. The pronounced electric field intensity was shown clearly for incidence of LCP/RCP wave which corresponds to the strong absorption of RCP/LCP light at resonant wavelength. When light illuminate at the metasurface, magnetic dipoles directed perpendicular to the light propagation direction can be generated due to the multilayer structure. The coupling between electric and magnetic dipoles was sensitive to the spin state of incident light due to the broken mirror symmetry. It is worth noting that our design can achieve extraordinary chiral optical response by simple planar structures through breaking unit cell mirror symmetry and thus dramatically decrease fabrication complexity. This chiral selective electric field enhancement will facilitate the chiral selective spontaneous photon emission of dipole emitters such as quantum dots which will be presented and discussed in the following sections.

For enantiomer B, the complementary behavior of reflectance spectrum (Fig. 2 (b)) elucidate the enantiomer symmetry very well. Fig. 2 (c) shows the chiral dichromic of reflectance (CDR) calculated by equation $CDR = (R_{LCP} - R_{RCP}) / (R_{LCP} + R_{RCP})$. The experiment CDR result as much as 0.65 was shown which indicates the large chiral optical sensitives. The additional reflection band at around 600nm exhibits no chiral selectivity

behavior. The large chiral dichroism can be explained that the tilted elliptical unit cell break the in-plane mirror symmetry and results in chiral optics response. The optically thick bottom Au layer on Si substrate provides a spin-state selective resonant cavity thus largely enhances the chiral optics response of the metasurface. The full-wave simulation results (dashed lines in Fig. 2 (a, b) and Fig. 2 (e)) calculate by finite element method indicates great agreement with experimental results.

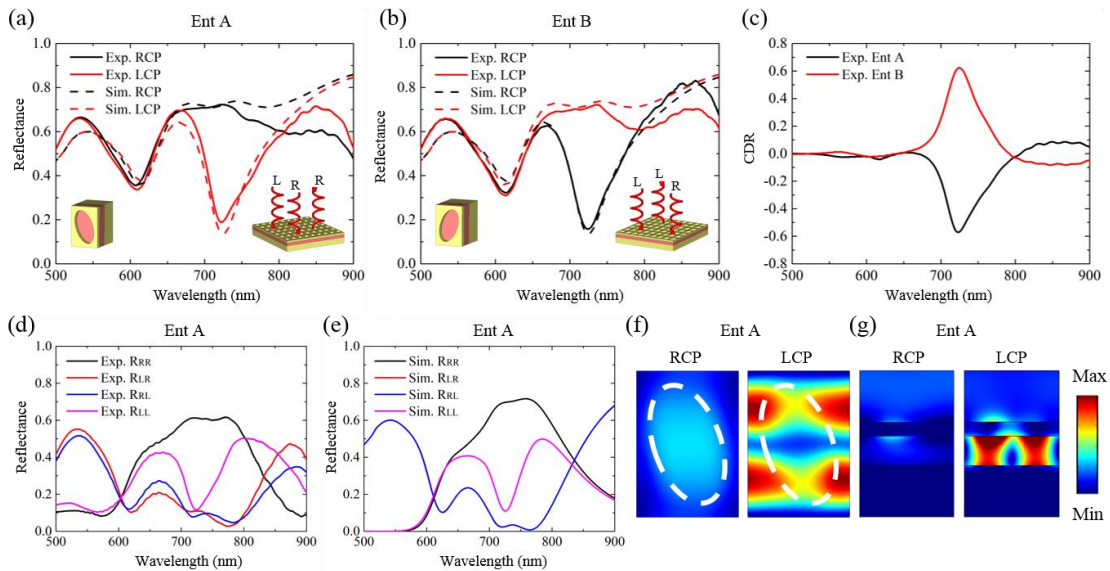


Figure 2. (a, b) Experimental (solid line) and simulation (dashed line) reflectance results of two enantiomers. (c) Experimental CDR of two enantiomers. (d, e) Experimental and simulation LCP and RCP component reflected spectrum of two enantiomers. (f). Electric field mode distribution of two enantiomers at different LCP and RCP incidence at resonance wavelength 725nm. The horizontal cross section is set 10nm beneath the top Au layer. (g) Electric field mode distribution at the vertical cross section at the right border of unit cell.

To further demonstrate the ability of chiral selective reflection, windmill pattern composed of two enantiomers (Fig. 3 (a)) was fabricated using FIB. The final pictures were taken under the illumination of LCP/RCP light without any wave plate or polarizer in the

collection optical path. At resonant wavelength 725nm, the complementary pictures unambiguously demonstrate the chiral dichroism of reflection. When changing the wavelength from resonant wavelength 725nm to non-resonant wavelength 825nm with a step of 25nm, the chiral dichroism gradually disappears. Fig. 3 (b) shows the picture at the illumination of two typical on and off resonant wavelength. In Fig. 3 (c), the red and black dot represent the measured normalized intensity difference ($I_{LCP} - I_{RCP}$) of two different enantiomer area in Fig. 3 (b). These normalized intensity difference results match the reflectance spectrum difference of previous sample (solid red and black line) very well.

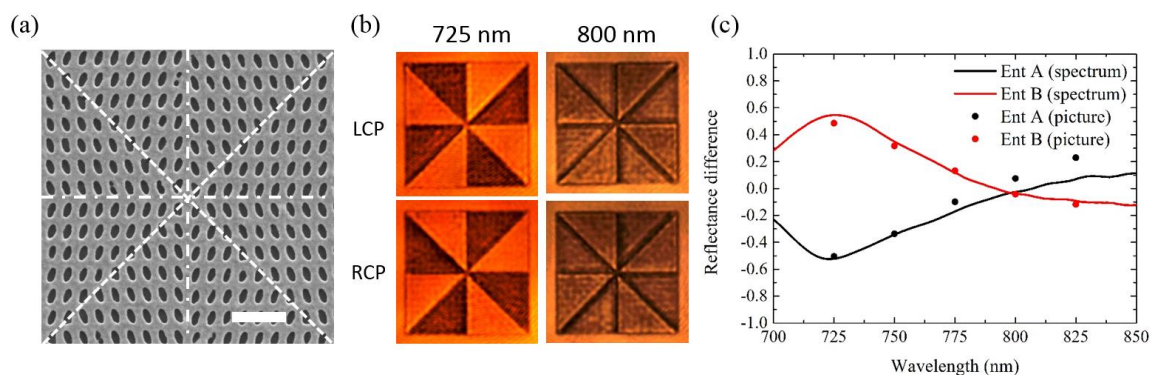


Figure 3. (a) Top view of fabricated windmill pattern. (Scale bar: 10um (a)) (b) Windmill pictures with incidence LCP and RCP light of difference wavelength. (c) Reflectance difference spectrum with incidence of LCP and RCP light. Black and red dots represent normalized intensity difference calculated from windmill picture.

3. SELECTIVE QUANTUM DOTS RCP AND LCP SPONTANEOUS EMISSION CONTROL

As we stressed earlier, to control spontaneous emission polarization the chiral selective electric field enhancement could be used, so we moved further to control dipole emitter emission property by coating quantum dot on top of chiral metasurface. The unique

chiral dichroism design ensure that the density of states for one spin state of photon significant larger than that of the other spin state, so that the QD emit more photon with one spin state than the other. Because the thin polymer layer was coated above the metasurface, resonant wavelength was red shift of to 750nm as shown in Fig. 4 (a, b). CdSe/ZnS QD (Qdot 800ITK Organic) with central emission wavelength around 775nm which slighted larger than 750nm was deliberated selected in experiment. The spectral overlap of the QD luminescence (gray area) with metasurface reflectance can results in the strong coupling efficiency between dipole emitter and plasmonic resonance mode.

To exclude the influence of pump light (402 nm) polarization on QD emission, QD was coated on control multilayer without pattern and illuminated by light with different polarization and one set of linear polarizer and quarter wave plate was placed in the collection optical path to separate LCP/ RCP component of emission light. As expected, the pump light polarization has no influence on the QD emission light polarization. When QD was excited either linear or circular polarized light, the emission intensity of LCP and RCP light were identical.

In the experiment, laser light without polarization was used to excite the QD above the chiral metasurface and spectral resolved photoluminescence intensity and time resolved spontaneous emission lifetime were measured for emission LCP and RCP component respectively. As expected, QD placed on top of metasurface which absorb more LCP/RCP light will emit more photons with that polarization. As indicated in Fig. 4 (c) LCP luminescence intensity of enantiomer A is larger than RCP luminescence intensity. It is worth noting that LCP luminescence peak is shifted to plasmonic resonance wavelength instead of QD Luminescence peak wavelength which unambiguously demonstrated that it

is dipole and chiral plasmonic coupling process that enhance LCP luminescence intensity. If the PL difference is due to selective chiral absorption, LCP luminescence intensity will be decreased and LCP peak wavelength should be red shifted which is not shown in experiment. Accordingly, average spontaneous lifetime extracted from stretched exponential relaxation model (94.1 ns) for LCP component is shorter than that (110.4 ns) of RCP component of enantiomer A as indicated in Fig. 4 (c). As of enantiomer B, RCP luminescence intensity is larger than that of LCP (Fig. 4 (d)) and RCP average spontaneous lifetime (94.8 ns) is shorter than LCP average spontaneous lifetime (101.8 ns) shown in Fig. 4 (f). These experiment results match our expectations very well that the chiral metasurface can control the dipole emitter spontaneous emission circular polarization.

In Fig. 4 (g), the chiral dichroism of photoluminescence (CDPL) was calculated using similar equation as CDR, $CDPL = (PL_{LCP} - PL_{RCP}) / (PL_{LCP} + PL_{RCP})$. Even though the peak emission wavelengths for LCP and RCP component are a little bit different, calculated CDPL peak wavelength (750nm) coincident with that of CDR (750nm) very well. This phenomenon further strengthen the dipole and plasmonic mode coupling mechanism. There is no doubt that CDPL is smaller than CDR because just coating QD on top of metasurface cannot exploit the full potential of chiral dichroism property of metasurface. Place the QD in the dielectric spacer layer in the fabrication process could have better control of spontaneous emission of dipole emitters.

The coupled QD-metasurface system was also investigated through 3D FDTD simulation with respect to photoluminescence properties for LCP and RCP emission light. The dashed line in Fig. 4 (h) indicates the simulated photoluminescence intensity for the

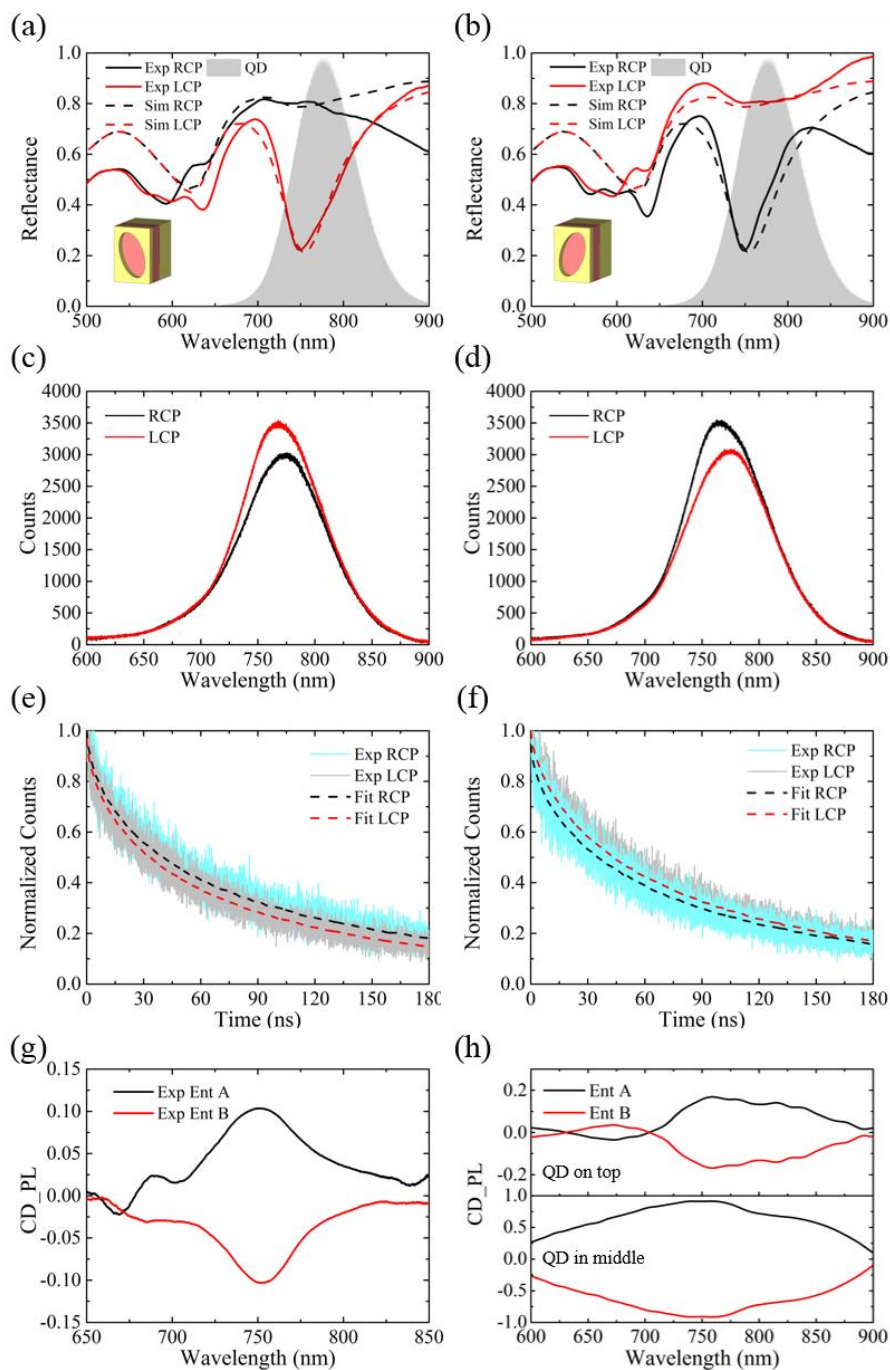


Figure 4. (a, b) Reflectance spectrum with LCP and RCP incidence after coating polymer. (c, d) LCP and RCP component of photo luminescent emitted from quantum dot placed in two enantiomers. (e, f) Fluorescence lifetime decays of LCP and RCP emission light from two enantiomers. (f) LCP and RCP intensity difference of two enantiomers. (g) Experimental CD_PL of two enantiomers. (h) Simulated CD_PL of two enantiomers when QDs placed above Au top surface and in the middle SiO₂ layer.

two circular polarized component averaged from electrical dipole emitters with three orthogonal polarizations and at 35 different positions located 30 nm above the top Au surface. The simulation results in Fig. 4(h) show excellent agreement with the experiment results for the CDPL. Furthermore, simulations also verify that placing QDs in the middle of SiO₂ spacing layer at the locations of the electromagnetic fields maxima will result in stronger exciton-plasmon coupling and larger CDPL as large as 0.91 (Fig. 4 (h)).

4. CONCLUSIONS

In the present work, we have proposed and experimentally demonstrated chiral selective reflection metasurface with chiral-selective absorption band that strongly absorb one-handed circular polarized light and reflect the other results in significant circular dichroism. By deliberately designing the metasurface chiral absorption band on-resonance with QD emission, we are able to enhance the chiral spontaneous emission of QD and investigate the coupling of QDs to chiral plasmonic mode. Via circular polarization dependent spectrally and time-resolved PL measurement, we have demonstrated that the chiral metasurface can selectively enhance dipole emitter corresponding circular polarization photon emission. We observe PL of LCP/RCP emission is 10% larger than that of LCP/RCP emission on top of corresponding chiral metasurface at the plasmonic resonance wavelength. At the same time, the QD lifetime measurement results respect to different circular polarization in the coupling system further validate the PL spectrum modification. The experiment results are supported by finite element analysis calculation of reflectance and PL spectrum. This finding has important implications for the chiral optoelectronic devices, optical information processing, and chiral sensing.

5. METHOD

The tilted elliptical arrays are fabricated on the top Au layer via focused ion beam milling (FEI Helios Nanolab 600 Dual Beam) with a gallium ion current of 9.7 pA and an accelerating voltage of 30 KeV. Then a thin polymer layer loaded with CdSe/ZnS QD (Qdot 800ITK Organic) was spin-coated on top of nanostructure (3000 rpm for 15min at room temperature). The original QD solution (QD weight ratio 0.15%, solvent: water) is diluted with a mixed solution of polyethylene glycol (PEG), buffer and water, resulting in final weight ratios for QDs and PEG of 0.013% and 1.7%, respectively.

When measure reflectance spectrum, all experimental spectra were normalized to that of a silver coated mirror (THORLABS) which has optical reflection larger than 97.5% in the visible range. Fluorescence lifetime and luminescent intensity were carried out using a homemade spectral-resolved and time-resolved fluorescence microscopy. The samples were excited by a picosecond pulsed laser emitting at 402nm (52 ps pulse width, 40 MHz repetition rate, 20 μ W excitation power, PicoQuant). Excitation light was focus on the sample using long focal objective lens (Olympus, NA = 0.8, 80X). Emission was collected by the same objective lens and directed to spectrometer (Horiba IHR550) where luminescence intensity was measured from a liquid N₂ cooled CCD detector and desired wavelength emission light was selected to the side exit split and coupled to a fiber coupled single photon detector (SPAD, MICRO PHOTON DEVICES). 650nm long pass filter was used to separate the fluorescence emission from the excitation. Time-correlated single photon counting system (PicoHarp 300, PicoQuant Photonics) in Time-Tagged Time-Resolved mode (TTTR mode) was used to measure fluorescence lifetime.

The spontaneous emission lifetime of QDs was extracted by fitting the experimental photoluminescence decay data using stretched exponential relaxation model: $I(t) = I_0 e^{-(t/\tau)^\beta} + I_b$ [4, 19], where τ is the lifetime after which the fluorescence intensity I decay to $1/e$ of initial value I_0 . β is modification parameter that describe the deviation of experimental multi-exponential decay curve from ideal single-exponential decay model (when $\beta = 1$). Final average lifetime can be calculated from $\langle\tau\rangle = (\tau/\beta)\Gamma(1/\beta)$ [20], where Γ represents the gamma function. The fitted average lifetime for Ent A is 94.1 (LCP) and 110.4 (RCP), whereas for Ent B is 101.8 (LCP) and 94.8 (RCP) respectively. The fitted lifetime τ value for Ent A is 66.9 (LCP) and 74.0 (RCP), whereas for Ent B is 76.8 (LCP) and 70.1 (RCP) respectively. The fitted β value for Ent A is 0.63 (LCP) and 0.60 (RCP), whereas for Ent B is 0.67 (LCP) and 0.66 (RCP) respectively.

Finite element method and Finite-difference time-domain method are used to calculate the metasurface reflectance spectrum and QD PL intensity. The permittivity of gold is taken from Johnson and Christy and damping constant was set as 2 times to compensate surface scattering and grain boundary effects in fabricated thin film. Electric dipole was used to represent QD to investigate the emission process in the coupled system around resonant wavelength. The electric dipole with three dipole moment directions along x, y and z axis was placed at 35 different positions located 30 nm above the top Au surface. The final PL results are averaged from PL from dipole with three directions maxima (Fig. 4 (g), dashed line). To find best CDPL, electric dipole was placed in the middle of SiO₂ spacing layer -110nm below top Au layer at the locations of the electromagnetic fields maxima (Fig. 4 (h), solid line).

ACKNOWLEDGMENTS

The authors thank Yichen Liang for the useful discussion and acknowledge the facility support from the Materials Research Center at Missouri S&T. This work was performed, in part, at the Center for Nanoscale Materials, a U.S. Department of Energy, Office of Science, and Office of Basic Energy Sciences User Facility under Contract No. DE-AC02-06CH11357.

REFERENCES

- [1] Schäferling, M., *Chiral Nanophotonics: Chiral Optical Properties of Plasmonic Systems*. Vol. 205. 2016: Springer.
- [2] Kelvin, W.T.B., *Baltimore lectures on molecular dynamics and the wave theory of light*. 1904: CJ Clay and Sons.
- [3] Purcell, E.M., H.C. Torrey, and R.V. Pound, Resonance absorption by nuclear magnetic moments in a solid. *Physical review*, 1946. 69(1-2): p. 37.
- [4] Li, L., et al., Enhanced quantum dot spontaneous emission with multilayer metamaterial nanostructures. *ACS Photonics*, 2017. 4(3): p. 501-508.
- [5] Sun, L., et al., Diffraction-free optical beam propagation with near-zero phase variation in extremely anisotropic metamaterials. *Journal of Optics*, 2015. 17(3): p. 035101.
- [6] Krishnamoorthy, H.N., et al., Topological transitions in metamaterials. *Science*, 2012. 336(6078): p. 205-209.
- [7] Li, Z., et al., Wavelength-selective mid-infrared metamaterial absorbers with multiple tungsten cross resonators. *Optics express*, 2018. 26(5): p. 5616-5631.
- [8] Deng, H., et al., Broadband perfect absorber based on one ultrathin layer of refractory metal. *Optics letters*, 2015. 40(11): p. 2592-2595.
- [9] Wang, W., et al., Realizing structural color generation with aluminum plasmonic V-groove metasurfaces. *Optics express*, 2017. 25(17): p. 20454-20465.
- [10] Li, Z., et al., All-metal structural color printing based on aluminum plasmonic metasurfaces. *Optics express*, 2016. 24(18): p. 20472-20480.

- [11] Frank, B., et al., Large-area 3D chiral plasmonic structures. *ACS nano*, 2013. 7(7): p. 6321-6329.
- [12] Li, W., et al., Circularly polarized light detection with hot electrons in chiral plasmonic metamaterials. *Nature communications*, 2015. 6: p. 8379.
- [13] Kang, L., et al., An active metamaterial platform for chiral responsive optoelectronics. *Advanced Materials*, 2015. 27(29): p. 4377-4383.
- [14] Ye, W., et al., Large Chiroptical Effects in Planar Chiral Metamaterials. *Physical Review Applied*, 2017. 7(5): p. 054003.
- [15] Tang, B., et al., Chiral-selective plasmonic metasurface absorbers operating at visible frequencies. *IEEE Photonics Technology Letters*, 2017. 29(3): p. 295-298.
- [16] Ouyang, L., et al., Near-infrared chiral plasmonic metasurface absorbers. *Optics Express*, 2018. 26(24): p. 31484-31489.
- [17] Liang, Y., et al., Functionalization of CdSe semiconductor nanocrystals with organic charge-transporting ligands. *Journal of Materials Chemistry C*, 2015. 3(16): p. 4134-4140.
- [18] Liang, Y., et al., Enhancement in the photorefractive performance of organic composites photosensitized with functionalized CdSe quantum dots. *Optical Materials*, 2016. 58: p. 203-209.
- [19] Berberan-Santos, M., E. Bodunov, and B. Valeur, Mathematical functions for the analysis of luminescence decays with underlying distributions 1. Kohlrausch decay function (stretched exponential). *Chemical Physics*, 2005. 315(1-2): p. 171-182.
- [20] Schlegel, G., et al., Fluorescence decay time of single semiconductor nanocrystals. *Physical Review Letters*, 2002. 88(13): p. 137401.

SECTION

2. CONCLUSION

In conclusion, various plasmonic metamaterial structures for structural color printing and quantum emitter spontaneous emission enhancement are explored and discussed in this project.

For plasmonic structural color printing, an all-aluminum structural color printing platform based on plasmonic V-groove metasurfaces and square-shaped disk arrays with high resolution and high color performance have been introduced and demonstrated by using a one-step focused ion beam milling process. By only adjusting the groove depth, the plasmonic resonances of the V-groove arrays can be tuned across the whole visible spectrum, resulting in either the subtractive colors obtained from the reflection spectra under the bright field illumination, or the complimentary additive colors resulting from the scattering spectra under the dark field illumination. The reproduced polarization dependent plasmonic paintings of color images under both the bright field and dark field illumination conditions manifest the feasibility and flexibility of all-aluminum plasmonic V-groove metasurfaces for structural color printing applications. By varying the geometrical parameters of square-shaped disk arrays including the disk etching depth, disk width and unit cell period, a wide range of visible colors has been achieved with the plasmonic metasurfaces. The subtractive colors are obtained from the reflection spectra due to the excitation of plasmonic electric and magnetic dipole resonances. The reproduced

microscale landscape patterning shows the feasibility and flexibility of all-metal plasmonic metasurfaces used for color printing applications.

For quantum emitter spontaneous emission enhancement, multilayer metamaterials, plasmonic perfect absorber and chiral metasurfaces were used to control dipole emitter spontaneous emission.

First, we have demonstrated multilayer metamaterial and multilayer grating nanostructures with broadband Purcell effects for CdSe/ZnS QD emission. Several-fold emission rate enhancement is achieved with a large LDOS as the emission wavelength goes from the elliptical to the hyperbolic dispersion regime across the ENZ region of a multilayer metamaterial. Multilayer gratings further enhance the QDs' spontaneous emission as the QDs located inside the grating grooves strongly interact with high-k coupled SPP modes. Position and polarization effects on QD emission rate enhancement are studied to reveal the coupling mechanisms and further engineer the LDOS in metamaterial nanostructures.

Second, anomalous power law for the Purcell factors has been demonstrated for hyperbolic metamaterial cavities with dipole excitation. Contrary to conventional optical cavities, identical fundamental resonance mode is supported in a series of hyperbolic multilayer nano-cavities with different resonating wavevectors. A fifth power law $PF \sim (k/k_0)^5$ for small wavevectors and a square law $PF \sim (k/k_0)^2$ for large wavevectors have been shown for 2D hyperbolic cavities. The Purcell factors calculated from emission power ratio can be understood well from the scaling laws for quality factor and mode area of the cavity mode.

Third, we have experimentally demonstrated the enhancement of CdSe/ZnS QDs spontaneous emission rates and photoluminescence intensity with metamaterial perfect

absorbers, which consist of hexagonal array of holes on a Ag-SiO₂-Ag thin films through rational design, and possess near-unity absorption at the QDs emission wavelength. Numerical simulations of the emission rate and intensity enhancement on the four studied QD-PA devices, as well as the electromagnetic fields distribution under dipole emitter excitation, have been conducted to assist the comprehensive understanding of the experimental observations.

Finally, we have proposed and experimentally demonstrated chiral selective reflection metasurface with chiral-selective absorption band that strongly absorb one-handed circular polarized light and reflect the other results in significant circular dichroism. By deliberately designing the metasurface chiral absorption band on-resonance with QD emission, we are able to enhance the chiral spontaneous emission of QD and investigate the coupling of QDs to chiral plasmonic mode. Via circular polarization dependent spectrally and time-resolved PL measurement, we have demonstrated that the chiral metasurface can selectively enhance dipole emitter corresponding circular polarization photon emission. We observe PL of LCP/RCP emission is 10% larger than that of LCP/RCP emission on top of corresponding chiral metasurface at the plasmonic resonance wavelength. At the same time, the QD lifetime measurement results respect to different circular polarization in the coupling system further validate the PL spectrum modification. The experiment results are supported by finite element analysis calculation of reflectance and PL spectrum.

The overall outcomes of this dissertation addressed several key applications of the plasmonic metamaterials. The demonstrated aluminum plasmonic metasurfaces for structural color printing will be well suited for applications such as microscale imaging,

information storage, anti-counterfeit tag and security marking. The dissertation also provides a systematic approach understanding of QD-metamaterial interactions. This finding has important implications in light-matter interactions such as light-emitting devices, nanoscale lasers, quantum electrodynamics, and quantum information processing.

BIBLIOGRAPHY

- [1] Novotny, L. and B. Hecht, Principles of nano-optics. 2012: Cambridge university press.
- [2] Saleh, B.E., M.C. Teich, and B.E. Saleh, Fundamentals of photonics. Vol. 22. 1991: Wiley New York.
- [3] Sarid, D. and W. Challener, Modern introduction to surface plasmons: theory, Mathematica modeling, and applications. 2010: Cambridge University Press.
- [4] Eisaman, M., et al., Invited review article: Single-photon sources and detectors. Review of scientific instruments, 2011. 82(7): p. 071101.
- [5] Cai, W. and V. Shalaev, Optical metamaterials: fundamentals and applications. 2009: Springer Science & Business Media.
- [6] Purcell, E.M., Spontaneous emission probabilities at radio frequencies. Physical Review, 1946. 69: p. 681.

VITA

Wei Wang was born in Fuzhen, Botou City, Hebei province, China. He received his Bachelor of Science degree in Optical Information Science and Technology from Department of Applied Physics, School of Science, Northwestern Polytechnical University (NPU), Xi'an, P. R. China. in June 2009. In June 2012, he received his Master of Science degree in Optical Engineering from National Laboratory of High Power Laser and Physics, Shanghai Institute of Optics and Fine Mechanics, Chinese Academy of Sciences (SIOM, CAS), Shanghai, P. R. China. From July 2012 to July 2013, he worked as a System Engineer in Shanghai Micro Electronics Equipment Co. Shanghai, P. R. China. In May 2019, he received his Doctor of Philosophy in Mechanical Engineering from Missouri University of Science and Technology, Rolla, Missouri, USA. His research in nanophotonics was a multidisciplinary research area that bridges the researchers across the fields of engineering, applied physics, optics, and material science. He was dedicated to design, fabrication and characterization of nanophotonic, plasmonic and optical metamaterial devices for understanding light-matter interactions at the nanoscale, which will advance many exciting applications in optical energy harvesting, optical sensing, chip-scale light sources and optical information processing. He authored and co-authored ten journal papers and two conference papers in the optics areas.